Grant Agreement No.: 226479

SafeLand

Living with landslide risk in Europe: Assessment, effects of global change, and risk management strategies

7th Framework Programme
Cooperation Theme 6 Environment (including climate change)
Sub-Activity 6.1.3 Natural Hazards

Deliverable 3.8

Changing pattern in climate-driven landslide hazard at selected sites in Europe (focus on Southern Italy, the Alps and Southern Norway) in the next 50 years

Work Package 3.3 - Landslide hazard evolution in Europe and risk evolution in selected "hotspot" areas

Deliverable/Work Package Leader: BRGM Revision: [No.] – ~~Draft~~/Final

April, 2012

Rev.	Deliverable Responsible	Controlled by	Date
0	BRGM	JRC	27 April 2012
1			
2			

SUMMARY

Previous study within the Safeland project (D3.7) has developed and applied a method to estimate impacts of climate change on the landslide hazard in Europe. The results, based on the A1B IPCC scenario, show a limited increase in the total amount of area exposed to landslide (+1.5%).
However, more detailed methods and finer data are required to assess the evolution of landslides hazard at local scale. Several methods have been proposed, one empirical, one semi-quantitative and two based on physics of phenomena, in order to transpose the scenario of climate change at low resolution, computed in other tasks within the Safeland Project (D3.3), into evolution of landslide activities at local site.
These methods have then been applied to different climatological context (Norway, Alps, Southern Italy and Spain) to evaluate these changes.

Note about contributors

The following organisations contributed to the work described in this deliverable:

Lead partner responsible for the deliverable:
BRGM: Vandromme Rosalie, Hohmann Audrey, Desramaut Nicolas, Baills Audrey

Partner responsible for quality control:
JRC : Van Den Eeckhaut Miet, Hervás Javier,

Other contributors:
ICG/NGI: Cepeda José, Syre Egil
UNISA: Sorbino Giuseppe, Cuomo Sabatino, Peduto Dario, Cascini Leonardo
ETHZ: Narasimhan Harikrishna
UPC: Hürlimann Marcel, Corominas Jordi

Aknowledgement to Malet Jean-Philippe (CNRS) for providing the data on Barcelonnette site.

CONTENTS

Figures

Tables

INTRODUCTION

Climate change in the next century is expected to lead to a modification of various meteorological parameters such as the spatial and temporal distribution of precipitation and extreme events. For rainfall induced landslides, the hazard maps are mainly influenced by the evolution of precipitation but other types of landslide may be impacted differently by climate change. For instance rock falls main triggering parameters are frost-defrost cycles. Other thresholds related to phenomena such as glacier or pergelic soil melting, sea level rising or change in land cover should be considered from the perspective of an exhaustive review of climate change impacts on landslide hazards. The aim of this work was to develop a methodology for integrating climate change scenarios and, as far as possible, other global-change scenarios into risk assessment. The influence of climate change depends on both the location of the test sites and the type of landslide considered, as they are not necessarily triggered by the same factors. Thus, three main areas have been selected to apply the methodology (the Alps, southern Italy and southern Norway) in order to cover different potential configurations.

FIRST PART - Methodology development

1. METHODS

a. ALICE and GARDENIA

The proposed approach is based on the coupling of a hydrological model (GARDENIA®) with a slope stability model (ALICE®), in order to spatially estimate safety factors. From a Digital Elevation Model (DEM) and land-cover, geological and geotechnical data, the ALICE® classifies hazard zones depending on geotechnical and different hydrological contexts varying in time. The methodology is applied to the Norwegian site for demonstration purpose on current climatic condition data (see SECOND PART 1.b) and to the Ubaye valley (France) using present and past climate conditions (See SECOND PART 2.b).

i. ALICE

ALICE®, which stands for Assessment of Landslides Induced by Climatic Events, is a programme designed to support landslide hazard mapping (Sedan, 2011 and Olivier et al., 2011). The model is based on a mechanical and geotechnical approach for which the main physical characteristics of the medium are quantified and used by a mathematical model calculating the safety factor (Aleotti & Chowdhury, 1999). In these models, the spatial variability of the parameters (e.g. mechanical characteristics) has to be known and is handled through GIS software. The probabilistic approach used in the software allows taking into account uncertainties by giving probabilistic distributions to some of the model parameters (Stillwater, 2007).

The software uses the Morgenstern and Price method (1967), which is a finite slope stability model based on the equilibrium calculation between slices subdividing the landslide volume. This method is used on regularly spaced topographic 2D profiles which cover the whole studied area. These profiles are automatically generated by the software using four input raster maps: a DEM, a slope map, a flow direction map and a flow accumulation map. Pedological and geological characteristics are taken into account thanks to the depth maps of the interfaces between each soil layer, the highest limit corresponding to the topographic surface (DEM). Variability and uncertainty of the geotechnical parameters are introduced in the software by means of probabilistic distributions (normal, uniform, triangular or trapezoid). A distribution is attributed to each soil characteristic i.e. cohesion (c), friction angle (ϕ) and unit weight (γ), and for each soil layer, and handled by the Monte Carlo method. The safety factor calculation also needs the assumption of the type of the landslide (rotational or translational) and its length. These parameters are defined for the whole studied area.

Another important factor of slope stability considered in ALICE is the pore pressure (and its variation) inside the slope. The hydrological condition in the different slopes is, thus, introduced thanks to the levels of the water table along the profile, which are then used to estimate pore pressures. This parameter is the only characteristic varying in time (due to the meteorological conditions) in the estimation of slope stability, and, hence, is the one which will vary over time.

In ALICE, the spatialization of the water table is performed using a global indicator, so-called filling ratio, FR, (in this study, provided by GARDENIA) and two piezometric maps: the lowest and highest water level maps. The resulting water level at any point is therefore computed according to this formula:

$$\boldsymbol{WL(i,j) = WL_{min}(i,j) + \left(WL_{max}(i,j) - WL_{min}(i,j)\right) * FR} \qquad \textbf{(1)}$$

With *WL(i,j)* *Water level at point (i,j)*

$WL_{min}(i,j)$ *Lowest water level at point (i,j)*
$WL_{max}(i,j)$ *Highest water level at point (i,j)*
FR *Filling Ratio*

ii. GARDENIA

In order to transform climatic data (either past records or future climatic scenarios) into filling ratio, the required hydrological input in ALICE, a global hydrological model is used.

This model is part of the GARDÉNIA® v.7.0 software package, developed by BRGM for lumped hydrological modelling of rainfall–runoff and aquifer level (Thiéry 2003). The GARDÉNIA® model simulates the water cycle from rainfall received by the soil surface until the outlet, either as the discharge rate or as the aquifer level at a given point. The hydrological system is modelled by a system of 3 or 4 tanks (top tens of centimetres of soil, where evapotranspiration occurs; an intermediate (unsaturated) level, where runoff occurs; and one or two aquifer zones, with delayed flows).

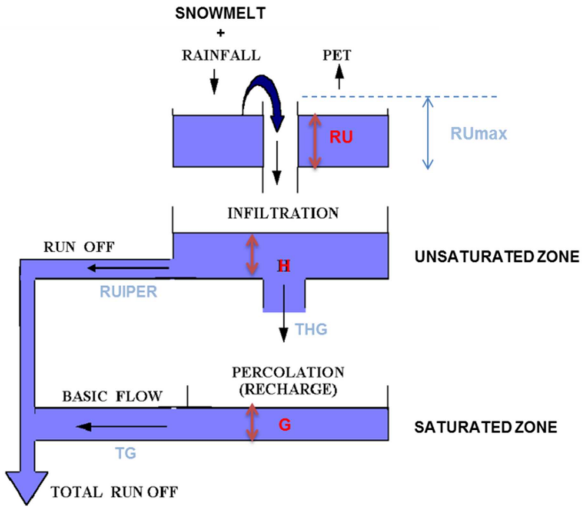

	Descriptions	Unit
RUmax	Maximal deficit of soil, i.e. maximal water level of the soil zone	mm
RU	Water level in the soil zone	mm
H	Water level in the unsaturated zone	mm
RUIPER	Water level for which run-off and percolation are equal	mm
THG	Half-time of percolation	day
G	Water level in the saturated zone	mm
TG	Half time of depletion	day

Figure 1: Description of the hydrological model (adapted from Thiéry 2003)

Hence, it allows the simulation of the relationships between series of:

- discharge data of a spring or stream and rainfall amounts received by the corresponding basin
- piezometric levels in an aquifer and amounts of rainfall received by the corresponding basin.

This model involves 4 to 6 lump parameters (soil and atmospheric characteristics). These parameters are calibrated using rainfall, discharge data and water level data from past records.

Filling ratios (FR) are deduced from the computed level of the saturated zone (G), according to the following equation:

$$\boldsymbol{FR = \frac{G - min(G)}{max(G) - min(G)}} \qquad (2)$$

It should be noticed that this filling ratio is thus related to the saturated zone and does not take directly into account the water content of the unsaturated zone.

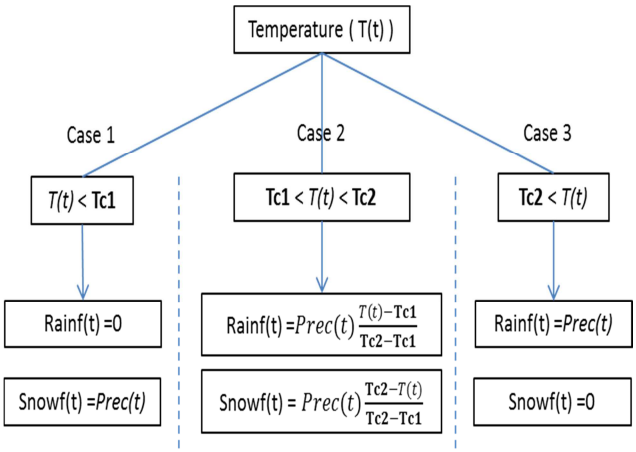

	Descriptions	Unit
Prec (t)	Total precipitation falling during day t	mm/day
Rainf(t)	Liquid precipitation falling during day t	mm/day
Snow(t)	Solid precipitation falling during day t	mm/day
Tc1	Temperature threshold below which precipitations fall as snow	°C
Tc2	Temperature threshold above which precipitation fall as rain	°C

Figure 2: Differentiation between snowfall and rainfall based on temperature

Another module has been developed to take into account snowfalls, their accumulation as snowpack and the process of melting, which adds further to rainfall. Based on the air temperature T, precipitation falls either as snow, rain or a mix of both (Figure 2). Then, if the temperature is higher than a threshold (*Tc*), the accumulated snowpack would melt following a degree-day approach (parameter *a*, in $mm.day^{-1}.K^{-1}$), as described in Equation (3). This extra water is added to the daily rainfall and goes into the upper tank (Figure 1).

$$\boldsymbol{Potential\ for\ snowmelt} = \begin{cases} \boldsymbol{a(T(t) - Tc)\ if\ T(t) > Tc} \\ \boldsymbol{0 \qquad\qquad if\ T(t) < Tc} \end{cases} \qquad (3)$$

iii. Workflow with GARDENIA and ALICE

The complete model implemented in this study links the global hydrological model Gardenia® to the slope stability model, ALICE® (Figure 3). After a calibration phase for both tools, based on available observations of rainfall events, water table levels and historical landslides, this methodology computes an estimate of the susceptibility for rainfall-induced landslides that could occur at the regional scale. Meteorological events gather all information from forecasts for near-future events to scenarios from climate change models for further periods. This is particularly useful in evaluating changing patterns of landslide activities due to climate change.

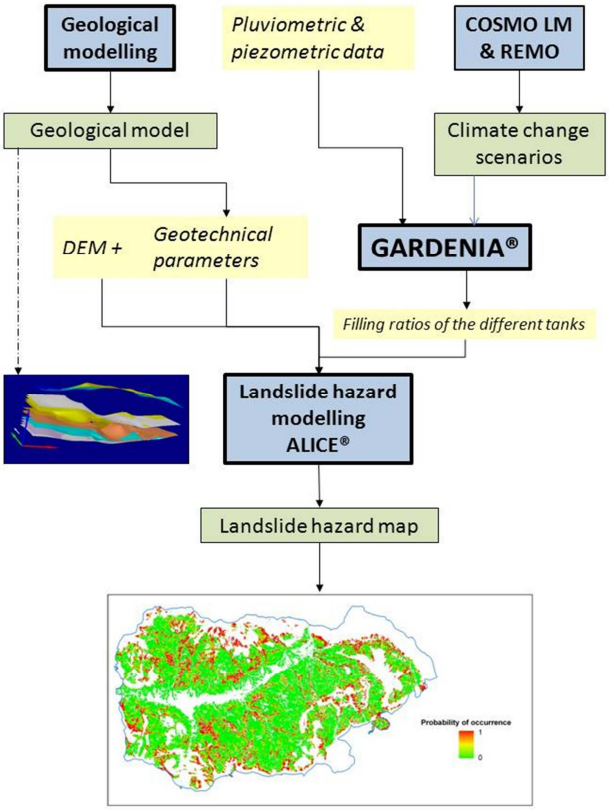

Figure 3: Chain of the methodology for coupling the hazard assessment tool with the hydrological model

b. UNISA's methodology

The proposed methodology is based on hydrology, geology and geotechnics and it consists in five steps.

The Step I is the construction of the rainfall Intensity-duration (I-D) curves for the selected area; to this aim hydrological analyses of historical rainfall data are performed to evaluate the I-d curves without considering any climate change.

Step II consists in the selection of the rainfall Intensity-duration (I-D) values to be considered in the analysis; particularly, for a given return period (T), rainfall intensity is chosen based on saturated hydraulic conductivity while rainfall duration is selected based on: i) the return period (T) and ii) the capability of rainfall to increase the pore water pressures inside the soil deposit which can be estimated through different analytical formulations (e.g., Pradel & Raad, 1993).

Step III consists in the application of geotechnical physically-based models to evaluate the hazard scenarios for the landslide source areas. The used models will be either SHALSTAB (Montgomery & Dietrich, 1994) or TRIGRS (Savage et al., 2004; Godt et al., 2008) both extensively described in Safeland Deliverable D1.2 (par.4.1.2.2). To this aim, high quality data are used: i) DEM (5 x 5 m, at least), ii) soil cover thickness map, iii) geomorphological map, iv) soil mechanical properties map. Previous applications of these models can be found in Sorbino et al. (2010).

Step IV is the application of mathematical models for the analysis of landslide propagation stage. Particularly, the commercial Flo-2D code (O'Brien et al., 1993) will be used which has been

successfully applied to previous case studies of flowslides and debris flows (Pirulli & Sorbino, 2008; Cascini et al., 2011).

Step V consists in the analysis of the results and includes the assessment of the effects of climate change on both the landslide source and propagation areas, integrating I-D curves from climate change

c. ICG's model

The ICG model is based on the experience gained in the HOTSPOT study from 2006 (Nadim et al., 2006). This type of analysis is based on expert judged reclassification and weighting of different factors that are assumed to be important for landslide susceptibility and hazard. Once the hazard is established, risk is estimated by considering exposure and vulnerability.

The analysis is a pixel based multiplication of the important factors to achieve a hazard index. This is done independently for two triggers, rainfall and seismicity. In the present evaluation, only the rainfall triggering factor is accounted for.

The term "landslide" in this study focuses on events involving gravity-driven rapid mass movement down-slope, like soil slides and flows, induced by rainfall; which pose a threat to human life. Slow moving slides have significant economic consequences for constructions and infrastructure, but rarely cause any fatalities.

To identify the global landslide hazard and risk "hotspots", Nadim et al. (2006) adopted a simplified first-pass analysis method. The scale of their analysis was a grid of roughly 1km x 1km pixels where landslide hazard, defined as the annual probability of occurrence of a potentially destructive landslide event, was estimated by an appropriate combination of the triggering factors (mainly extreme precipitation and seismicity) and susceptibility factors (slope, lithology, vegetation and land cover). The principles of the method are depicted in Figure 4.

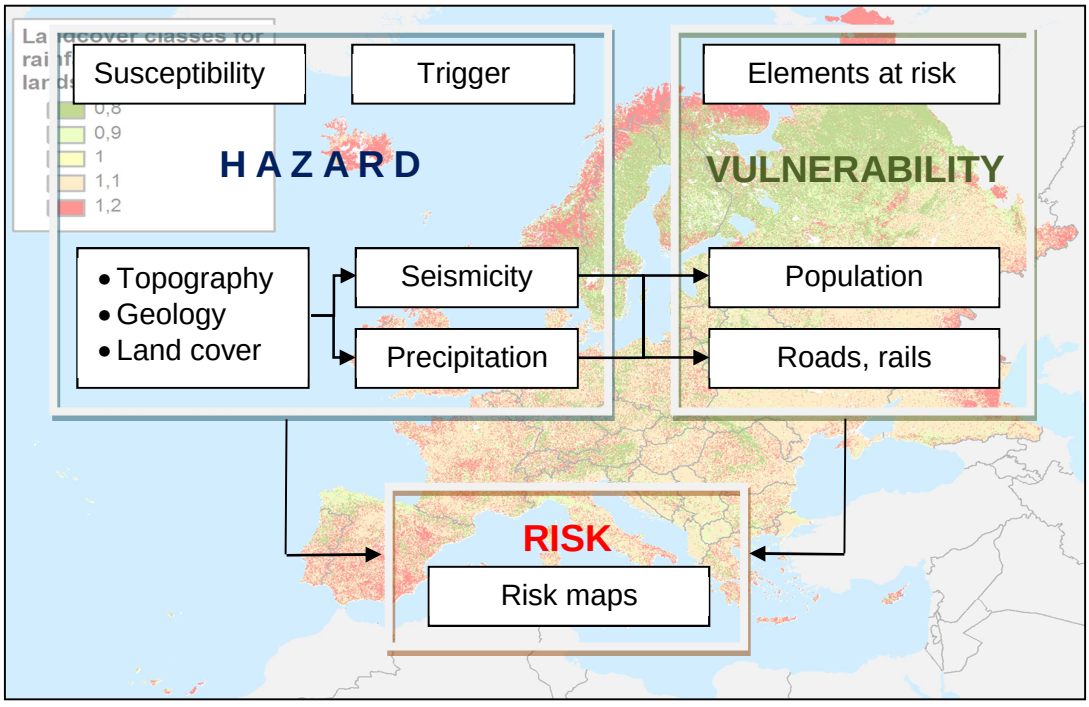

Figure 4: Schematic approach for landslide hazard and risk evaluation.

The weights of different triggering and susceptibility factors were calibrated to the information available in landslide inventories and physical processes. The general approach used in the present study is an adapted version of the approach used by Nadim et al. (2006).

The key adaptations in the present model are:

- The increased resolution on the DEM and consequently the slope data. In SafeLand D2.10 and D3.7, a 30 arc seconds resolution was used (from a SRTM dataset), whereas the present study uses a 5m DEM based on a 1m contour map (1:5000).
- Increased resolution of the lithology and land use maps (1:5000) compared to the European scale data used in SafeLand D2.10 and D3.7.
- Calibration of the model based on a bivariate regression of the susceptibility factors and a landslide inventory.
- Estimation of the precipitation triggering factor based on a probabilistic assessment of threshold criteria developed in SafeLand D1.5.

The general model for landslide hazard assessment uses the following equation:

$$H = \left(\prod_{i=1}^{p} S_i \right) \times T \qquad (4)$$

where H is a landslide hazard index, S_i is the i-th susceptibility factor, p is the total number of susceptibility factors and T is a triggering factor.

The indices for precipitation-induced landslide hazard were estimated using the following equation:

$$H_r = (S_r \times S_l \times S_v) \times T_p \qquad (5)$$

where H_r is the landslide hazard index for rainfall-induced landslides, S_r is the slope factor within a selected grid cell, S_l is lithological (or geological) conditions factor, S_v is the vegetation cover or land use factor, and T_p is the precipitation factor.

In SafeLand D2.10 and D3.7, the susceptibility factors were calibrated based on expert judgment and experience. In the present adaptation, the following three criteria were used:

- Maximum and minimum values are the same as in SafeLand D2.10 and D3.7.
- A spatial bivariate statistical analysis was performed between each susceptibility factor and the landslide inventory in order to obtain weights for every class in each susceptibility factor (van Westen, 1997). The calibration was performed using data from all Norway, not only from the study area.
- The susceptibility factors were obtained by standardizing the weights of the classes to the maximum and minimum values in the corresponding factor. The factors were rounded to the same number of significant digits (0 digit for slope factor and precipitation factor, 1 digit for lithological and land-cover factor) as in SafeLand D2.10 and D3.7 (except for the lithology factor, where one more significant digit was used).

The weights for every class were obtained using the following equation (van Westen, 1997):

$$\ln W_i = \ln\left(\frac{DC}{DM}\right) = \ln\left(\frac{NS_i/NN_i}{\sum NS_i/\sum NN_i}\right) \quad (6)$$

where,

W_i = weight for the i-th class within a susceptibility factor.
DC = density of landslides within the i-th class.
DM = density of landslides within the entire map.
NS_i = number of pixels with landslides within the i-th class.
NN_i = number of pixels within the i-th class.

2. UNCERTAINTIES

i. SOURCES AND CATEGORISATION OF UNCERTAINTIES

A large number of propositions exist for the characterization of uncertainties. A common practice is to differentiate between uncertainties due to inherent natural variability, model uncertainties and statistical uncertainties. Whereas the first mentioned type of uncertainty is often called aleatory (or Type 1) uncertainty, the latter two are referred to as epistemic (or Type 2) uncertainties. This distinction has been considered in literature for the risk assessment of technical systems (e.g., Apostolakis, 1990; Helton and Burmaster, 1996) and increasingly for the risk assessment and management of natural hazards (e.g., Hall, 2003; Apel et al. 2004; Straub and Der Kiureghian, 2008), and has been discussed also for general geological applications by Mann (1993). Aleatory uncertainties are interpreted as random uncertainties, which, for a given model, are naturally inherent to the considered process; epistemic uncertainties are related to our incomplete knowledge of the process, often because of limited data and can be characterised in the form of model uncertainties and statistical uncertainties.

The absolute and relative magnitudes of aleatory and epistemic uncertainty are markedly case-specific. The differentiation into aleatory uncertainties and epistemic uncertainties is subject to a defined model of the considered system. The relative contribution of the two components of uncertainty depends on the spatial and temporal scale applied in the model. McGuire et al. (2005) argue that for those concerned with application of probability in a decision-theoretic perspective, the differentiation of uncertainty into aleatory and epistemic has no practical consequence. In this case, probabilities are deemed to reflect, in effect, the personal probability values that a decision maker is prepared to act upon. As a simple example, if one's decision about how to bet on a particular poker hand is the same before the cards are shuffled (pure aleatory variability) as they are after the five cards are dealt face down on the table (pure epistemic uncertainty), then our equality of preference between the two cases implies that we are assigning them the same probability and acting as if there is no difference between aleatory and epistemic uncertainties. In that case, the probability of an event (that has been defined in turn by probabilities and conditional probabilities of events segregated for whatever practical, operational reasons into epistemic and aleatory) is the average aleatory probability. The averaging, again, is over the epistemic probabilities. The formal basis for this interpretation lies in decision theory (e.g., Savage 1954, Raiffa 1968) which has the use of probability firmly in mind.

In practice, the differentiation in uncertainties is introduced for the purpose of setting focus on how uncertainty may be reduced, rather than calling for a differentiated treatment in the risk assessment and decision analysis process. The distinction is relevant because aleatory uncertainty cannot be

reduced for a given model. In contrast, epistemic uncertainty can be reduced, for instance, by collecting additional information. For this reason, a clear identification of the epistemic uncertainties in the analysis is crucial, as these may be reduced at a later time. Furthermore, neglecting epistemic uncertainty may lead to strong underestimation of the risk, see Coles et al. (2003) for an example.

There are various sources for epistemic uncertainties in large scale models; a brief description of some of these is provided below.

1. *Statistical uncertainty*

The parameters of the large scale models are derived empirically from data sets. Because of the limited size of these data sets, the estimated parameters are subject to statistical uncertainty.

Measurements and recordings of the geological properties are typically subject to uncertainty and observations of historical events are often incomplete and biased and must rely on local experts. As an example, rocks on a road will generally be reported and documented, but those that missed the road may often not be. Measurement uncertainty also results from drifts from equipment, operator/procedural and random measurement effects.

2. *Model uncertainty*

Extrapolation of the statistical models to areas other than those for which observations are available leads to additional uncertainty as the geological and topographical characteristics will be different for these areas. GIS-based models will take into account some of these parameters, but the omitted parameters will lead to an uncertainty in the model predictions. Uncertainty also occurs due to the approximations and simplifications inherent in empirical, semi-empirical, experimental or theoretical models used to relate measured quantities to non-measurable numerical parameters used in estimation.

3. *Spatial variability*

The frequency of hazard events varies in space. The observations represent an average over an area and the resulting parameter values, therefore, do not reflect the variations from the average.

4. *Temporal variability*

The frequency of hazard events varies in time. When working with annual frequencies, the seasonal changes do not affect the analysis, but the frequency may change over the years or may be dependent on extreme events (e.g., storms). However, in certain instances, e.g., when temporal closure of the road is considered as a risk reduction measure in rockfall risk management, seasonal variations must be explicitly addressed by the analysis.

How can these uncertainties be quantified? Statistical uncertainty can be quantified by using standard statistical methods such as Bayesian analysis, see, e.g., Coles (2001). Measurement uncertainty can generally be estimated when the data collection method is known. Unfortunately, no simple analytical method is available for estimating model uncertainties. A solution is to rely on expert opinion, i.e., to ask experts about their confidence in the models. It is also possible to compare the model with observations which have not been used in the calibration of the model (model validation) or to compare different models. Furthermore, it is possible to include additional parameters in the formulation of the model; the model uncertainties are then reduced while the statistical uncertainties increase which can then be estimated analytically. This approach is demonstrated in Coles et al. (2003) for the analysis of rainfall data. The spatial and temporal variability can be analysed quantitatively, if

data is available in sufficiently small scale. A data-set showing the spatial distribution of rockfall events is presented in Dussauge-Peisser et al. (2002). Spatial variability can be described by the spatial correlation of the relevant characteristics. In most practical cases, however, a simplified approach is favourable, whereby smaller areas are determined within which the spatial variability can be neglected. Temporal (typically seasonal) variability can be described by time-dependent parameters in the exceedance frequency model, corresponding to the assumption that the hazard event (e.g. rockfall) follows an inhomogeneous Poisson process.

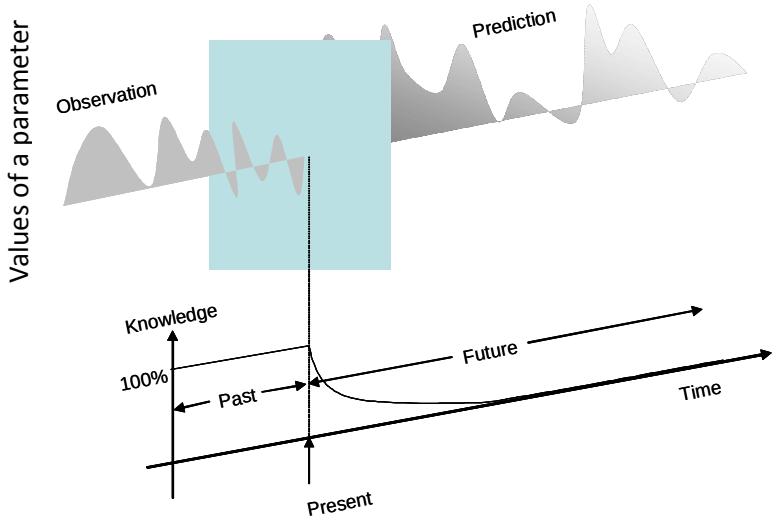

Figure 5: Illustration of the time dependence of knowledge.

It is interesting to notice that the type of uncertainty associated with the state of knowledge has a time dependency. This is especially relevant in the context of uncertainties that evolve over relatively longer reference time periods as is the case in climate change analyses. Following Figure 5, it is possible to observe an uncertain phenomenon when it has occurred. In principle, if the observation is perfect without any errors, the knowledge about the phenomenon is perfect. The modelling of the same phenomenon in the future, however, is uncertain as this involves models subject to natural variability, model uncertainty and statistical uncertainty. Often but not always the models available tend to lose their precision rather fast so that phenomena lying just a few days or weeks ahead can be predicted only with significant uncertainty. An extreme example of this concerns the prediction of the weather.

The above discussion shows another interesting effect, namely that the uncertainty associated with a model concerning the future transforms from a mixture of aleatory and epistemic uncertainty to a purely epistemic uncertainty when the modelled phenomenon is observed. This transition of the type of uncertainty has a significant importance because it facilitates the fact that the uncertainty is reduced by utilization of observation – referred to as updating.

ii. TREATMENT OF UNCERTAINTIES – A BAYESIAN APPROACH

Generally, uncertainties are best represented through random variables with specified probability density functions and corresponding parameters. If two or more uncertainties can be assumed to be statistically or otherwise dependent, this dependency should be accounted for in the probabilistic

modelling. Statistical dependency may be appropriately represented through correlation. Functional dependency or common cause dependency is appropriately represented through hierarchical probabilistic models (JCSS, 2001).

The treatment of uncertainties can be consistently dealt within the platform of decision making through methods and tools used for decision analysis. Decision making may be defined as the process of selection making a logical choice among several available options. Typical decision problems are subject to a combination of inherent, modelling and statistical uncertainties. In principle, all prevailing types of uncertainties can be taken into account in decision analysis within the framework of Bayesian probability theory; a more detailed treatment of this issue is given in Paté-Cornell (1996) and Lindley (1976). The Bayesian approach provides a basis for the consistent representation of uncertainties independent of their source and readily facilitates the joint consideration of purely subjectively assessed uncertainties, analytically assessed uncertainties and evidence as obtained through observations. Further, a consistent consideration of new knowledge or information when it becomes available is possible in the Bayesian approach through updating. Consistent decision making subject to uncertainties is treated in detail in Raiffa and Schlaifer (1961) and Benjamin and Cornell (1970). Other aspects on decision analysis in engineering applications are treated in Apostolakis (1990), Paté-Cornell (1996), Faber and Stewart (2003) and JCSS (2008).

Depending on the state of information at the time of the decision analysis, three different analysis types are distinguished, namely prior analysis, posterior analysis and pre-posterior analysis; these analysis methods provide the basis for the treatment of uncertainties. A description of these analysis methods and their use in the representation of uncertainties can be found in deliverables D0.3 and D5.4 of the SafeLand project Safeland D0.3, 2011 and Safeland D5.4, 2011. A summary of the three analysis methods is provided below.

The simplest form of the decision analysis is prior analysis. In the prior analysis, the risk (or expected utility) is evaluated on the basis of statistical information and probabilistic modelling available prior to any decision and/or activity. The representation of uncertainties is hence made on the basis of the existing information about the different variables in the analysis; however, as the realisations concerning the decision and/or activity have not occurred yet, the probabilistic modelling involves both aleatory and epistemic uncertainties. The distribution parameters used to quantify uncertainties in variables are initially modelled by prior distribution functions.

Posterior decision analysis is in principle of the same form as the prior decision analysis, however, changes in the branching probabilities and/or the consequences in the decision tree reflect that the considered problem has been changed as an effect of e.g. risk reducing measures, risk mitigating measures and/or collection of additional information. The posterior decision analysis provides a means for the utilization of new information in the decision analysis – referred to as updating. By the application of the Bayes' theorem (see e.g. Lindley, 1976) the prior distribution functions, assessed by any mixture of frequentistic and subjective information, are updated and transformed into posterior distribution functions.

The third type of decision analysis is the pre-posterior analysis. Using pre-posterior decision analysis, optimal decisions in regard to information collection activities which may be performed in the future can be identified. Pre-posterior decision analysis is described in Raiffa and Schlaifer (1961) and Benjamin and Cornell (1970). The principle behind the pre-posterior decision analysis is that the outcomes of planned information collection activities are assumed to follow the prior probabilistic

model of uncertainties. Based on these assumed outcomes and taking into account any uncertainties associated with the observation and/or interpretation of the outcomes, posterior decision analyses are performed. The corresponding risks are thereafter weighed with their probability of occurrence, again based on the prior probabilistic modelling. The pre-posterior decision problems may hence be seen as a series of posterior decision problems for which the optimal solutions are averaged out over the entire prior uncertainty, with the analysis made before new information is actually collected. The formulation of each of the posterior decision problems is based on an updated probabilistic model of the prevailing uncertainties assuming a given 'outcome of nature'.

It is important to differentiate between the different types of uncertainty in the probabilistic modelling of uncertain phenomena. Only when the origin and the nature of the prevailing uncertainties are fully understood, a consistent probabilistic modelling can be established allowing for rational decision making by means of posterior and pre-posterior decision analysis.

The risk assessment and management of large scale natural hazards such as landslide and rockfall events requires a systematic and consistent representation and management of information for a typically complex system with a large number of constituents or sub-systems and time-varying trends and properties. Such representation must enable a rational treatment and quantification of the various uncertainties discussed earlier; these uncertainties can be associated with the constituents as well as the system. The consistent handling of new knowledge about the system and its constituents as and when it becomes available and its use in the risk assessment and decision making process is also essential. Further, the numerous dependencies and linkages that exist between different constituents of the system need to be systematically considered. The above requirements and considerations necessitate the use of generic risk models for the assessment and management of risks due to natural hazards. The use of Bayesian Probabilistic Networks (BPNs) has proven to be efficient in such risk assessment applications (Bayraktarli et al., 2005, 2006; Faber et al., 2005; Faber et al., 2007; Graf et al., 2009; Nishijima and Faber, 2007; Straub, 2005 and Schubert et al., 2005). A description of the principles and use of Bayesian Probabilistic Networks can be found in Jensen (2001).

SECOND PART - Application to test sites in Europe

1. NORWAY

a. Site Presentation

The Nedre Romerike area included in this study comprises the following municipalities which are part of the county of Akershus: Fet, Gjerdrum, Nannestad, Rælingen, Skedsmo, Sørum and Ullensaker. They cover around 1200 km². This region lies to the East of Oslo, the capital of Norway. The total population in 2010 was about 160 000 habitants, which constitutes more than 30% of the total population of Oslo suburbs. In addition to the urban areas, Nedre Romerike includes important industrial and agricultural areas. Land use plans from authorities consider urban expansion for the next 100 years. The study area is widely covered with marine deposits (clayey soils), and many slopes with marginal safety. The main triggering factors for landslides are human activity (anthropic) and precipitation.

Figure 6: Localisation of the Norwegian site

This region of Norway enjoys a humid continental climate (according to the Köppen climate classification system). Despite its northerly location, the climate is relatively mild throughout the year because of the Gulf Stream.

The south-east regions have pleasantly mild to warm summers with average high temperatures of 20–22 °C (68–72 °F) and lows of around 12 °C (54 °F).

Annual precipitation is 800 millimetres with moderate rainfall throughout the year. Snowfall can occur from November to April, but snow accumulation occurs mainly from January through March.

Landslides are frequently caused by precipitation events that exceed a certain threshold value of rainfall intensity. 35 landslides were registered in the database. The majority of the slides were located in the two counties Akershus and Buskerud. Many of them occurred near rivers and lake shores.

b. Assessment of landslide susceptibility (BRGM)

i. Data preparation

1. General GIS data

Table 1 : List of GIS data available on the study area

Theme	ArcGIS storage	Feature type	Information
Landslides Inventory	Shapefile	Point	It presents those landslides that were reported since 1973, most likely only those that affected population, roads or railways.
Land cover	Shapefile	Polygon	
Municipal boundaries	Shapefile	Polygon	Municipal boundaries selected County Akershus
Water Courses	Geodatabase	Polygon & Polyline	with object types : River, perennial brooks, no perennial brooks, channels, lakes
Quaternary deposits	Shapefile	Polygon	Surficial deposits
Terrain	Shapefile	Polygon	1 m contours
DEM 10 m	Raster	/	After an interpolation method specifically designed for the creation of hydrologically correct digital elevation models (DEMs) (ArcGis Tools)

First, elevation values were interpolated according to the topographic map of the area for a DEM 10 m with an ArcGIS tool. This method imposes some constraints to ensure that the digital elevation model is hydrologically correct. In other words, it contains a connected drainage structure and represents ridges and streams correctly from input contour data. All sink points were removed in the output DEM that have not been identified as sinks in the input sink feature dataset.

Based on this corrected DEM file, slope inclination and the direction of the flow for each cell of the area have been computed.

2. Lithological model

Regarding lithology, the area was divided into two parts:

- the bedrock (old, stable)

- Sedimentary deposits (most recent, unstable)

The bedrock corresponds to the high altitude parts of the DEM. It is a hard granite formation that is not conducive to the occurrence of landslides. Locally, the bedrock can be covered by thin Quaternary formations, which are not likely to generate large landslides.

In this study, only sedimentary deposits are supposed to be triggered by rainfall events. The sedimentary deposits selected in the map are listed in Table 2:

Table 2: List of unstable formations selected for analysis

Lithology code	Name
35	Lacustrine deposit
50	River deposits, unspecified
54	Flood deposits, continuous
55	Flood deposits, non-continuous/thin
81	Slide material
41	Marine and fjord deposits, continuous, locally thick
42	Marine and fjord deposits, continuous
43	Marine and fjord deposits, non-continuous/thin

Crossing the landslides inventory with the map of surficial deposits shows that 29 inventoried landslides happened in the “Marine and fjord deposits, continuous, locally thick” formation and one in the “river deposits or unspecified” formation. The remaining five landslides are in formations outside of the selected formations.

Most of the landslides from the inventory occurred in the same geological unit[1] and most of them occurred during the same period: autumn 2000, but according to the experts, they can be considered representative for the area.

[1] Therefore, in the following sections, "study area", would mean "area of surficial deposits" favourable to landslides.

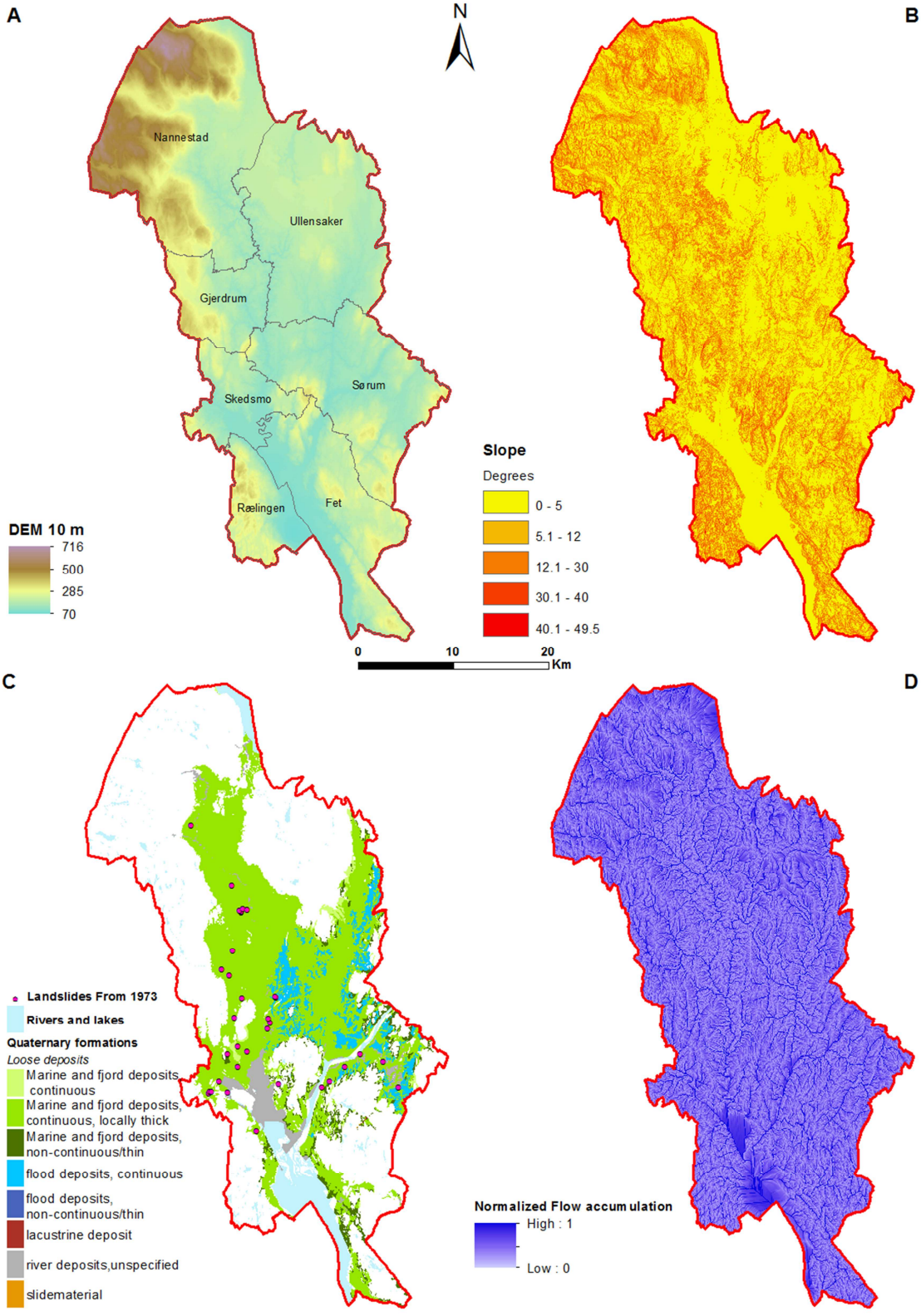

Figure 7: Main data used in the model: A) elevation model (resolution: 10 m); B) slope map; C) surficial deposits and landslides inventory; D) flow accumulation map

3. *Geological and geotechnical parameters*

Insofar as only few geotechnical data were available for the whole area, a simple geological model was applied by considering a single geotechnical zone on the site. This zone is represented by a soil column made of 2 layers called soil units. Each soil unit is characterized by its thickness and its geotechnical parameters (cohesion, friction angle and dry density).

For the area, a typical profile of two soil units was used. The first layer is the upper part of the ground which was weathered due to weather conditions and has so a low cohesion and is highly permeable. The second layer includes unweathered marine clay layers.

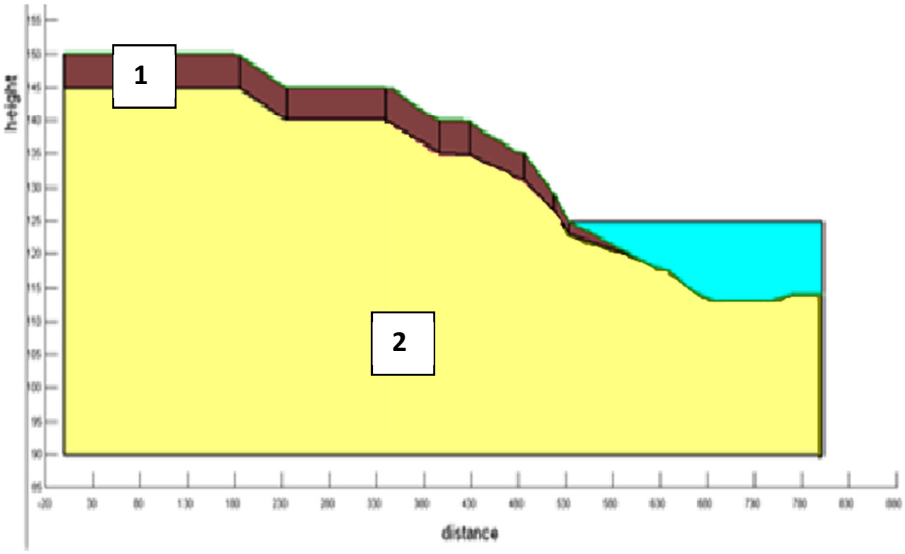

Figure 8: Typical profile of the study area: layer one (brown color) is the upper weathered layer and layer two (yellow) consists of Marine clay blocks. Adapted from Rességuier (2006).

Some geotechnical parameters provided by Resseguier (2006) for a typical profile of this zone, have been modified in order to create the geotechnical model finally used as input in ALICE. These parameters, listed in Table 3, take also into account some uncertainties in their heterogeneities and their spatial distribution (see paragraph on uncertainties) for the cohesion and friction angle of the first layer, assuming triangular distributions. The Apex value is supposed to be the most likely. As landslides are assumed to occur inside the first layer, heterogeneities in the second layers are less important to be taken into acocunt and can be assumed to be constant.

Table 3: Geotechnical parameters and their distribution law

	Cohesion (kPa)			Friction angle (°)			Dry density (kN.m^3)		
	min	apex	max	min	apex	max	min	apex	max
Upper weathered crust	0	1	2	20	21	22		18	
Marine clay blocks		15			25			19	

The thickness of the first layer was estimated with a method similar to the one described in the report of NGI (Resseguier 2006), in order to have it around 3.5 m for the plateau flat zones, decreasing in the slope, and around 0 m in the bottom of the ravines. The resulting formula is the following one:

$$D = (H-88)*(3.5/136) \quad \textbf{(7)}$$

Where :

- D is the depth of the layer studied (corresponding to its thickness) (in m)
- H is the elevation of the point where the thickness is computed. (in m)

The thickness of the upper layer is therefore spatialized (Figure 9) and used to estimate the magnitude of fluctuation of the water table. The water table level in our study is assumed to vary between the bottom and the top of the upper crust.

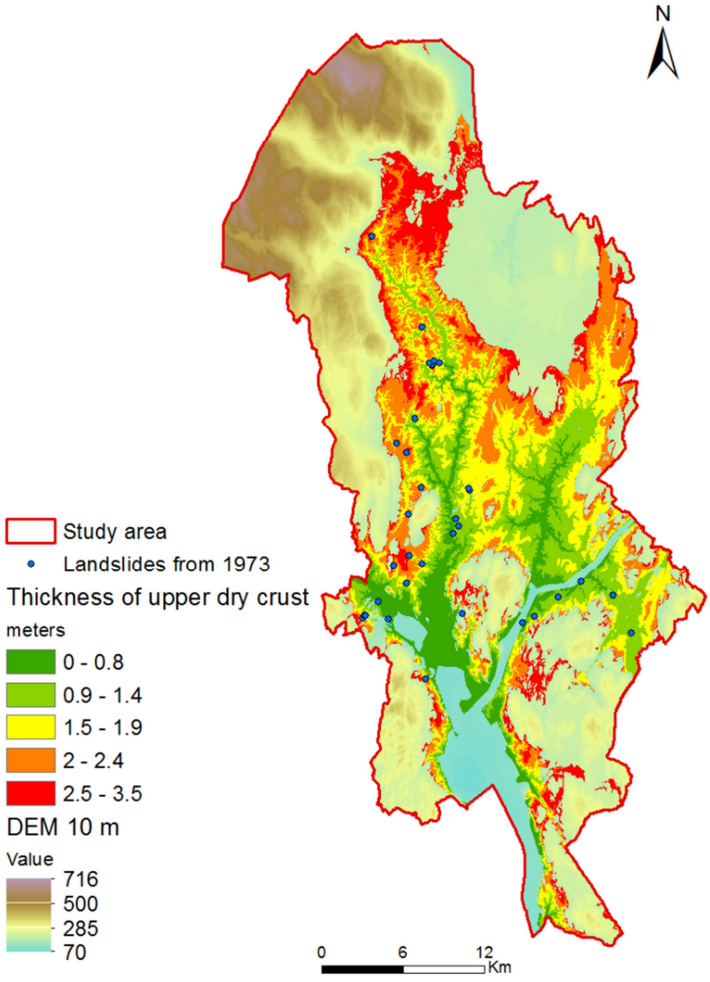

Figure 9: map of thickness of the upper layer

ii. Modelling scenarios

In this case, due to scarcity of observed hydrological data, only ALICE software has been used.

The methodology was tested using 3 different water table scenarios. These scenarios cover the two extreme cases: the minimum water level (filling ratio=0), corresponding to a drought period and the maximal one (filling ratio=1), corresponding to period of heavy and lasting rainfall; and an average situation (filling ratio=0.5).

Insofar as hydrologic system of the area is only known on few points, simple assumptions have been made concerning the variation of the water table level. Hence, the bottom of the dry crust corresponds approximately to the minimum (shallowest) depth of the ground water table (Figure 11). This dry situation is simulated using a filing ratio of 0. However, during extreme infiltration events (extreme precipitation, intense snow melt), the ground water table can reach the ground surface. Below the dry crust there is saturated clay. The maximum water table level, simulated using a filling ratio of 1, is consistent with the elevation model (Figure 12). This assumption is not fully realistic but it permits to provide conservative results.

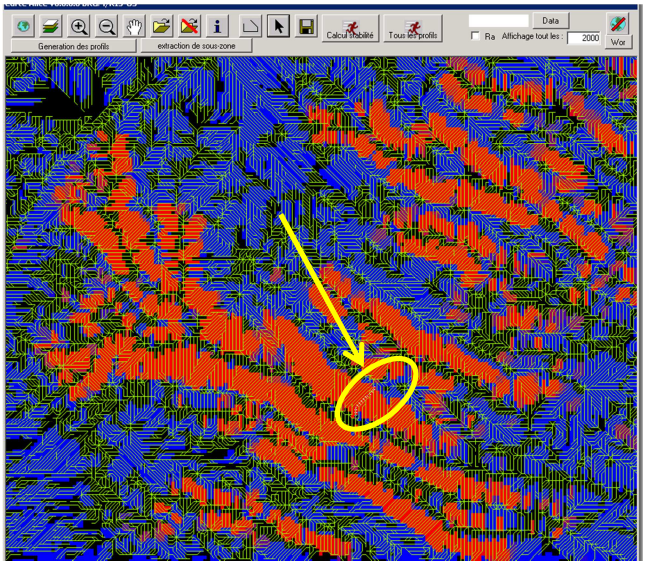

Figure 10 : location of a test profile (red color: high probability of instability, blue low probability)

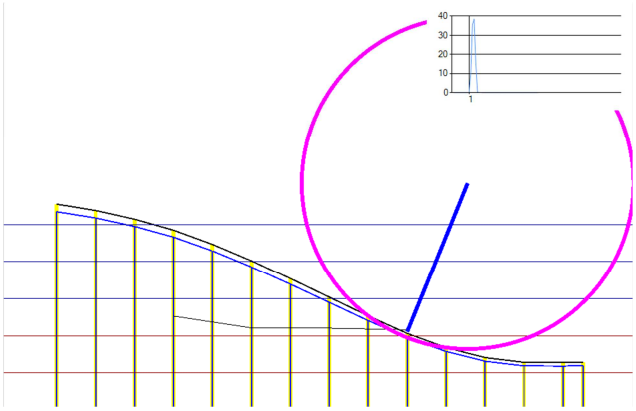

Figure 11: example of result obtained on a typical profile for a drought period (water table is represented in blue). The circle represents the less favourable situation on the profile.Graph in the upper right part shows the distribution of the Safety Factor. Safety factor is always above 1, so probability of instability is null.

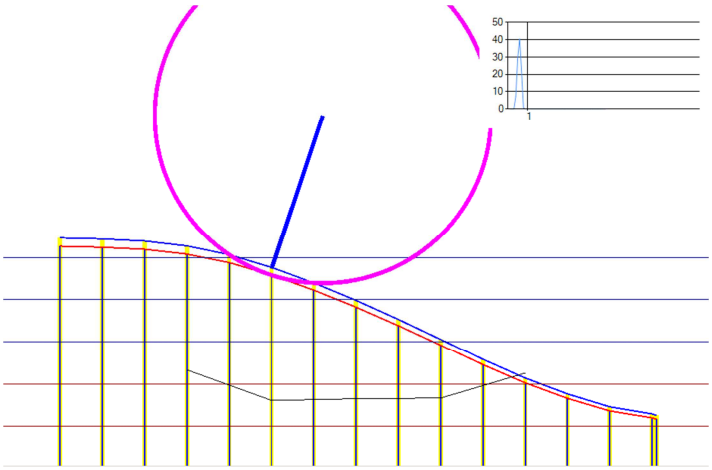

Figure 12: example of result obtained after a heavy and lasting rainfall period (water table is represented in blue). The circle represents the more unstable situation and in this case, its occurrence probability is 1.

Landslides' length and depth are parameters defined for the whole studied area for an ALICE® run. The word "length" is used to define the size of the landslide initiation zone and not the propagation length. As no field observations were planned in the project and the inventory of landslides do not always provide a length, several simulations with different landslides' length from 30 m to 75 m were conducted and the resulting landslides' occurrence probability maps were compared.

To reduce the computing time, the ALICE ® software allows to specify a minimum slope (in degrees) from which the calculation of safety factor will be realized. As the study area is relatively flat, a value for this minimum slope was assigned very low (0.5 °) in order to take into account a maximum number of profiles.

After the first calibration tests for the geotechnical parameters, 50 runs were realized for different lengths of landslides between 30 and 75 m and each time for three different filling ratios. In the end, 1200 runs were performed in our study area.

iii. Final hazard landslide mapping

For a given filling ratio for each profile of the study area, the software calculates safety factors for several landslide positions. The probability of having the safety factor below one represents the probability of occurrence of the landslide for a given triggering scenario (i.e. landslide geometry and water table level). The dispersion of the distribution gives the uncertainty of the result (see paragraph on uncertainties before). The calculated probability of occurrence is then attributed to all pixels of the result raster located on the profile and intersecting the landslide geometry. Thus a pixel receives as many probabilities as landslide positions it is included in. Finally, a map is created, displaying the highest calculated probability of occurrence for each pixel of the studied area.

After comparing the landslides occurrence probability maps obtained for different landslides' lengths, the safety factors calculated for lengths of about 35 to 40 meters seem more realistic with regard to the landslide inventory provided. Figure 13 shows three landslides occurrence probability maps resulting from the simulations using the 3 different filling ratios and a landslides' length of 35 meters.

These results show that, as expected, an increase of the water content of the soil induces a reduction in the safety factor, and a decrease in the water level makes the slopes more stable.

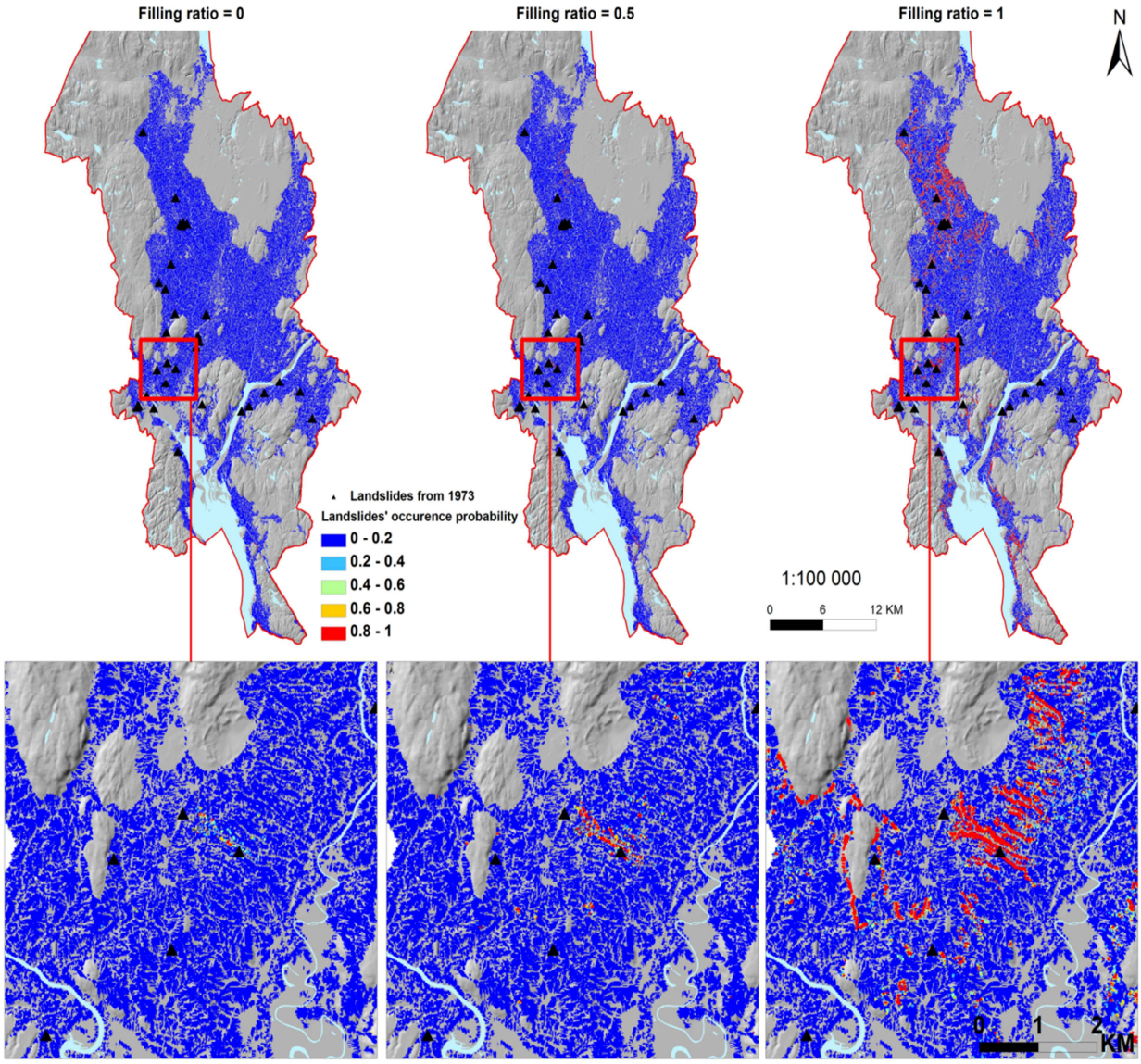

Figure 13: Representation of the probability of occurrence resulting from the simulations using the 3 different filling ratios and a landslides' length of 35 meters.

c. Evolution of landslide hazard (ICG/NGI)

i. Slope factor Sr

The slope factor represents the natural landscape ruggedness within a grid unit. For calculating the slope angle, a terrain model was prepared based on 1-m contour lines, which are part of the official 1:5 000 scale maps of all Norway.

The classification of slope and the estimated susceptibility factors are shown in Table 4. The ranges of slope angles are the same as in SafeLand D2.10 and D3.7. The susceptibility factors were obtained using Eq. (3) and the criteria listed in the section "1.c". The spatial distribution of slope classes in the study area is shown in Figure 14.

Table 4: Slope angle ranges and corresponding susceptibility factors

Slope (degrees)	S_r
0-1	0
1-6	1
6-12	3
12-18	4
18-24	5
24-40	4
40-45	0
45-90	0

Note: for slopes angles less than 1° (i.e. for flat or nearly flat areas), S_r is set equal to zero because the resulting landslide hazard is zero even if the other factors are favourable. For slope angles more than 40°, S_r is also equal to 0 because it is assumed that no material susceptible for landslide can be found in this context.

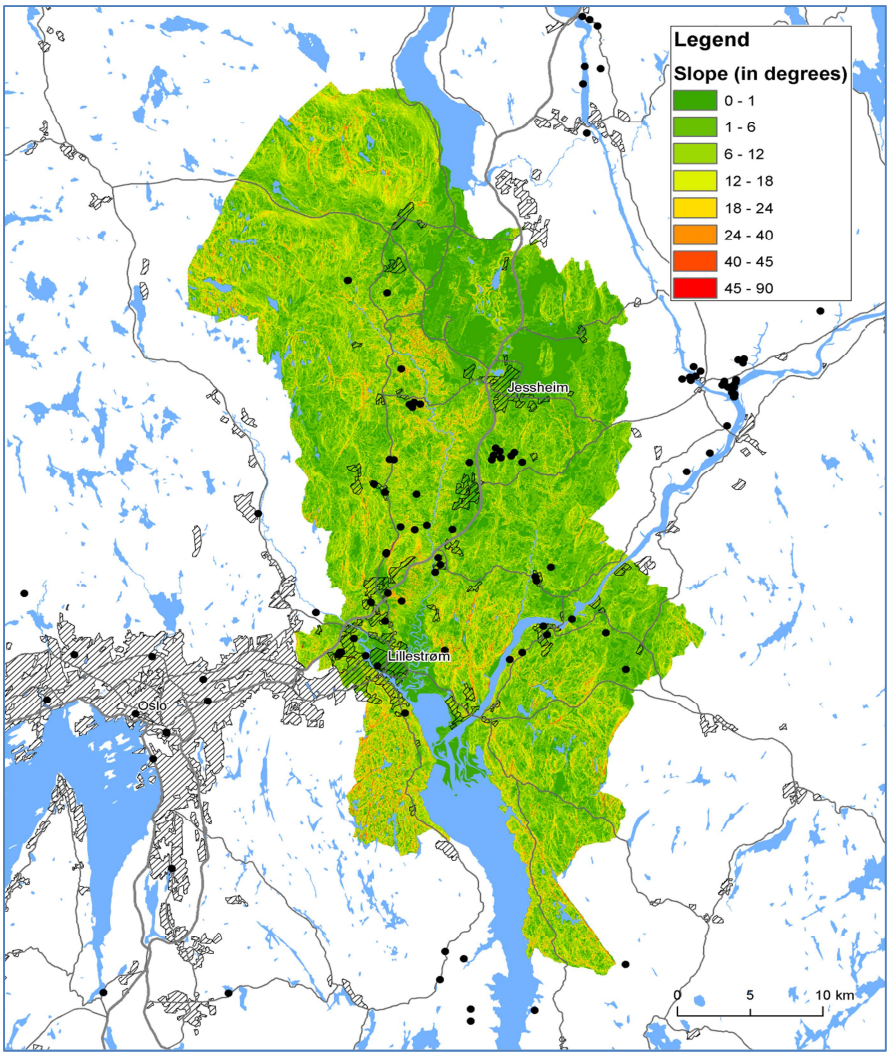

Figure 14: Slope classes used for the slope susceptibility factor Sr for the study area. Black circle markers are landslides from the Norwegian inventory of landslides.

ii. Lithology factor Sl

This is probably the most difficult parameter to assess. Physically-based susceptibility models require detailed geotechnical information, which is generally difficult to parameterize in regional assessments due to the limited availability of data and the high spatial variability of the geotechnical properties. In the model used in this evaluation a geological description is required, preferably classifying materials based on their expected levels of characteristic shear strength.

The type of landslides considered for this assessment occurs mainly on marine deposits (generally silty clays). A typical event is shown in **Erreur ! Source du renvoi introuvable.**.

Figure 15. Typical landslide on marine deposits, similar to the ones included in the inventory used in the present study (Jaedicke and Kleven, 2008).

In order to illustrate the spatial variability of the geotechnical parameters in the marine deposits used in the study area (both in depth and horizontally), a cross-section is presented as an example in **Erreur ! Source du renvoi introuvable.**.

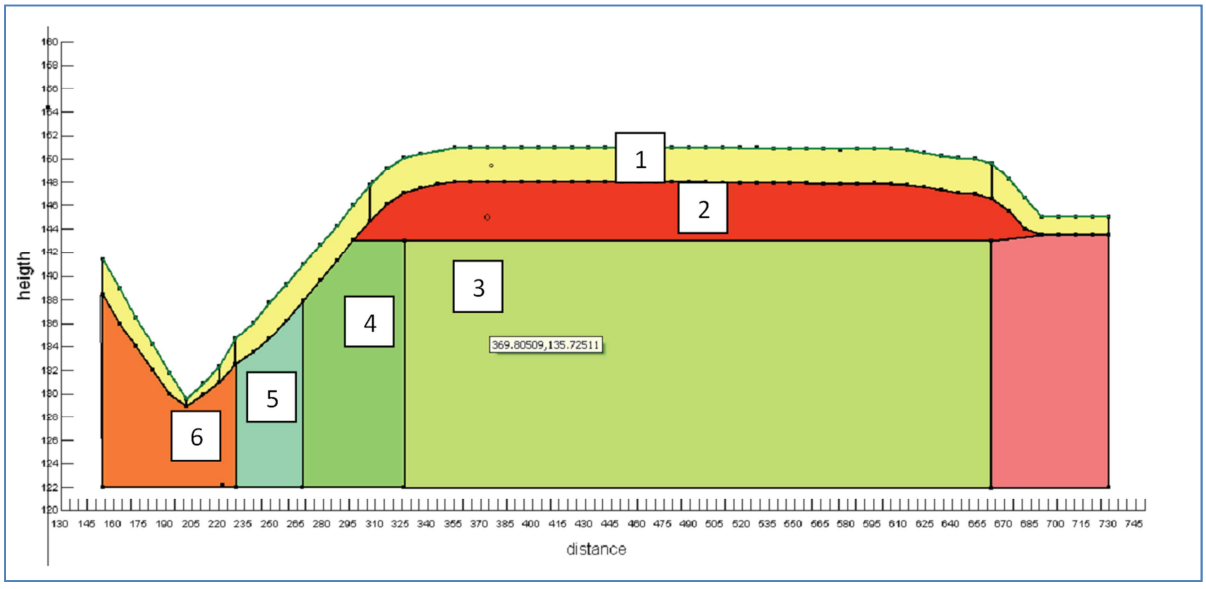

Figure 16: Example of cross-section of a site with marine deposits in the study area. Layering and dimensions in the Figure are only illustrative and are not intended to be interpreted as average or predominant conditions in the study area. The numbered units are described in the text. Adapted from Rességuier (2006).

A description of the cross-section presented in Figure 16 follows (the numbers in parentheses refer to the labels of the units in the cross-section). The profile consists of a weathered dry crust at the top **(1)**.

The bottom of the dry layer corresponds approximately to the minimum (shallowest) depth of the ground water table. However, during extreme infiltration events (extreme precipitation, intense snow melt), the ground water table can reach the ground surface. Below the dry crust there is saturated fine-grained soil (e.g., silty clay). Due to differences in overburden depths along the slope, associated to the former seabed level, the clay in the upper parts of the slope **(2 & 3)** is normally consolidated or slightly overconsolidated, and the overconsolidation increases towards the bottom of the slope (gradually towards, **4, 5** and **6**). The differences in overconsolidation are reflected by increasing undrained shear strength as one moves down the slope. It should be noticed that in an actual situation, the evolution between units 3, 4, 5 and 6 is progressive, the vertical boundaries are only for illustration purposes.

Estimation of material properties and their range of variability in the different units are presented below. These are, therefore, not intended to be interpreted as average or predominant conditions in the study area:

- Upper dry layer **(1)**:
  - Thickness: 2 to 5 m in the upper part of the slope; ~0 m at the lower part of the slope (bottom of a ravine or a river)
  - Shear strength:
    - Cohesion: 0 to 5 kPa
    - Friction angle: around 32 degrees
  - Unit weight: 18 kN/m^3
- Clay:
  - Unit weight: 19 kN/m^3
  - Along plateau **(2)**:
    - Thickness: 4 to 6 m
    - Undrained shear strength: 20-50 kPa (constant with depth)
  - Upper part of slope **(3)**:
    - Undrained shear strength at the top of layer: 20-50 kPa
    - Rate of change with depth: 3.5 kPa/m
  - Middle-upper part of slope **(4)**:
    - Undrained shear strength at the top of the layer: 25-55 kPa
    - Rate of change with depth: 3.6 kPa/m
  - Middle-lower part of slope **(5)**:
    - Undrained shear strength at the top of the layer: 30-65 kPa
    - Rate of change with depth: 3.9 kPa/m
  - Lower part of slope **(6)**:
    - Undrained shear strength at the top of the layer: 35-75 kPa
    - Rate of change with depth: 4 kPa/m

From the above list, it is seen that the strength parameters can have wide variations both spatially (horizontally and vertically) and due to the intrinsic properties of the material, its current state and the stress history (as reflected by the listed ranges of variation of strength at the top of the layers). Two additional aspects that are also important and have not been included here are: the effects of strength anisotropy when moving from the active to the passive parts of the slope; and the effect of the sensitivity of the soil (ratio between the intact and remoulded shear strength) in reducing the characteristic shear strength relative to non-sensitive soils.

There are no available datasets in the case study area for defining the spatial distribution of ground conditions with the level of detail presented in Figure 16. The best representation of ground conditions at regional scale is provided by the quaternary maps. This is a vector (polygon) dataset mostly prepared by digitizing 1:50 000 maps produced by the Norwegian Geological Survey NGU. The quaternary map for the area of interest is shown in Figure 17. The description of the lithological units is presented in Table 5.

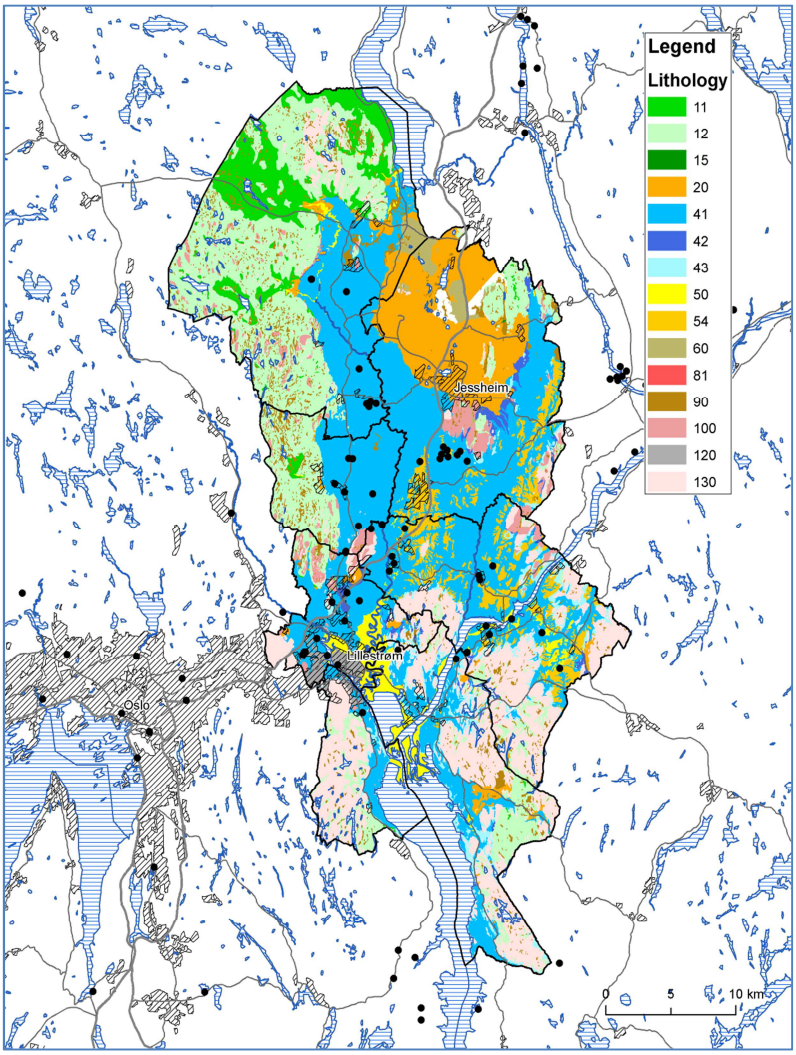

Figure 17: Quaternary map of the study area based on the digitization of 1:50 000 maps. Source: Norwegian Geological Survey – NGU. Black circle markers are landslides from the Norwegian inventory of landslides.

Table 5: Lithological units in the study area: description and susceptibility factor S_l

Code	Description	S_l
11	Moraine material, continuous, locally thick	1.3
12	Moraine material, non-continuous/thin	1.5
15	Terminal moraine	2.3
20	Glaciofluvial deposit	1.9
41	Marine and fjord deposits, continuous, locally thick	3
42	Marine and fjord deposits, continuous	2.5
43	Marine and fjord deposits, non-continuous/thin	2.4
50	River and stream deposits, unspecified	2.7
54	Flood-plain deposits, continuous	3
60	Aeolian? Deposits	1.5
81	Landslide material, continuous, locally thick	1.5
90	Peat and marshland (organic material)	1.9
100	Humus blanket/thin peat blanket overlying bedrock	2.1
120	Fill (anthropogenic material), unspecified	2.9
130	Bare rock	1.7

The type of landslides which is relevant for the study area consists of earth slides, which occur in silty clays deposited in a marine environment. Therefore, the units with the 6 highest scores are related to the presence of marine sediments (units 50, 54 and 120 are often overlying marine sediments, especially on shoreline and riverbank areas).

iii. Land cover index Sv

The source for the land cover index S_v was the CORINE Land Cover (CLC) database. This is a seamless European land cover vector database which was completed by the Norwegian Forest and Landscape Institute in 2008. The calibrated susceptibility factors are presented in Table 6 and the current distribution of land cover is shown in Figure 18.

Table 6: Classification of land cover for the hazard analysis

Land cover class	S_v
Water	0
Marshland	0.1
Forest	0.4
Sparsely vegetated areas	0.8
Crops	1.1
Urban	1.2

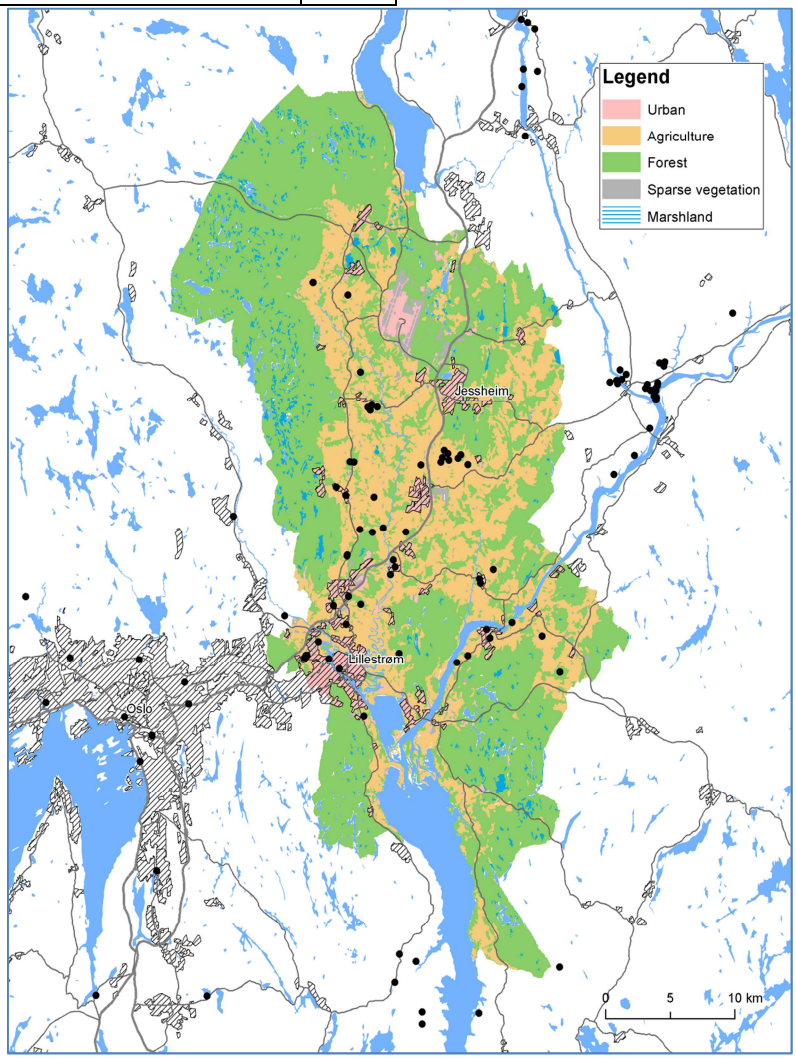

Figure 18: Land cover map of the study area as of 2008 based on the CORINE Land Cover database. Black circle markers are landslides from the Norwegian inventory of landslides.

The land cover was projected up to the year 2090 based on the current land cover dataset. The population of the region is expected to increase by 50% by 2040, resulting in a substantial growth of urban land cover. Plans from the Akershus county to which all municipalities belong indicate that a

majority of this growth is expected in central towns, described as tie-points for communication. Though not a single list of tie-points exists yet, assumptions were made that the tie-points will be the largest of the existing towns. Smaller towns and villages will most likely see smaller changes. For this study, the urban growth was therefore modelled for the largest urban areas. For each 20-year period, these urban areas were expanded by a certain distance. Urban growth was limited by excluding water features. In addition, the urban area representing Oslo Airport was kept constant, even though an expansion is expected around 2030-2040. The model was calibrated versus expected area of the urban growth and versus plans for urban development of Skedsmo municipality for 2050. The spatial distribution of land cover evolution over the period 2010 to 2090 is presented in Figure 19 and the evolution for each class is shown in Figure 20.

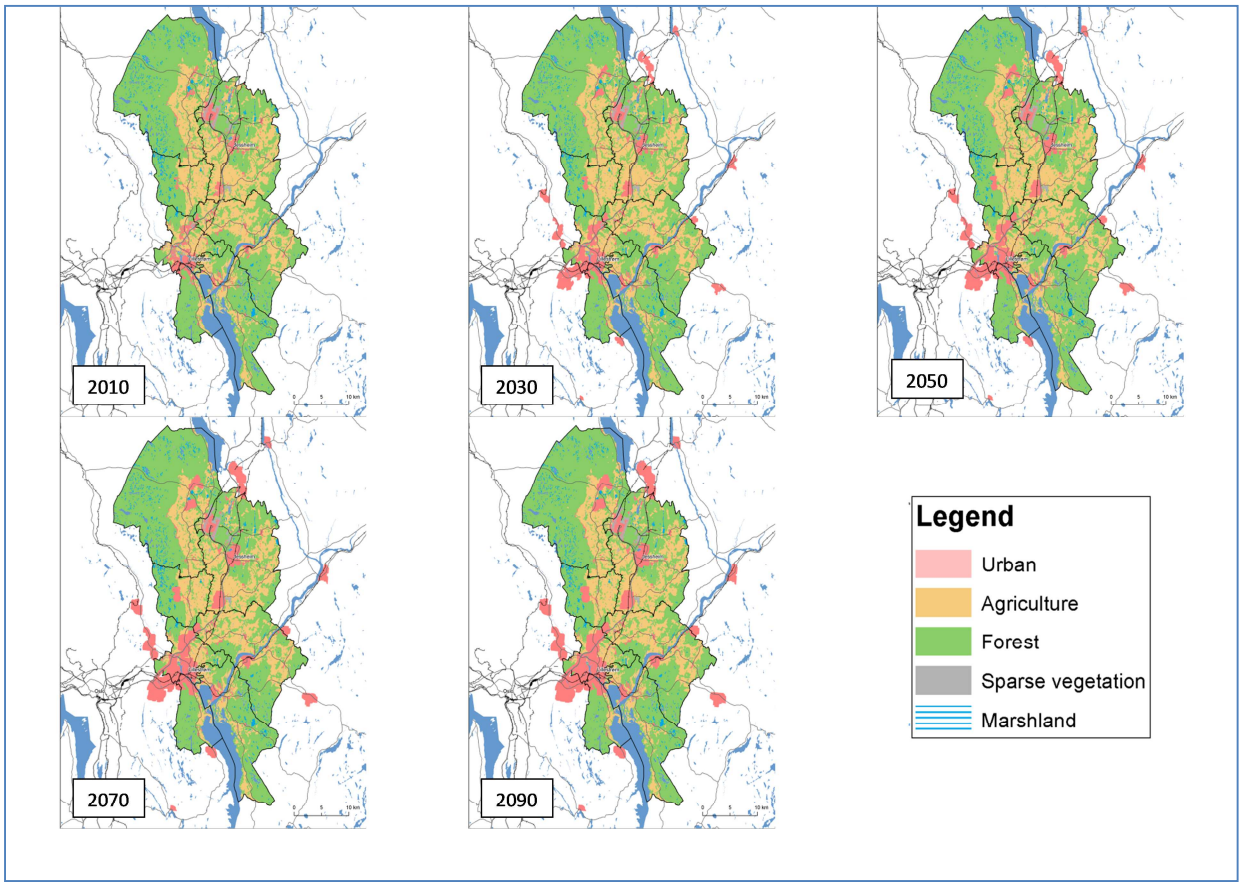

Figure 19. Land cover evolution within the period 2010-2090 in the study area.

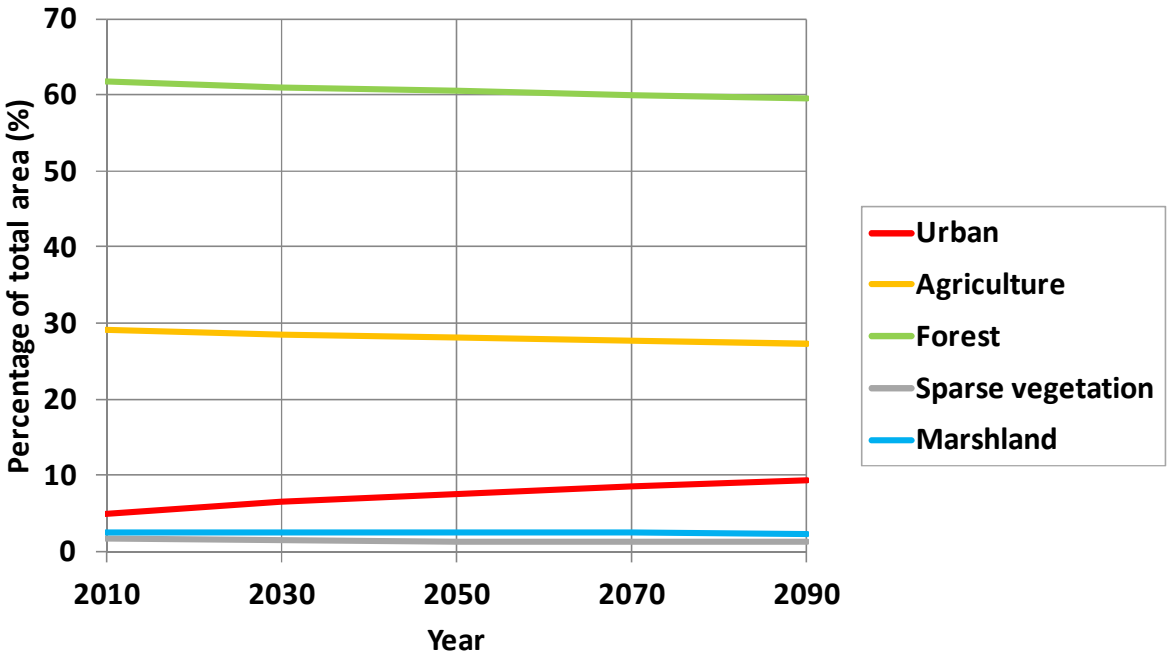

Figure 20: Evolution of land cover classes over the period 2010-2090.

iv. Precipitation trigger factor Tp

The starting point for defining the precipitation triggering factor was establishing the critical duration of triggering precipitation for the type of landslides considered in the study area. In the European scale assessments, it has been assumed that 1-day precipitation provides the necessary criterion for landslide initiation at continental scale. The SafeLand Deliverable D1.5 analysed the threshold conditions for the same inventory of landslides considered in the present hazard assessment. After analysing daily precipitation data for a 30-year period for both landslide and no-landslide days, and after considering accumulations of precipitation ranging between 1 and 360 days, the assessment concluded that the critical duration of precipitation for initiating landslides in the study area is 46 days, which was somehow expected considering the low infiltration capacity in the predominantly fine grained soils (mostly silty clays). The variation of the misclassification error (ratio of misclassified events – both false alarms and missed events – to total number of events) and the number of days of accumulated precipitation is shown in Figure 21.

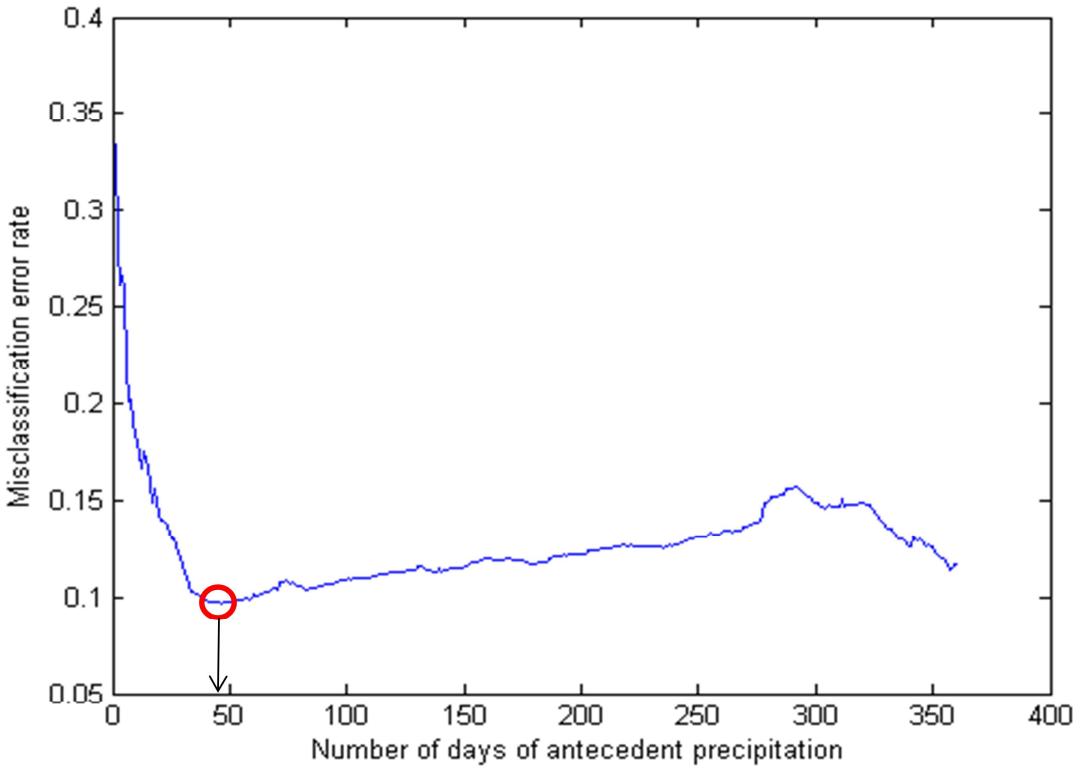

Figure 21: Misclassification error rate vs number of days of antecedent precipitation. The critical duration corresponds to the minimum error, as indicated by the red circle and corresponding to 46 days. Adapted from SafeLand D1.5.

The class boundaries for the precipitation triggering factor used in D2.10 and D3.7 were based on 1-day precipitation, so these cannot be used directly here for values based on 46-day accumulated precipitation. The approach that was followed is to map approximately the class boundaries based on the correlation between the 1-day and 46-day values. This correlation for the 99.9% percentiles is shown in Figure 23.

In order to be consistent with the European scale assessments in D2.10 and D3.7, the categorization of T_p was based on the estimate of the 99.9% percentile of 46-day precipitation for 20 year periods. The time series were provided as daily data from SafeLand Deliverable D3.3. The procedure for obtaining the precipitation triggering factor T_p was the following: Calculate the accumulated 46-day precipitation for each cell (374 cells) and each day in the time series (21900 days).

- Calculate 99.9% percentile for the different 20-year periods at each cell.
- Analyse 99.9% percentiles for 46-day and 1-day precipitation for adjusting class boundaries based on reclassification used in D3.7.
- Adjust precipitation triggering factor T_p for each cell and each 20-year period.
- Reclassify 99.9% perc. of 46-day precipitation to obtain T_p.

The spatial distribution of the 99.9% percentile of 46-day precipitation in the study area for years 2010, 2030 and 2050 is shown in Figure 22. It can be noted that the spatial distribution is very similar for all three periods, with the highest accumulations to the north west of the study area, and the lowest to the south east.

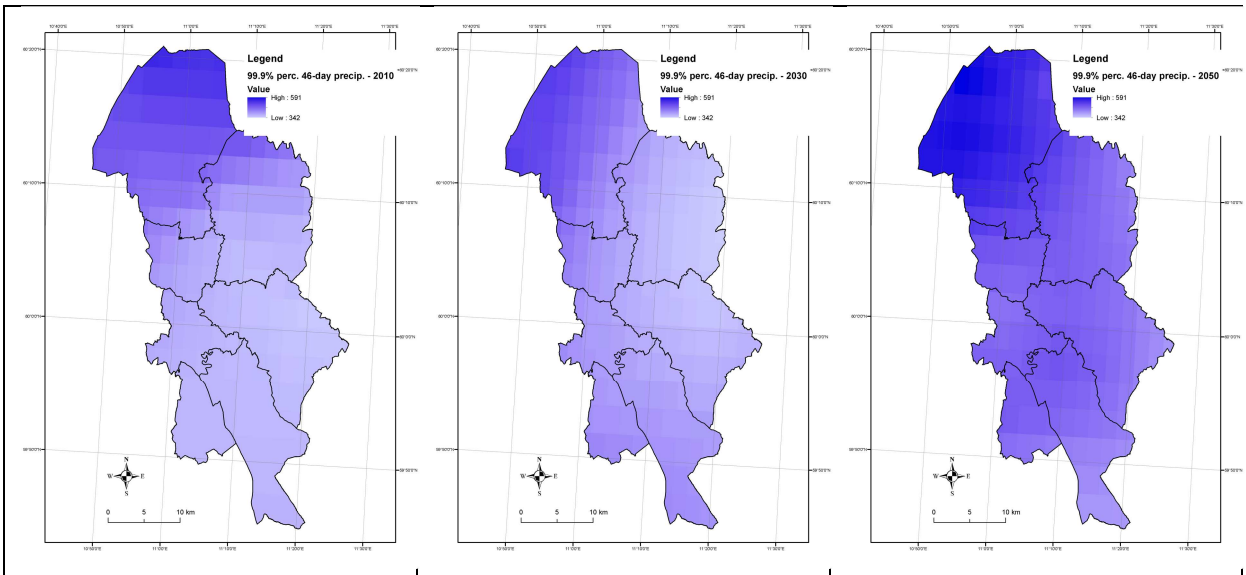

Figure 22: Spatial distribution of 99.9% percentile of 46-day precipitation in the study area based on 20 year time series. The colour bars are stretched to the minimum and maximum values in the period, 342 and 591 mm.

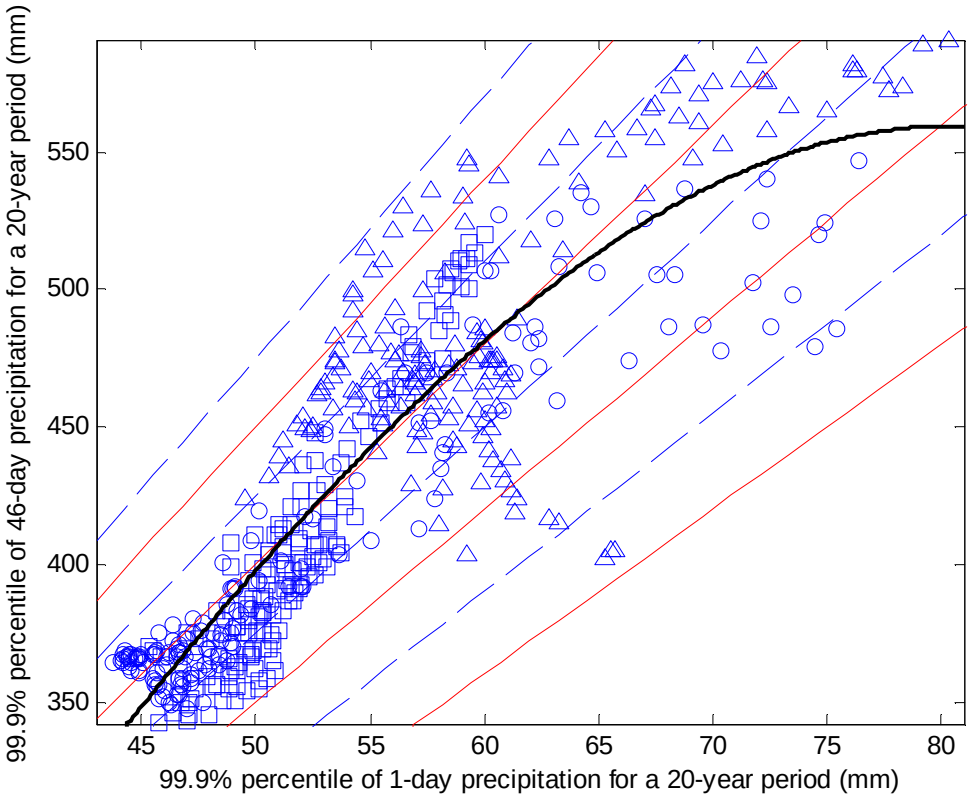

Figure 23: Pixel-by-pixel correlation between 99.9% percentile of 1-day and 46-day precipitation. Circle, square and triangle markers correspond to scenarios in 2010, 2030 and 2050, respectively. The red solid lines represent ratios of 46-day to 1-day precipitation from 6 (lowest) to 9 (highest). The blue dashed lines represent ratios of 6.5 to 9.5. The black solid line is the best fit of the data to a second degree polynomial.

On the basis of the estimated 99.9% percentile of 46-day precipitation for 20 year periods (**Erreur ! Source du renvoi introuvable.**) and the pixel-by-pixel correlation of 46-day and 1-day precipitation (Figure 23) a precipitation index T_p was assigned as listed in Table 7.

Table 7: Reclassification of precipitation triggering factor Tp for the study area.

Classes 1-day precipitation – D3.7 (mm)	Classes 46-day precipitation (mm)	Susceptibility	T_p
0 – 60	0 – 480	Low	1
60 – 75	480 – 550	Moderate	2
75 – 95	550 – 700	Medium	3
95 – 120	700 – 880	High	4
120 -	880 -	Very high	5

The spatial distribution of the precipitation triggering factor T_p in the three scenarios at 2010, 2030 and 2050 is presented in **Erreur ! Source du renvoi introuvable.**.

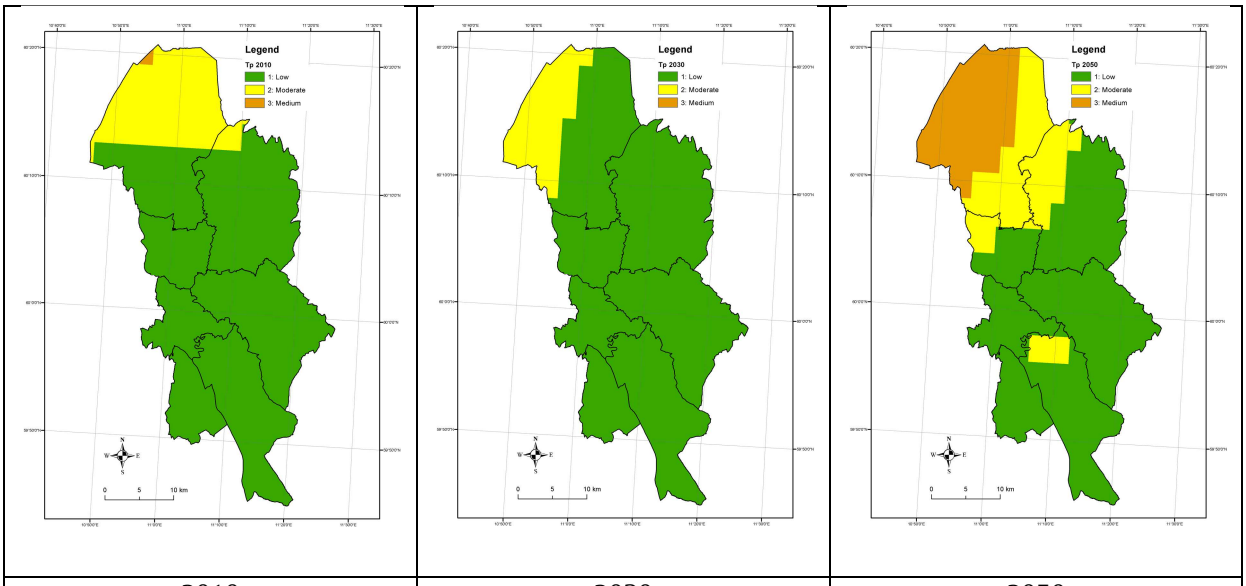

2010	2030	2050

Figure 24: Spatial distribution of precipitation triggering factor Tp in the study area based on the 99.9% percentile of 46-day precipitation (Figure 22) and the reclassification presented in Table 7.

The evolution of the spatial coverage of each class of triggering factor is presented in Figure 25. This indicates an increase in the Moderate and Medium classes and a reduction of about 20% for low classes when comparing 2010 and 2050.

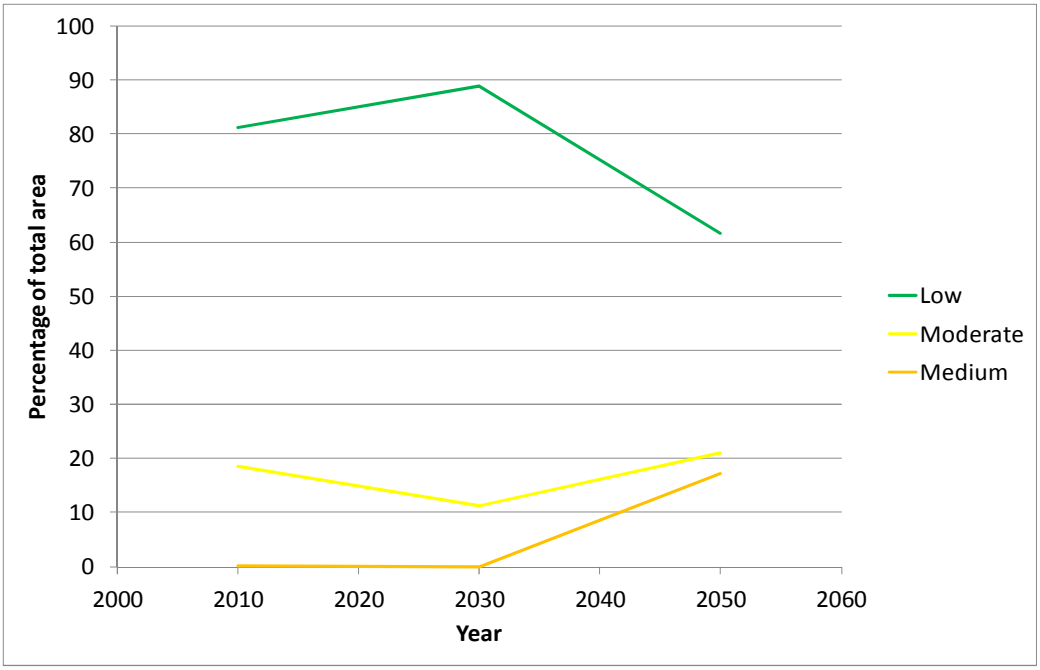

Figure 25: Evolution of classes of precipitation triggering factor Tp as a percentage of the total study area over the three scenarios at 2010, 2030 and 2050.

2. BARCELONNETTE (FRANCE)

a. Present and future data

i. Site Presentation

The studied site, the Barcelonnette Basin[2], is a 350 km² zone representative of climatic, lithological, geomorphological and land cover conditions common to several regions of South French Alps. It is crossed by the Ubaye River and delimitated by crests reaching up to 3100 m.

The Barcelonnette Basin is an asymmetric valley. The north-facing slope is characterized by allochtonous sandstone outcrops and autochtonous marls. Dominated by black marls covered by moraine deposits (2 to 20 m), its gentle slopes (10-30°) present an irregular topography with steep convex, planar and hummocky slopes. On the other side, the south-facing slope presents the steepest slopes (35-75°) with associated bar rocks on the upper part (45-75°), and with screes on the lower part (35-50°). The lower slopes associates convex and hummocky slopes (15-30°) and are covered by moraine deposits (Malet, 2003).

The landslide hazard is high in this area (Figure 26), the slopes being notably affected by severe gullying and both shallow and deep-seated large landslides (for example La Valette and Super-Sauze). Currently, many factors tend to make slopes unstable such as a dry and mountainous Mediterranean climate with strong inter-annual rainfall variability. Essentially moraine deposits and black marls are affected by rotational landslides. Other formations such as allochtonous limestones, sandstones and flyschs are principally affected by falling blocs. However, this study will not address this last type and will focus only on landslides.

[2] See webpage: http://eost.u-strasbg.fr/omiv/barcelo_area_intro.php (last visit: April 11th, 2012)

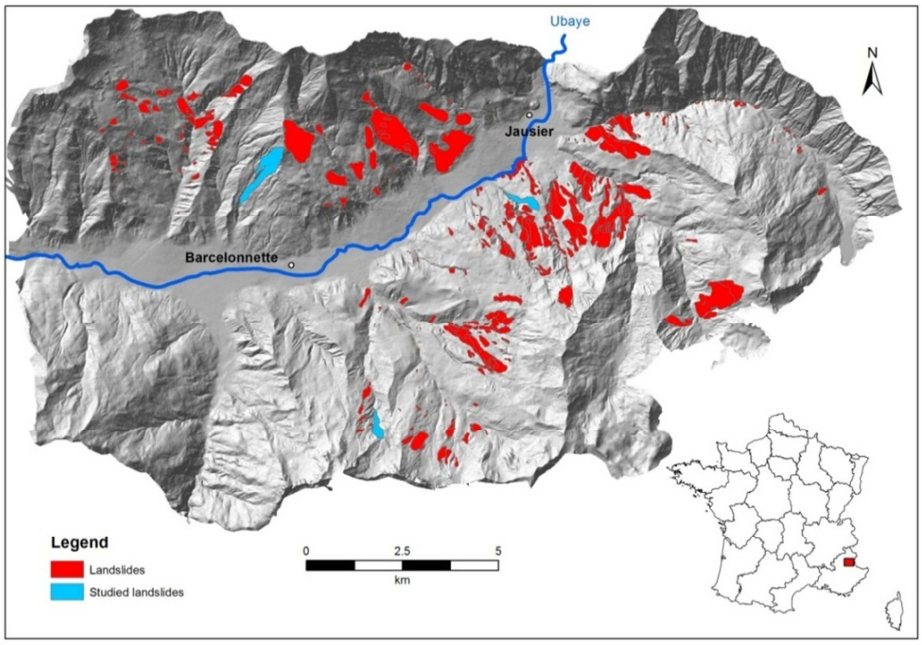

Figure 26: Study area location and landslides inventory from IPGS (2007). The blue-coloured landslides are active and monitored landslides (La Valette, Super Sauze and Poche). No inventory is shown for the South-Western part of the area.

ii. Climate data

1. Present climatic conditions

The Barcelonnette Basin has a dry and mountainous Mediterranean climate with strong interannual rainfall variability (735±412 mm over the period 1928–2005), and some high intensity storms during summer and autumn (over 40 $mm.h^{-1}$). Mean average temperature is around 7.5°, with ca. 130 freezing days per year. On the upper slopes, snowpack remains from 4 to 6 months, according to the expositions of the slopes. These strong rainstorms and the snowmelt are favourable to the triggering of mass movements (Malet et al., 2007).

However, landslides are not controlled only by climatic conditions; instability can also occur during relatively dry periods preceded or not by heavy rainfall. This reveals that land use changes can also trigger landslides.

Past climatic data used in this study were provided by CNRS and come from 2 meteorological stations, one located in Barcelonnette's village (in the valley, altitude 1155m), which provides total precipitation measures since 1928 (Figure 27) and the other one located near the Super-Sauze landslide (alt. 1740m) which records daily mean (Figure 28), minimal and maximal temperatures since 2000 and daily hours of sunshine (to estimate potential evapotranspiration) since 2004, but no data on rainfall were available for this station.

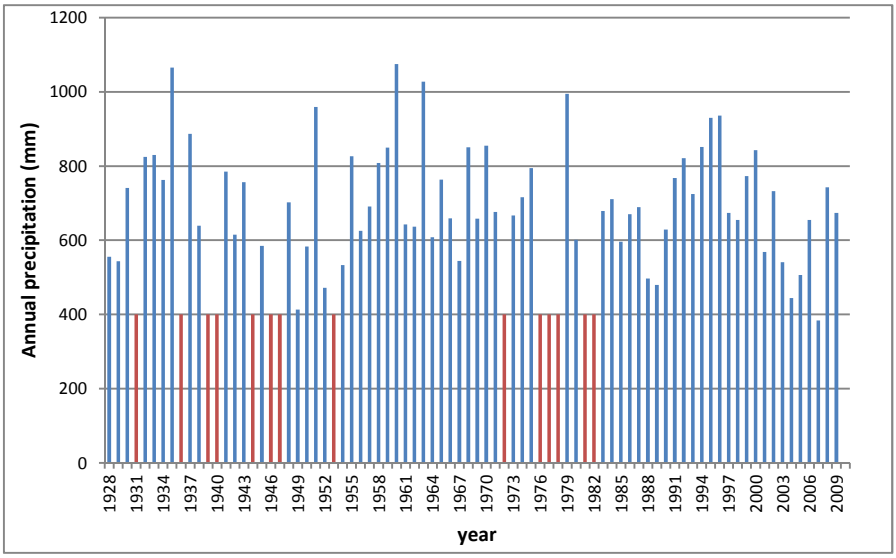

Figure 27: Annual precipitations recorded at Barcelonnette over the 1928-2009 period. (Red bars correspond to years with more than 25 days with no record)

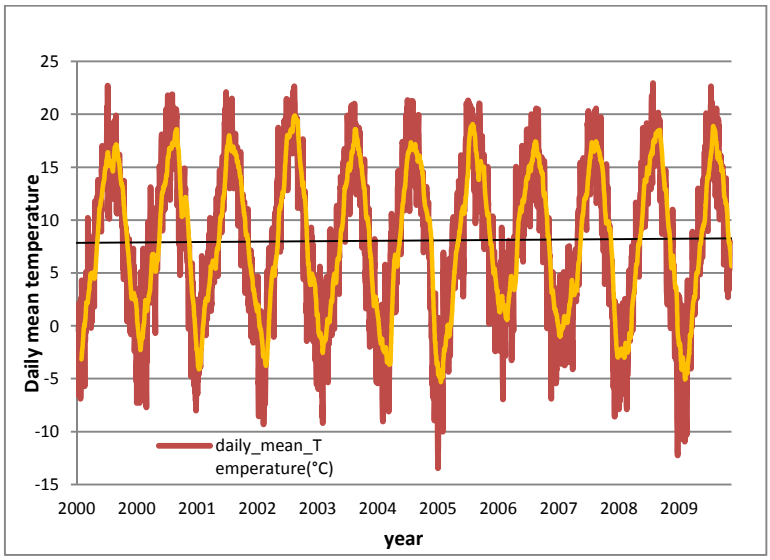

Figure 28: Daily mean temperature recorded at Super-Sauze meteorological station over the 2000-2009 period.

2. *Climate change scenario*

The regional climate model REMO (Jacob, 2001) provides basic information on possible future changes in the European climate until the end of the 21st century at a spatial scale of 25km. These simulations have been carried out under the SRES emission scenario A1B within the European ENSEMBLES project (Deliverable 3.1, Safeland 2012a). They have been used as boundary conditions of dedicated REMO simulations at a very high resolution of 10 x 10 km² for the period 1950-2050 in the area of the Alps (Deliverable 3.2, Safeland 2012b)

The second phase of the study consists in applying the non-hydrostatic COSMO Lokal Modell with a resolution of 3.8 x 3.8 km² to the results of the REMO simulations (Deliverable 3.3, Safeland 2012c).

In this way, a physically consistent simulation of small scale climatic features, e.g., local precipitation extremes and other landslide triggering events, is possible and can be linked to geomechanical models used for high resolution case studies (Deliverable 3.4, Safeland 2012d)

Finally a bias-correction model has been applied, based on differences between modelled and observed data, in order to remove the induced bias, inherent to the climate model.

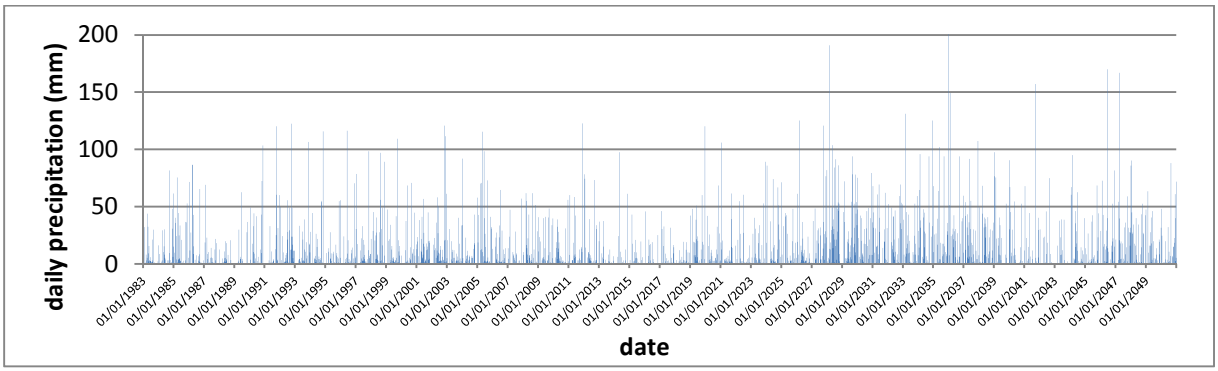

Figure 29: Time series of the daily precipitation modelled by the COSMO-LM for the 1983-2050 period

According to this model, over the 100 km by 100 km area, climate change should induce significant increases of average temperatures (up to 3°C) in both summer and winter. Regarding precipitation, the evolution is different according to the season. Winters should be wetter (up to 25 mm increase) in the future, but rainfall is likely to slightly decrease in summer.

iii. Lithological model

A simplified geological model has been derived from an engineering soil map (Thiéry 2007). The area has been divided into 6 different geotechnical zones. Each zone is represented by a column composed of 3 layers called soil units (the lower one is always considered as bedrock). Each soil unit is characterized by its thickness and some geotechnical parameters (cohesion, friction angle and dry density). Some parameters are described by probability distributions defined by expert judgment so as to take into account uncertainty and variability on the values used in the model. These parameters and their distributions are listed in Table 8.

Table 8: geotechnical parameters and their distribution law (cohesions are in kPa, frictions angle in degrees and density in kN.m-3)

	Cohesion			Friction angle			Dry density		
	min	apex	max	min	apex	max	min	apex	max
Lacustrine deposits		20			30			19	
Moraine	2	5	8	28	31.5	35	15	17.5	19
Torrential deposits		20			30			19	
Marls	16	18	20	26	31	36	16	18	20
Weathered marls	10	15	20	26	31	36	14	16.5	19

Layers' thicknesses are given through elevation maps. The top layer thickness has been evaluated through an empirical geomorphology-based approach based on Catani et al. (2010). This approach links soil thickness to slope, horizontal and vertical slope curvature, elevation, and relative position within the hillslope profile as described in Rochat et al. (under submission). It creates an index of

relative soil thickness at a regional scale, for the whole area, which can then be converted into absolute soil thickness based on some in-situ data. Hence, using punctual field data, the top layer thickness has been mapped all over the study area, varying between 1 and 7 meters (Figure 30d).

For this study area, as the hydrologic system of the area is only known on few points, simple assumptions have been made concerning the variation of the water table level. The level of ground water is assumed to fluctuate inside the top soil layer, which mostly corresponds to reworked soil. Hence, assumptions have been made that the bottom of this layer corresponds approximately to the maximum (shallowest) depth of the ground water table. This dry situation corresponds to a filing ratio of 0. Furthermore, during extreme infiltration events (extreme precipitation, intense snow melt), the ground water table could in theory reach the ground surface. The maximum water table level, simulated with a filling ratio of 1, is equal thus to the elevation model. This assumption is arguable, but it provides the potentially most adverse situation regarding landslide activities.

a)

b)

c)

d)

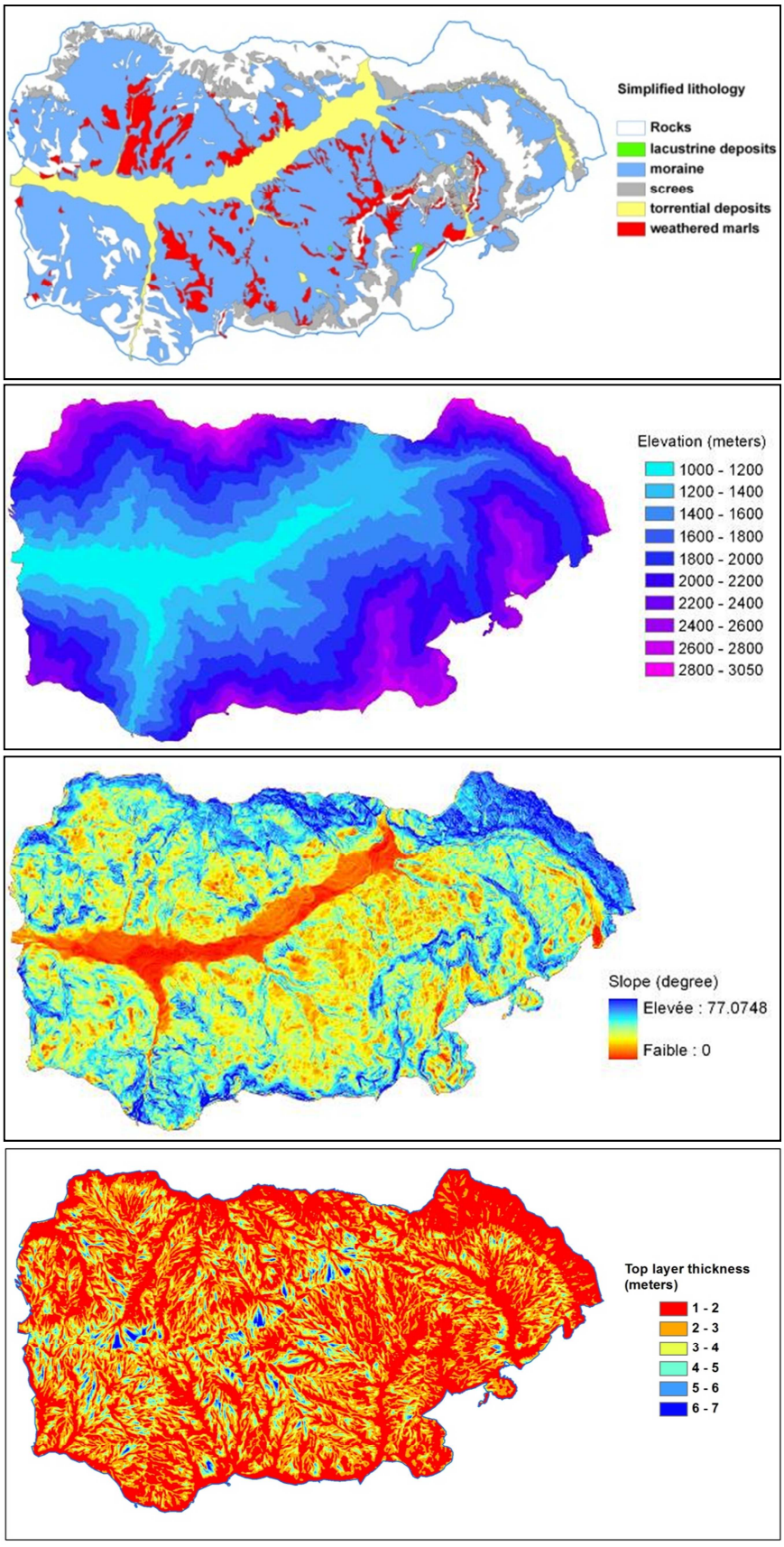

Figure 30: Main data used in the model: geotechnical zones (a), elevation model (b), slope map (c) and top layer thickness (d) (resolution: 10 m)

b. BRGM's simulation

i. Calibration phase

Landslides' length and depth are parameters defined for the whole studied area for ALICE®. Field observations have pointed out that landslides' depth varies between 1 and 10 meters and their length can reach 200 meters. The word "length" is again used to define the size of the landslide initiation zone and not the propagation length.

For the first test, 100 runs are performed for a filling ratio of 0.5. Landslides' length and maximal depth have an important influence on results (Table 9). As a matter of fact, for 80 m long landslides, an increase of the depth from 2 to 10 m implies an increase of 450 % of surface where landslides' probability occurrence is greater than 0.8 (Table 9). For 5 m deep landslides, the increase of the length from 40 to 140 m results in an increase of 20 % of surface where landslides' probability occurrence is greater than 0.8. Landslides' depth has a greater effect than landslides' length.

Table 9: Numbers of pixels where landslides' probability occurrence > 0.8, for different values of P (depth) and L (length). The water table filling ratio is 0.5.

P \ L	40 m	80 m	140 m
2 m	28420	65113	81632
5 m	131392	171076	156607
10 m	237769	360536	309866

To select the geometry (L and P) that best fits to the field data, the different computed stability maps have been compared to the landslides inventory of 2007 from IPGS (Figure 26). In so far as this inventory is not covering the complete study area, the comparison area has been reduced to be representative of the inventory. Two numbers haves been calculated:

- NG (true positive), which corresponds to the number of pixels where landslides have occurred in 2007 and where the occurrence probability simulated with Alice is greater than 0.5 ;
- NG0 (true negative), which corresponds to the number of pixels where landslides haven't occurred in 2007 and where the occurrence probability simulated with Alice is smaller than 0.5.

Hence, it is possible to evaluate NG+NG0 for all the possible landslides lengths and depths (1 m < P < 10 m and 40 m < L < 200 m). The more realistic simulations are those for which NG+NG0 is maximal. Results are represented in Figure 31.

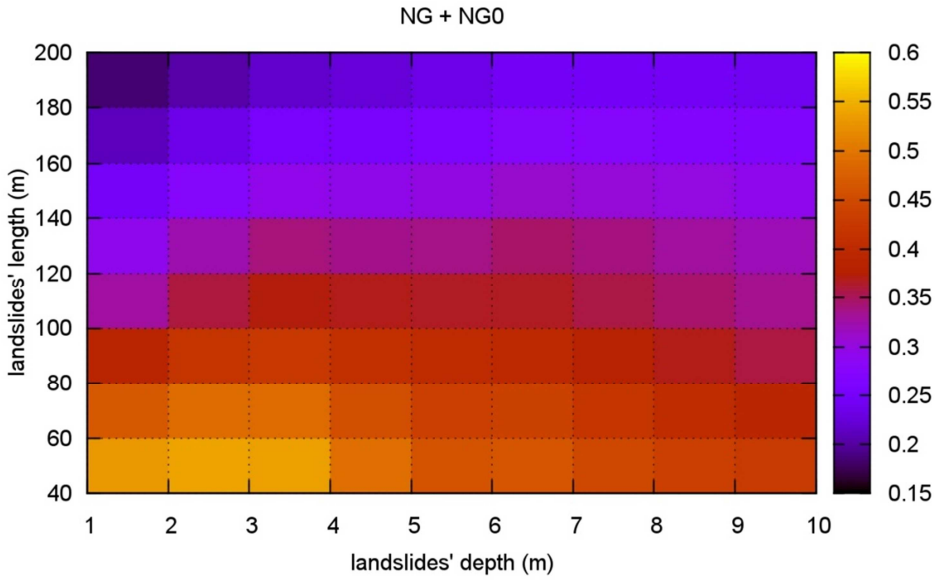

Figure 31 : Geometry analysis

The best results are obtained for landslides' depths between 2 and 4 meters and for length between 40 and 80 meters. For the next simulations P = 4 m and L = 60 m will be used.

v. First modelling scenario

Before being able to use climate change data (COSMO Lokal Modell simulations were not yet available when the study began), the methodology was tested using 3 different water table scenarios. These scenarios cover the two extreme cases: the minimum water level (filling ratio=0), corresponding to an extreme drought period and the maximal one (filling ratio=1), corresponding to a period of heavy and lasting rainfall; and an intermediate situation (filling ratio=0.5).

The whole chain was run with the 3 different filling ratios, providing 3 maps of probability of occurrence (Figure 32). These preliminary results show that, as expected, an increase of the level of the saturated zone (e.g. in our case due to a long period of rainfall and or snow melt events) induces a reduction in the probability of occurrence, and a decrease in the water level makes the slopes more stable. These changes are not uniform over the area. Effects of water-table changes are more pronounced on profiles with steepest slopes.

These preliminary results reproduce quite well the field observations: big landslide areas such as La Valette, Super Sauze and Poche are pointed out by the simulations with concentrated zones of pixels with high occurrence probabilities (often greater than 0.8). The higher the filling ratio, the more the high-occurrence probability zones are extended.

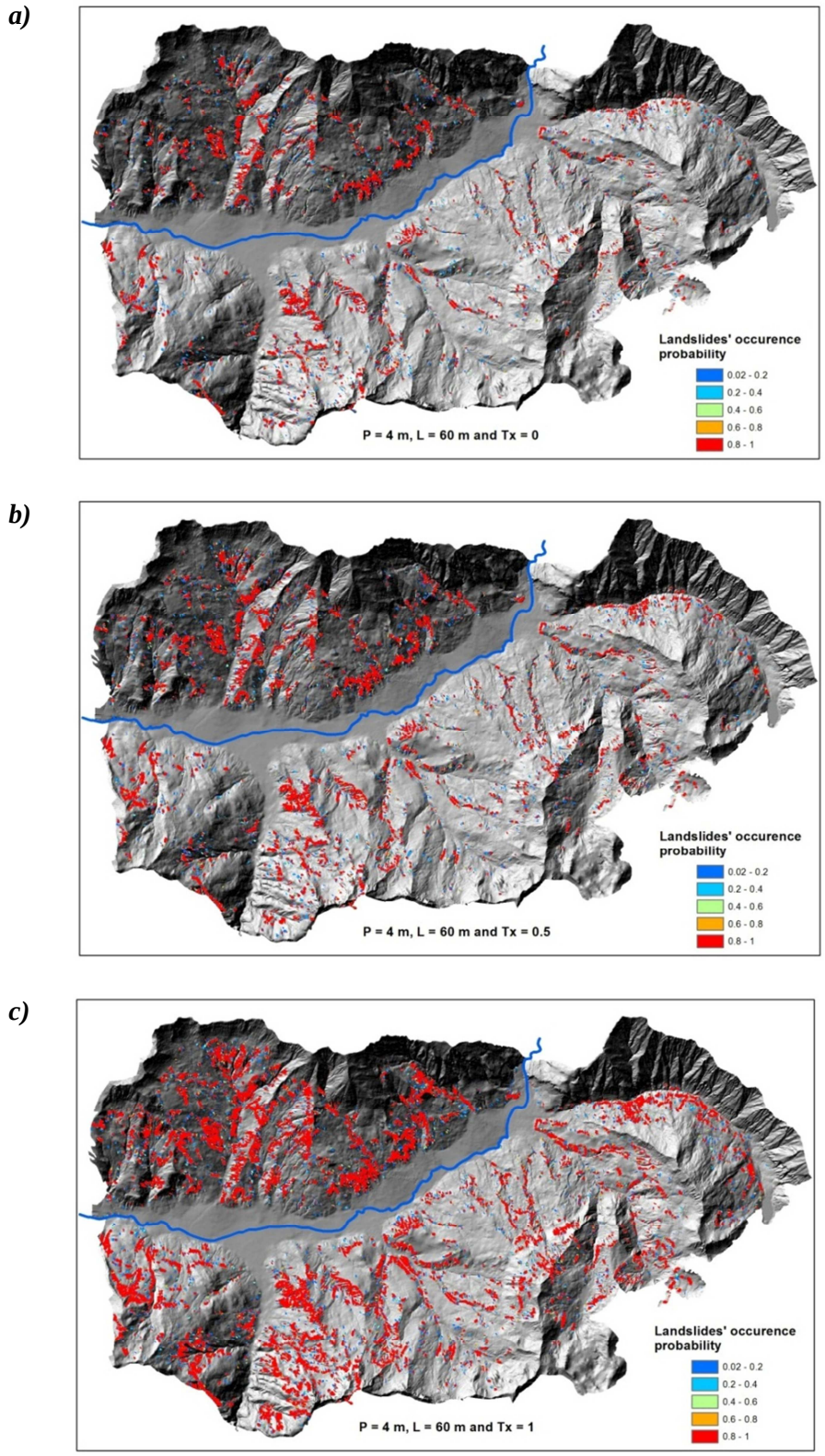

Figure 32: Representation of the probability of occurrence resulting from the simulations using the 3 different filling ratios. The ratio is 0 (a), 0.5 (b) and 1 (c). P: maximal depth of the landslides, L: length of the landslide and TX: Filling ration

However, in reality, in this area, a situation where the water table is at its lowest level should not trigger landslide with a 100% probability. One can conclude that this model is thus very conservative. This can be explained by conservative assumptions on, among other geotechnical data and to approximation of thickness propagated on the whole area. This model is nevertheless useful to make a baseline situation, in order to show the validity of the proposed methodology, but also to evaluate the relative tendencies of the effects of global climate change on landslide's activities

In order to improve the accuracy of the results, eleven maps have been computed instead of the previous three, covering the range of filing ratios from 0 to 1, corresponding to 11 classes of water table levels (Table 10). Maps are computed using the central values as filling ratio, except for the 2 extremes (in these case, 0 and 1 are taken). Hence, for a given day, according to the previous meteorological conditions (either obtained from observed data or modelled by climate model), Gardenia computes a global filing ratio, which falls into one of these classes, each class corresponding to a specific susceptibility map.

Table 10: Classes of levels of water table according to the filling ratio

Classes of water levels	Interval for the filling ratio	Filing ratio used to compute the stability map
WL_0	[0.00 ; 0.05 [	0
WL_1	[0.05 ; 0.15 [	0.1
WL_2	[0.15 ; 0.25 [	0.2
WL_3	[0.25 ; 0.35 [	0.3
WL_4	[0.35 ; 0.45 [	0.4
WL_5	[0.45 ; 0.55 [	0.5
WL_6	[0.55 ; 0.65 [	0.6
WL_7	[0.65 ; 0.75 [	0.7
WL_8	[0.75 ; 0.85 [	0.8
WL_9	[0.85 ; 0.95 [	0.9
WL_{10}	[0.95 ; 1.00]	1

vi. Hydrological Modelling

1. Calibrations

In order to calibrate the hydrological model, records of water table are required. The only piezometric data available over a long-enough period of time are the ones recorded on the Super Sauze's landslide (Figure 33). However, as GARDENIA is a global model, it should be as representative as possible of the average hydrological behaviour of the whole area. Among the possible piezometers, the EV2, located at the foot of the landslide is the best candidate. In this location, soil is indeed less remoulded and thus presents some hydrological characteristics close to the autochthonous marls or moraine deposits.

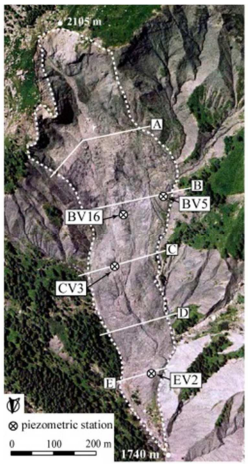

Piezometric stations	depth	Recording period
BV5	3.2m	2002-2008
BV16	2.5m	1999-2008
CV3	2.5m	2002-2008
EV2	3.0m	2002-2008

Figure 33: Piezometric stations located on the Super-Sauze mudflow (data retrieved from OMIV website3)

The calibration of the hydrological model has been performed between 2004 and 2008, period during which all the required observed data (mean temperature, total precipitation, potential evapotranspiration and water table) coexist. The results of this calibration are shown in Figure 34. In order to compensate the differences of temperature between the weather station and at the piezometer due to the temperature gradient between the different elevations, a bias correction has been applied (increase by a constant equal to 4°C).

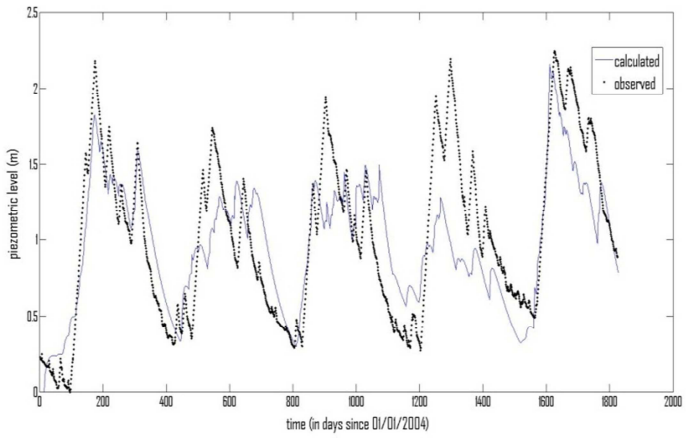

Name	Value
RUMax	0 mm
RUIPER	0.16674 mm
THG	174 days
TG1	66.1 days
N0	260.465 (mm)
a	0.8 ($mm.°C^{-1}.day^{-1}$)
Tc1	0.19 °C
Tc2	1 °C
Tc	0.7 °C

Figure 34: Calibration of the hydrological global model based on observed water table between 2004 and 2008. (parameters are described in section 1.a.ii)

[3] http://eost.u-strasbg.fr/omiv (last visit 03/06/2012)

2. Predictions

Gardenia's parameters being calibrated, climatological data provided by CMCC have been used to compute time series of water level. In order to assess the evolution of patterns of climate driven landslide hazard, we choose to work on two different 31-year periods: the first one from 1983 to 2013, for the current period and the second one from 2020 to 2050 for the prediction of future climate (Figure 35).

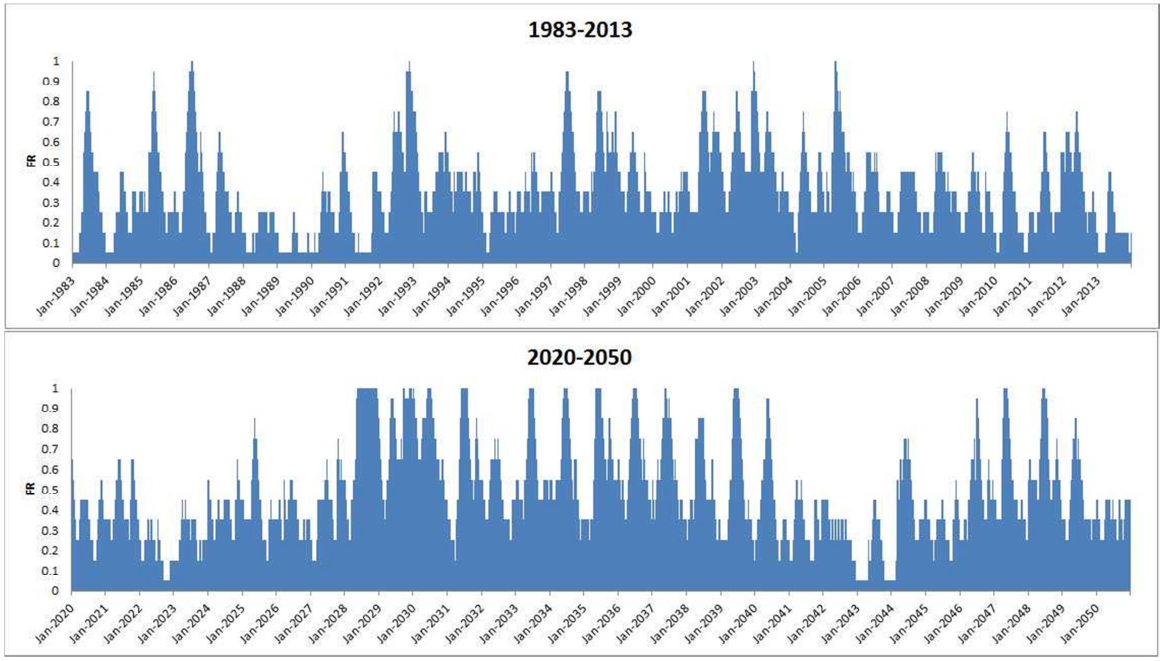

Figure 35: Time series of filling ratio for the current period (up) and the future period (down) computed based on data from COSMO-REMO model

These computed water levels have been converted into time series of filling ratios according to (2). Frequency histograms of filling ratio classes have then been established for the two periods (Figure 35). This representation shows that the highest "water table levels" would occur more often than now.

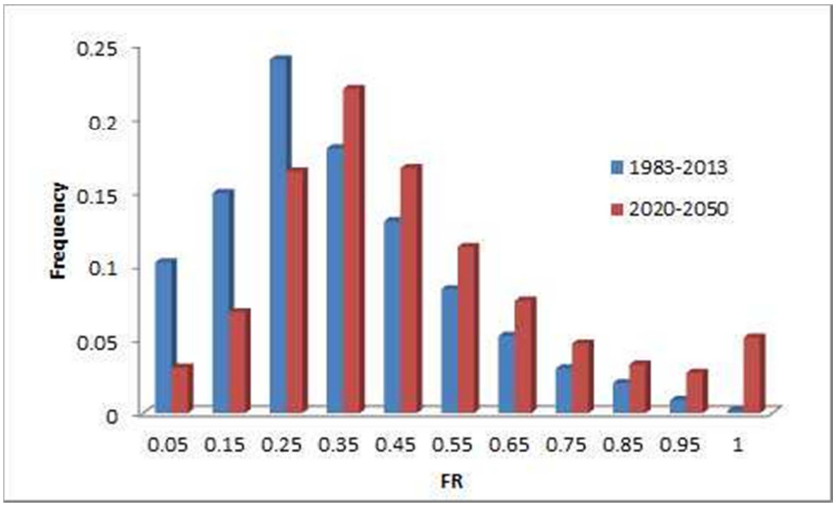

Figure 36: Distributions of the filling ratios for the current and future periods computed based on the COSMO-REMO data

Global susceptibility maps have then been computed considering a weighted mean, as described in Equation (8)

- for the present and future 30-year periods based on COSMO-REMO climatic data (Figure 38)
- for the actual landslide conditions based on observed data (Figure 37)

$$Susc(i) = \sum_{FR=1}^{11} Freq(FR) * Susc(i, FR) \quad \textbf{(8)}$$

With Susc(i) : landslide occurrence probability at pixel i
Freq(FR): Frequency of filling ratio class (FR)
Susc(i,FR): landslide occurrence probability at pixel i, given a filling ratio FR

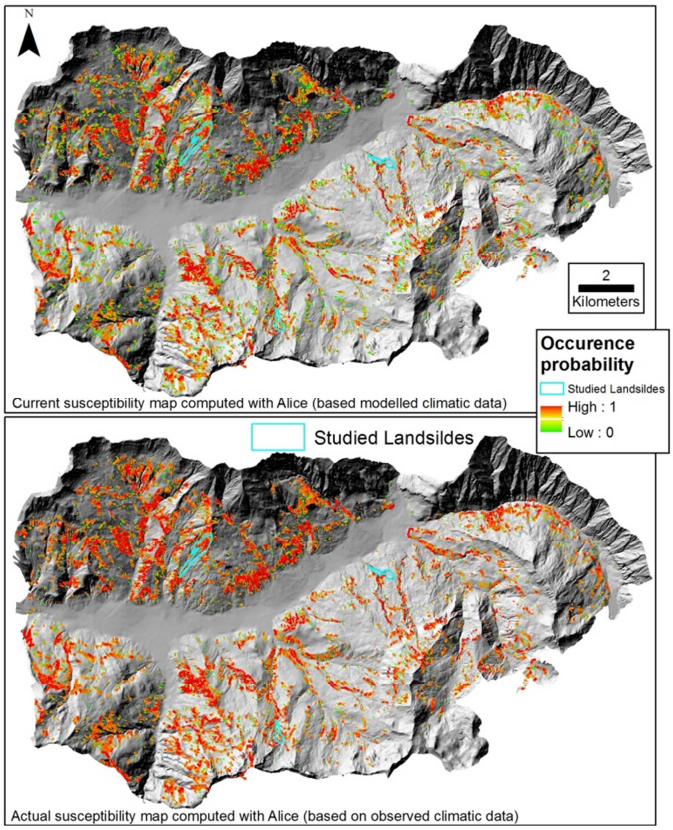

Figure 37: Comparison of the susceptibility maps computed for the current period, based on (up) data provided by the COSMO-REMO model for the 1983-2013 period, (down) observed data for the 2004-2009 period. Area with 0 probability of instability are not colored.

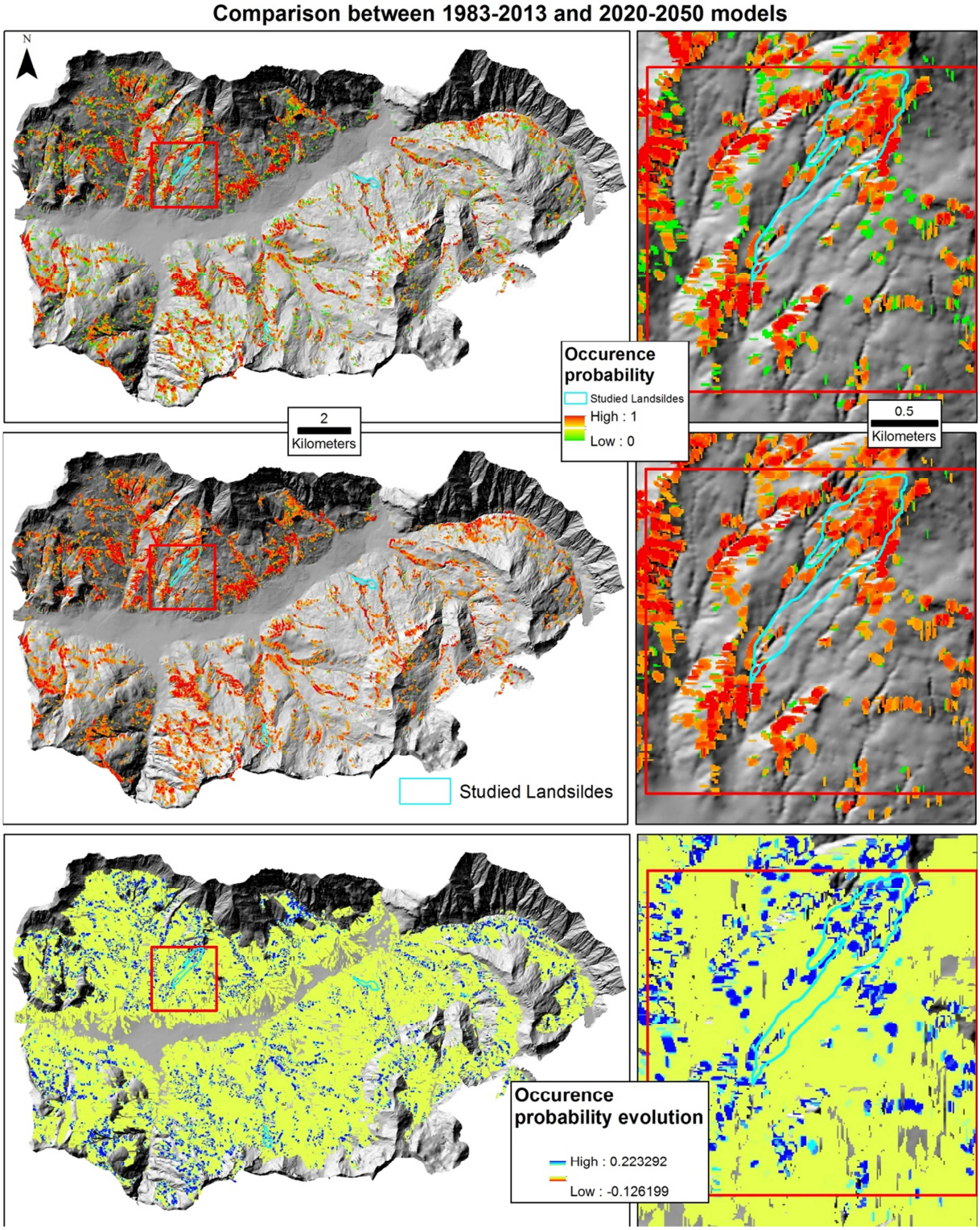

Figure 38: Susceptibility maps for, above, the current (1983-2013) and, below, the future (2020-2050) periods computed with ALICE based on COSMO-REMO climatic data

The comparison of these 3 maps points out that:

- The map for the current period is close to the actual susceptibility map, whereas climatic data are just a scenario which does not aim at representing real past events, but just a climatic

context. This similarity confirms that climatic data could be used as a pattern to evaluate trends in landslide activities over a long period of time, but not for a day-to-day comparison. Hence, the impact of climate change on landslide susceptibility can be estimated comparing the maps generated using the climate model data.

- As expected in view of the evolution trend in the distribution of the water table level, the occurrence probability of instability would be either equal or higher in the future than today (Figure 39). The SRES A1B scenario is very likely to induce an increase in landslide activity.

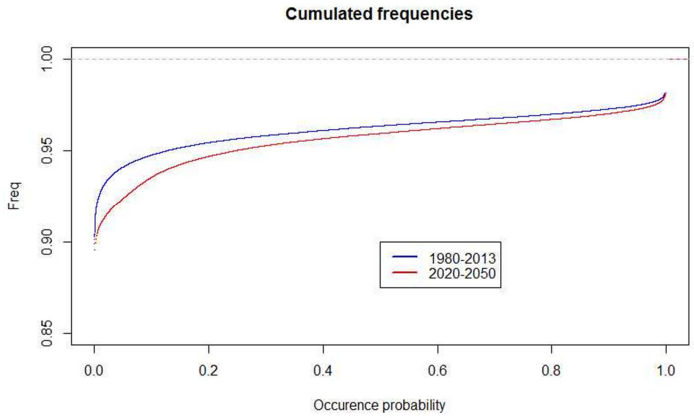

Figure 39: Cumulated proportion of pixels with given occurrence probability of occurrence

c. Conclusion and perspectives

Dealing with risks requires an evaluation of what the future could be. Thus, changes in triggering factors have to be taken into account in hazard assessment, not only qualitatively, but also quantitatively. In order to cope with this issue, a method was proposed here.

A hydrological model (GARDENIA®) is combined with a quantitative landslide assessment model (ALICE®) to allow the integration of climatic scenarios into landslide susceptibility mapping.

3. PIZZO D'ALVANO (ITALY)

a. Description of the study area and CC data (UNISA)

The study area is located in Southern Italy (Figure 40) within a context of about 400 km^2 where steep carbonate bedrock massifs are covered by shallow deposits of unsaturated pyroclastic soils (Cascini et al., 2009). In this area, the Pizzo d'Alvano massif (Figure 40) represents one of the mostly affected area by shallow landslides, with a huge catastrophe occurred on May 1998 (Cascini et al., 2011). During this event, rainfall triggered about one hundred of shallow landslides and tens of flow-type landslides which can be classified as flowslides, debris flows and debris avalanches according to the landslides classification proposed by Hungr et al. (2001). It is worth noting that the occurred landslides were triggered by different rainfall-induced triggering mechanisms (Cascini et al., 2008) which can be investigated over large area with different levels of uncertainties, as discussed by Sorbino et al. (2009).

As for the in-situ conditions, Pizzo d'Alvano massif is characterized by steep hill-slopes with a high energy relief, being the uppermost areas located at about 1'000 m a.s.l. and piedmont zones at about

50-200 m a.s.l.. Slope angles range from 30° to 40° along the hill-slopes where pyroclastic soil covers have thickness ranging from 1 to 3 meters. Pyroclastic soils are characterized by unsaturated conditions with suction values ranging from about 60kPa in summer up to 2-5kPa in winter (Cascini & Sorbino, 2002).

The main geotechnical features of pyroclastic soils (Bilotta et al., 2005) consists in: negligible soil cohesion values, soil friction angles comparable to slope angles, high porosity values, and collapsible behavior of the soils upon wetting. These peculiar mechanical features highly predispose the occurrence of rainfall-induced landslides of the flow-type.

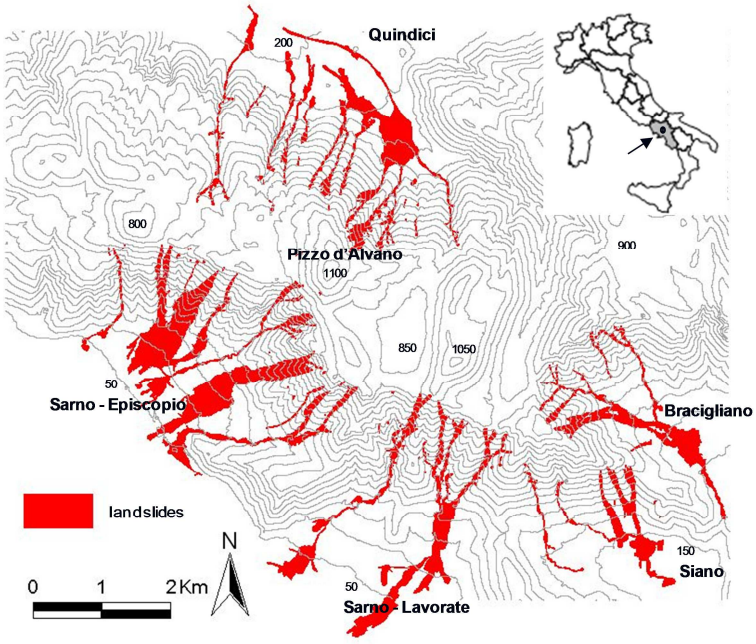

Figure 40: Overview of the Pizzo d'Alvano test area (Southern Italy) with the indication of the landslides occurred on May 1998.

Within the test area, three mountain basins have been selected (namely B3, B14 and B35) which are characterized by typical massif's site conditions and large soil volumes prone to landsliding. The field data for these basins are provided in the following Figure 41, Figure 42 and Figure 43. Particularly, a high quality 3m x 3m Digital Elevation Data (DEM) has been referred which is showed in Figure 41; based on this DEM, the slope angle map has been computed (Figure 42); for the uppermost parts of the hill slopes, a detailed cover thickness map is available which has been drawn after the 1998 landslides, thus outlining the total amount of soil volumes which can be mobilized by potential future landslides (Figure 43); finally, a geomorphological map is also available which outlines the areas susceptible to landslides (Figure 44).

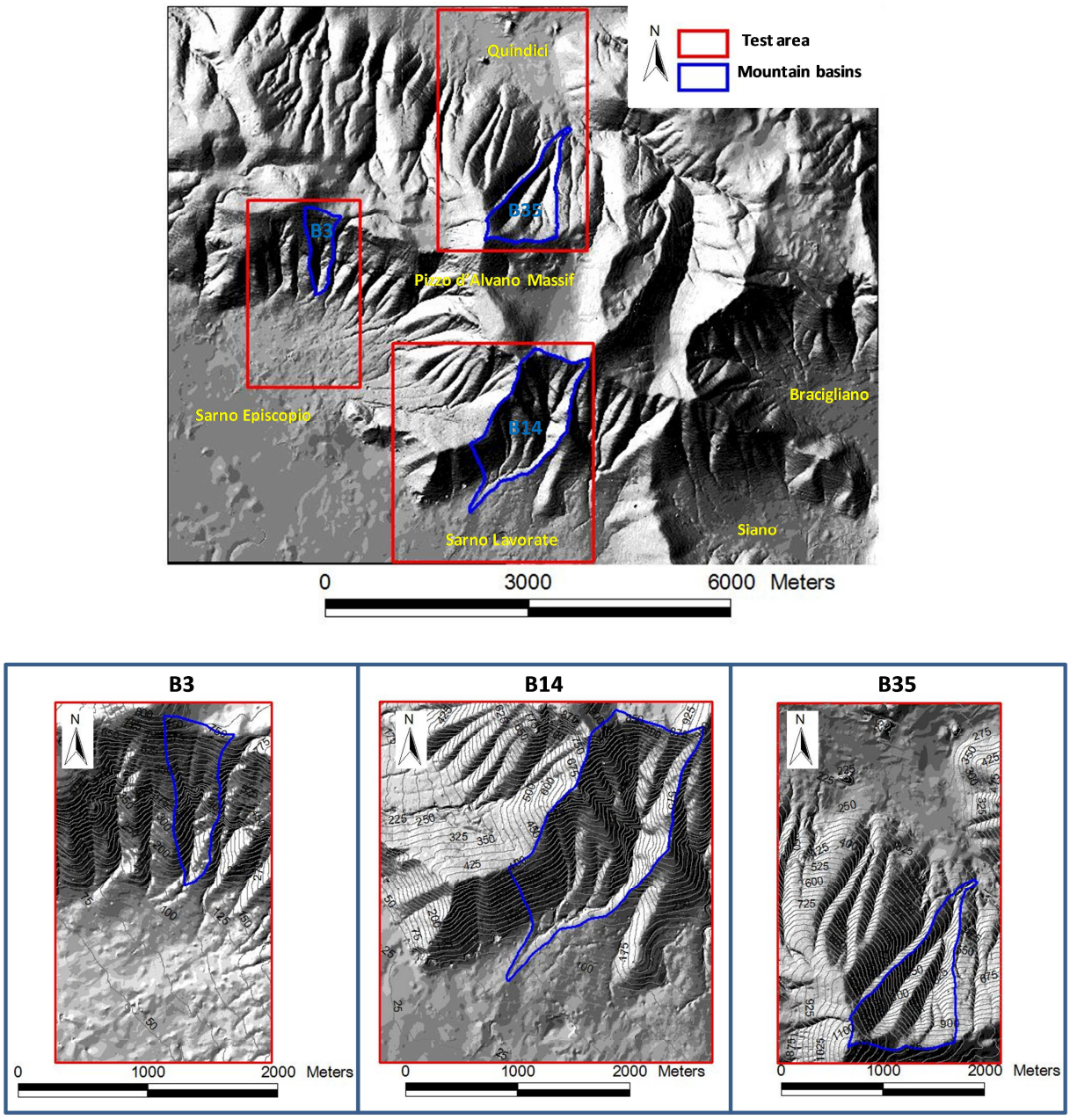

Figure 41: Digital Elevation Model (3m x 3m) used for the selected basins (data from Cascini et al., 2006).

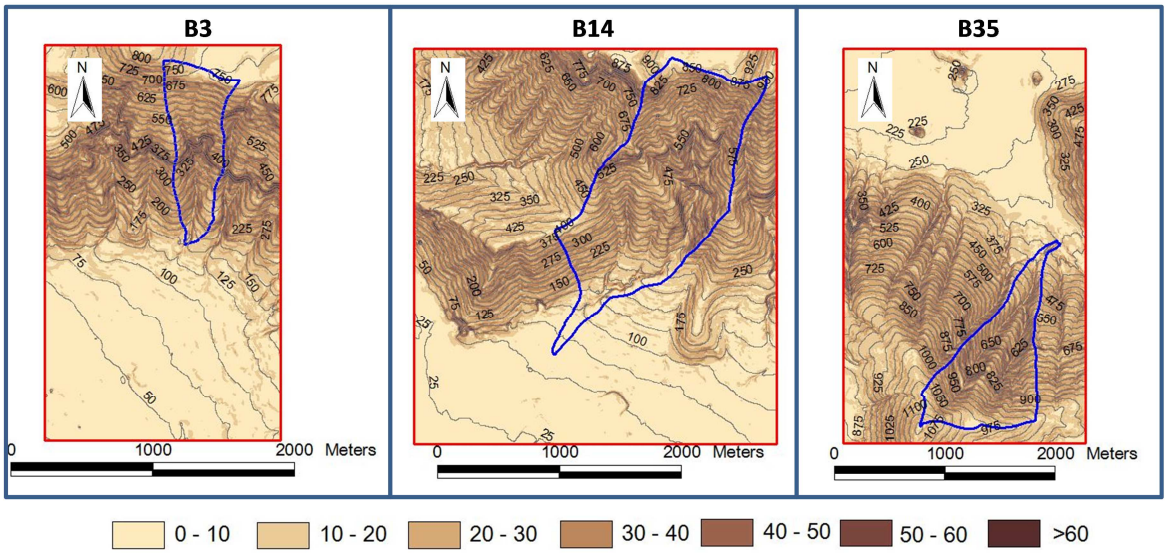

Figure 42: Slope angle map obtained from the DEM of Figure 41.

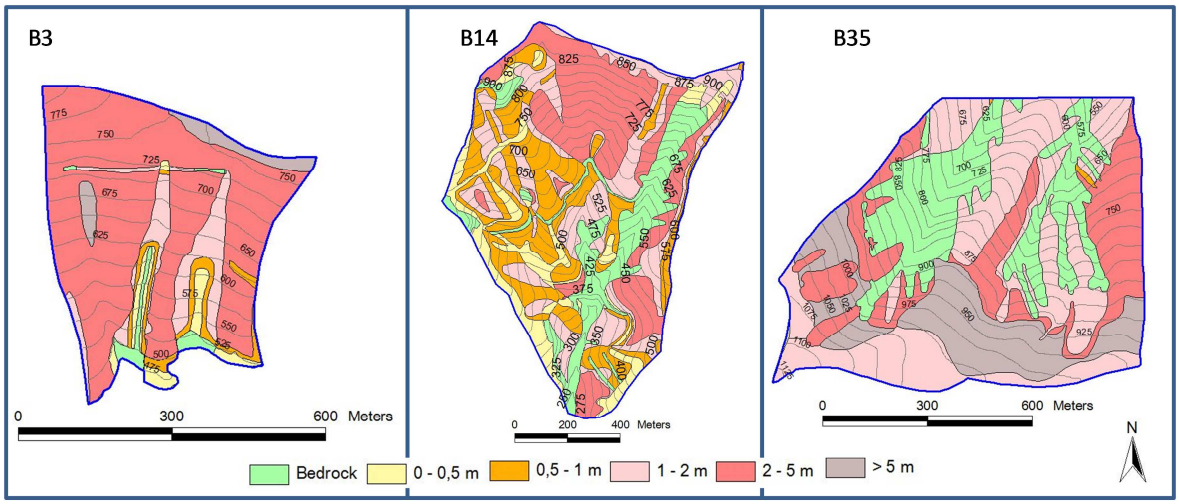

Figure 43: Thickness map of the pyroclastic covers for the selected basins (data from Cascini et al., 2006).

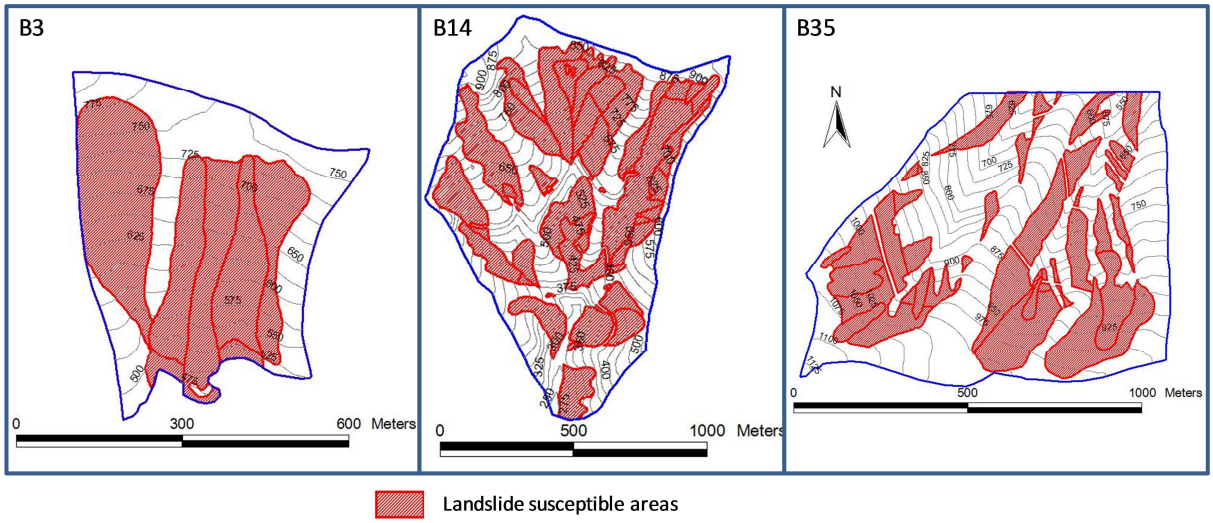

Figure 44: Areas susceptible to landslides for the selected basins (data from Cascini et al., 2006).

Figure 45 shows the rainfall data provided by CMCC (EuroMediterranean Centre for Climate Changes) which were obtained based on an extensive rainfall data-set coming from measurements at 5 rain-gauges located at different altitudes around the Pizzo d'Alvano massif; particularly, the CMCC rainfall data (labeled as COSMO CLM in Figure 45) take into account the Climate Change effects and they are provided in terms of intensity-duration values for return periods equal to 10, 50 and 100 years. Figure 45 shows that CMCC data correspond to higher rainfall intensities than available measurements; this is the case for each considered return period and all the investigated rainfall durations; particularly, the CMCC rainfall intensities exceed the available measurements with increments ranging from 82% (T=10 years) to 95% (T=100 years).

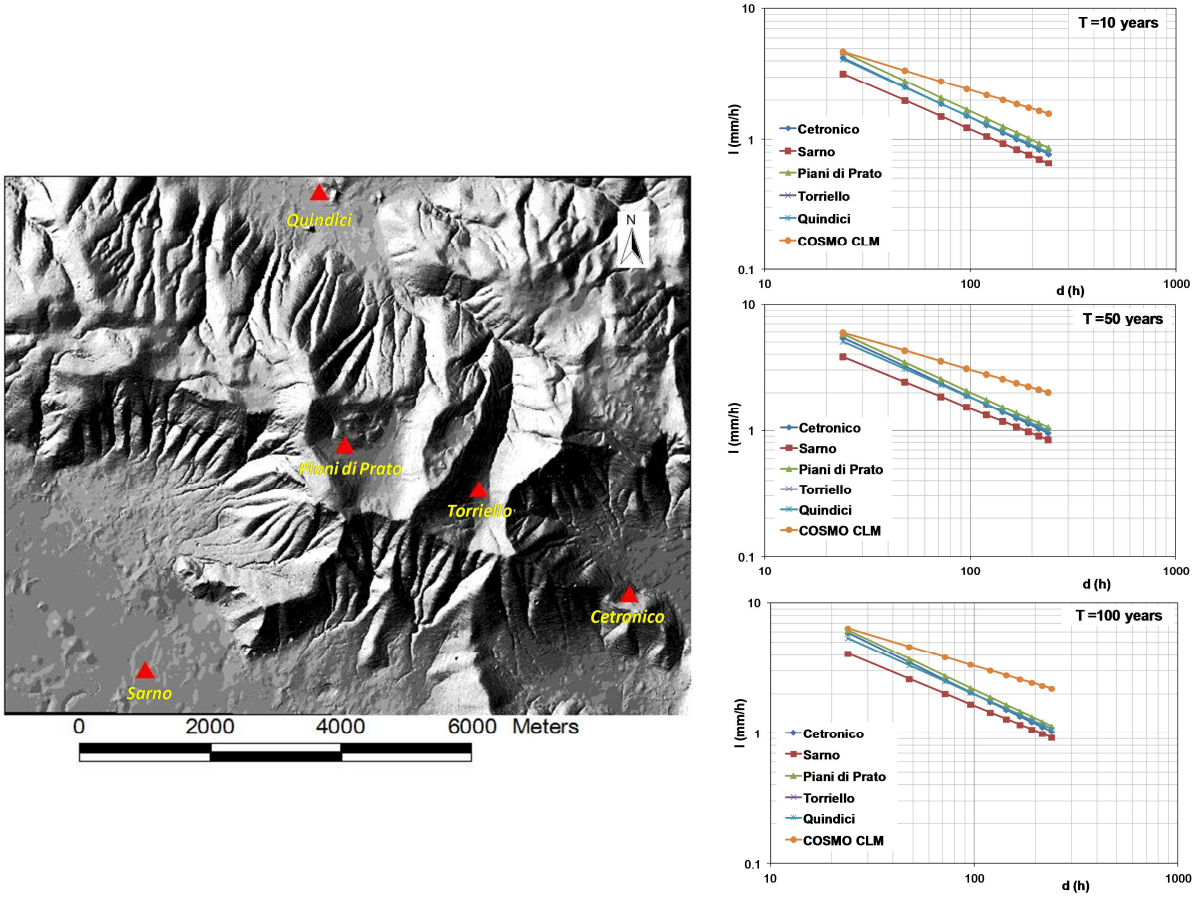

Figure 45: Rainfall data including the Climate Change effects for the Pizzo d'Alvano area (data from CMCC).

b. Methods applied (UNISA)

The performed analyses were aimed to assess the source and propagation areas of potential landslides induced by different rainfall intensity-duration scenarios.

In details, the considered return periods were equal to 10 and 50 years; rainfall intensity was assumed not higher than saturated soil conductivity; rainfall duration was computed from the formulation of Pradel & Raad (1993) who relate rainfall duration to the wetting front velocity in an unsaturated soil. Based on these hypotheses, the scenarios of Figure 46 were considered for the selected mountain basins (Figure 47).

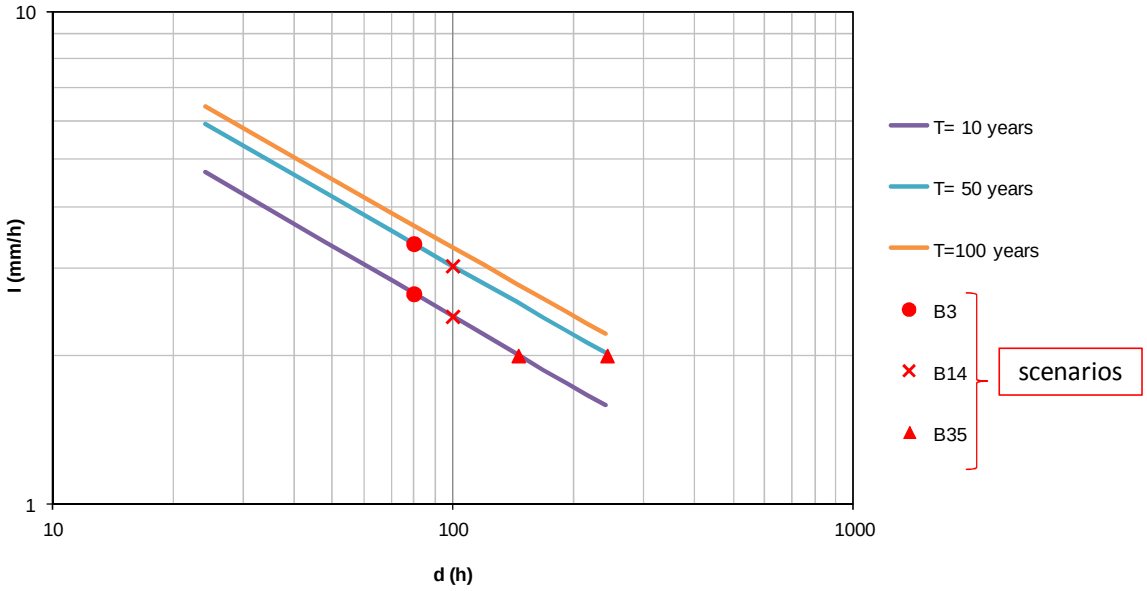

Figure 46: Intensity-duration rainfall scenarios considered for the selected basins (data from CMCC - EuroMediterranean Centre for Climate Changes).

For the landslide source areas, the TRIGRS model (Savage et al., 2004; Godt et al., 2008) was used to simulate the transient groundwater flow induced by rainfall in the pyroclastic soils in saturated-unsaturated conditions. Hourly rainfall intensities of Figure 46 were assumed as boundary condition at the ground surface and evapotranspiration was disregarded since its effects are negligible for 1-7 days rainfall (Sorbino, 2005). As far as the initial condition, for each sector, different initial water table depths were considered which provide a mean suction value of 5 – 10 kPa in the pyroclastic covers, in agreement with the suction measurements (Cascini and Sorbino, 2002). As for the soil mechanical properties, Table 11 shows both hydraulic properties and shear strength parameters which were taken from Sorbino et al. (2010).

Table 11: Physical and mechanical properties of pyroclastic soils (from Sorbino et al., 2010).

	γ_{tot} (kN/m^3)	c' (kPa)	φ' (°)	k_{sat} (m/s)	D (m^2/s)	θ_{sat}	θ_r	α (m^{-1})
Sarno	15	5	38	1.8×10^{-5}	5.9×10^{-5}	0.66	0.20	6.3
Quindici	15	5	38	6.0×10^{-6}	4.5×10^{-5}	0.53	0.25	8

γ_{tot}: soil unit weigth, c':effective cohesion, φ':friction angle, k_{sat}: hydraulic conductivity, D :diffusivity, θ_{sat}: saturated water content, θ_r: residual water content, α: Gardner curve parameter

The landslide propagation areas were computed through the Flo-2D model (O 'Brien, 1993) considering as mobilized volumes those obtained from the TRIGRS model. Particularly, triangular discharge-time functions were assumed with the peak at 1/3 of total duration; the input peak discharge was computed from the mobilized volume as proposed by Rickermann (1999). For the propagating masses the solid concentration was assumed equal to 35 % and a quadratic rheological law was considered with rheological parameters taken from Pirulli and Sorbino (2007, 2008) and Cascini et al. (2011), hereafter summarized in Table 12.

Table 12: Rheological parameters assumed for propagation analyses.

	$\tau_{y,\,min}$ [kPa]	η [Pa·s]	K_{lam} [-]	n_{st} [-]	C_v [-]
Case 1	1.0	2.0	2500	0.08	0.35
Case 2	2.0				

τ_y: yield strength, η:dynamic viscosity, K_{lam}: resistance parameter for laminar flow, n_{st} : flow resistance of the turbulent and dispersive shear stress, C_v : sediment concentration by volume

c. Results and discussion

Figure 47 provides the simulated landslide source areas for the selected mountain basins for return periods equal to 10 and 50 years.

It can be noted that depending on the massif sector (Sarno for B3 and B14 while Quindici for B35) failure scenarios are characterized by a different severity and mobilized volumes range from about 9'000 m^3 for B3 to 20'000 m^3 for B35.

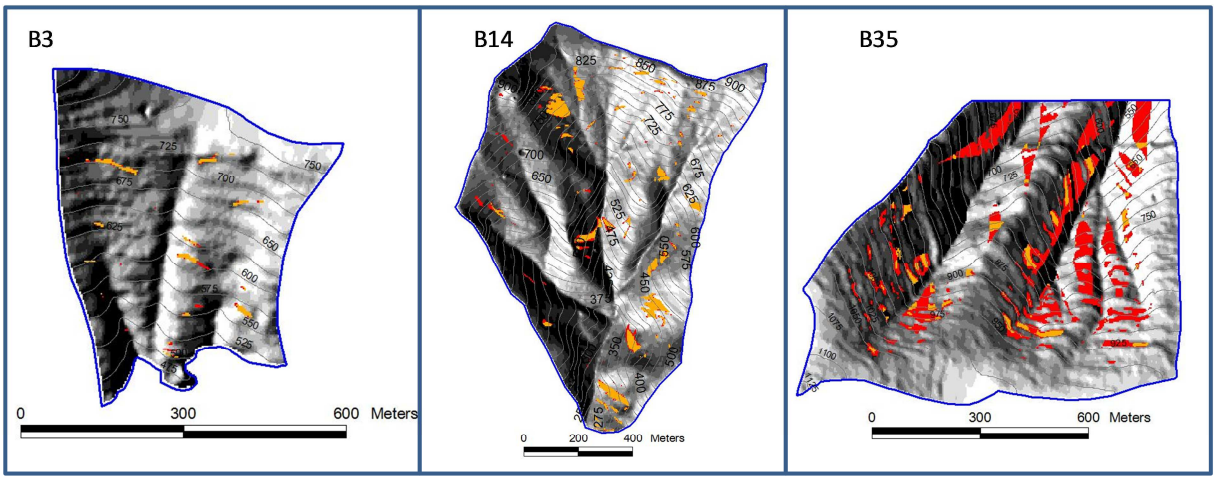

T (years)	B3	B14	B35
	Volume (m^3)		
10	6880.5	100984.5	42403.5
50	8626.5	122400	199692

Figure 47: Simulated landslide source areas for the selected basins.

Figure 48, Figure 49 and Figure 50 show the simulated landslide propagation areas and the simulated flow depths which are mostly comprised in the range 1-3 m, with greater values attained only in some upper/central parts of the channels or at the piedmont areas for the most severe scenarios. These scenarios must be compared to events with similar return periods and some considerations can arise from a comparison between the achieved results and the results coming from the historical analysis (Cascini & Ferlisi, 2003) of the occurred events on Pizzo d'Alvano massif from 1640 to date. Particularly, historical analysis shows that for a return period ranging from 10 to 50 years, all the occurred phenomena involved two mountain basins as a maximum. The performed analysis using CMCC data clearly shows that the number of the involved mountain basins can be higher and this can be related to the effect of the increased intensities of rainfall events due to climate change.

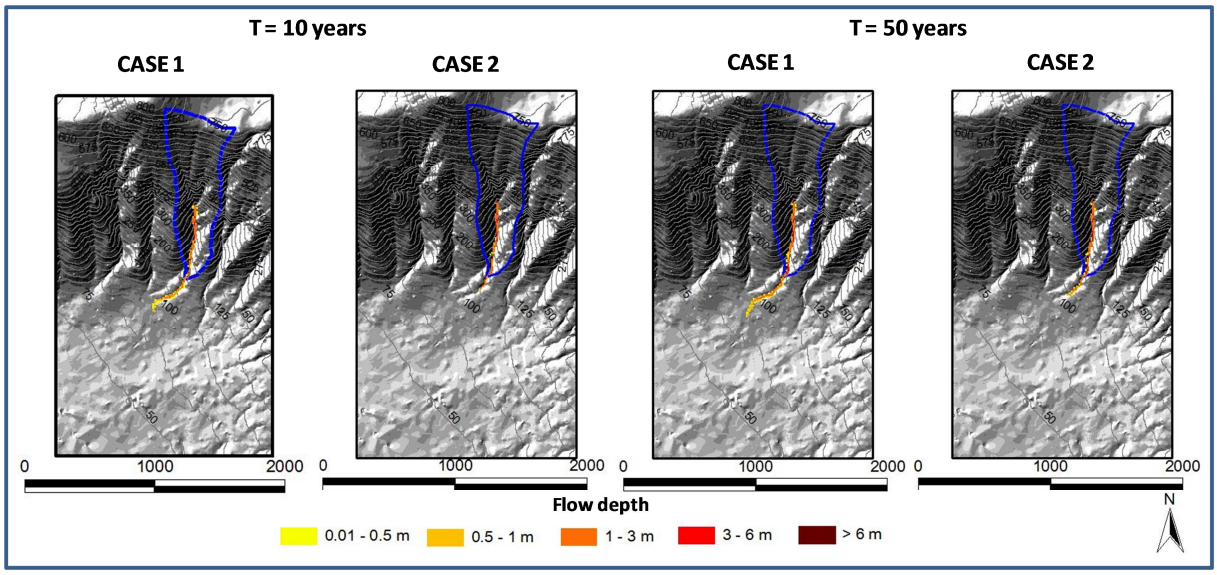

Figure 48: Simulated landslide propagation areas for the B3 mountain basin.

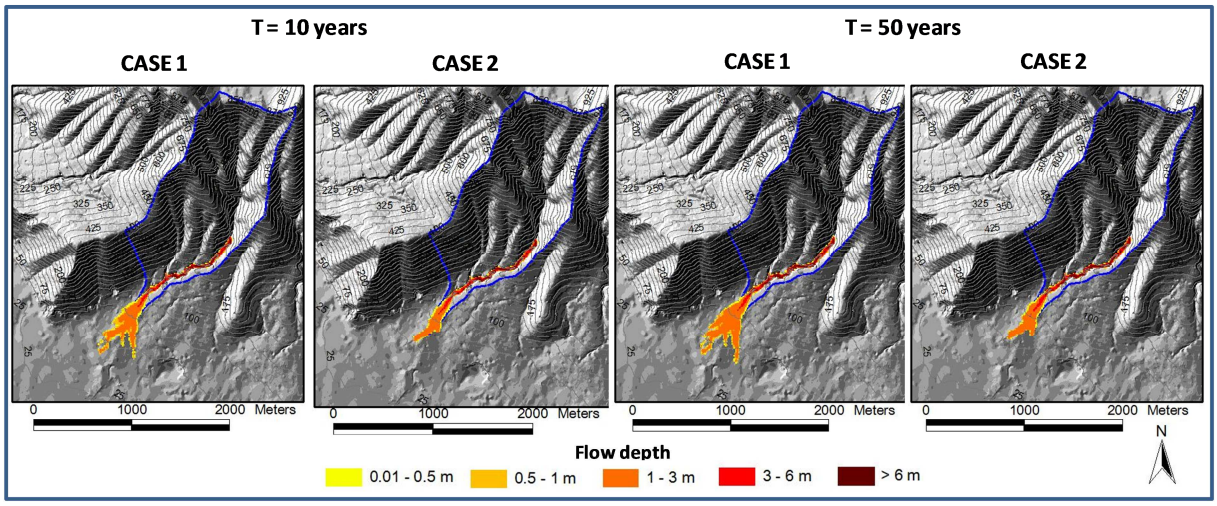

Figure 49: Simulated landslide propagation areas for the B14 mountain basin.

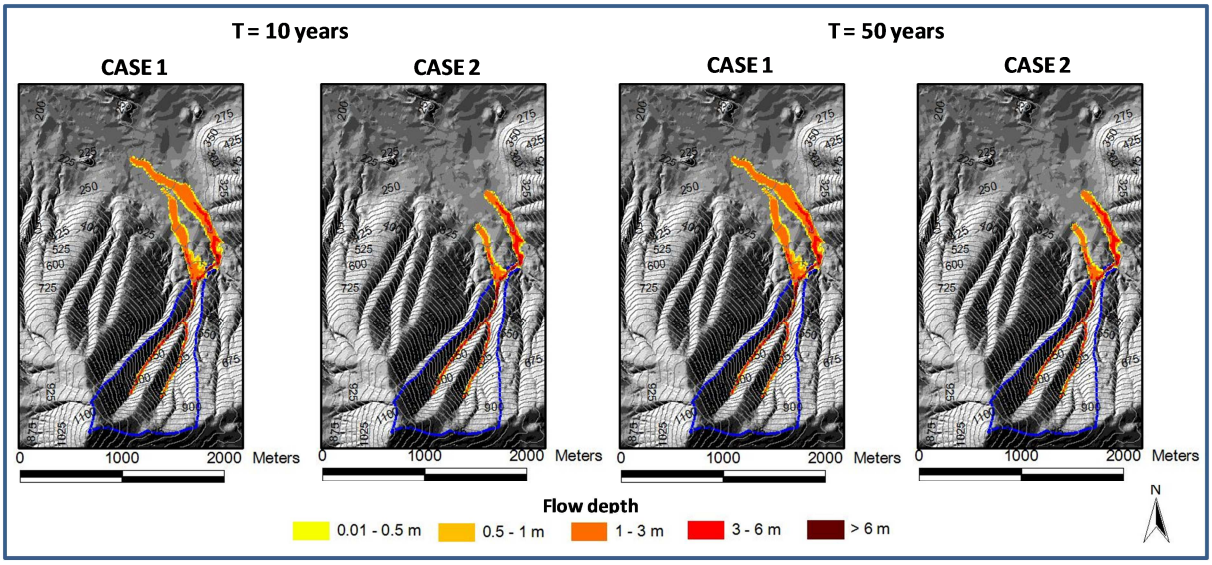

Figure 50: Simulated landslide propagation areas for the B35 mountain basin.

4. SPAIN

a. Description of the study area:

The study area is located in the Central Pyrenees (Figure 51) and is characterized by a high mountain relief with elevations between about 1000 and almost 3000 m asl. From a geological point of view, the study area is situated in the Axial Pyrenees. The basement consists almost entirely of igneous and metamorphic Paleozoic rocks formed and tectonised during the Hercinian orogeny and deformed again during the Alpine orogeny (Muñoz, 1992). The bedrock is covered by colluvium and tills. Colluvial deposits reach a thickness of a few meters in some low order catchments, and glacial deposits can locally present a thickness of several tens of meters.

The climate in the study area is influenced by three factors: the vicinity of the Mediterranean Sea, the west winds from the North Atlantic and the orographic effects of the Pyrenean mountain range (Novoa, 1984; Cuadrat and Pita, 1997). There are two typical rainfall patterns that trigger debris flows in the region (Hürlimann et al., 2003): i) short duration, high intensity rainfalls related to convective summer storms, and ii) moderate intensity rainfall during autumn/winter lasting for several days or weeks and affecting large areas.

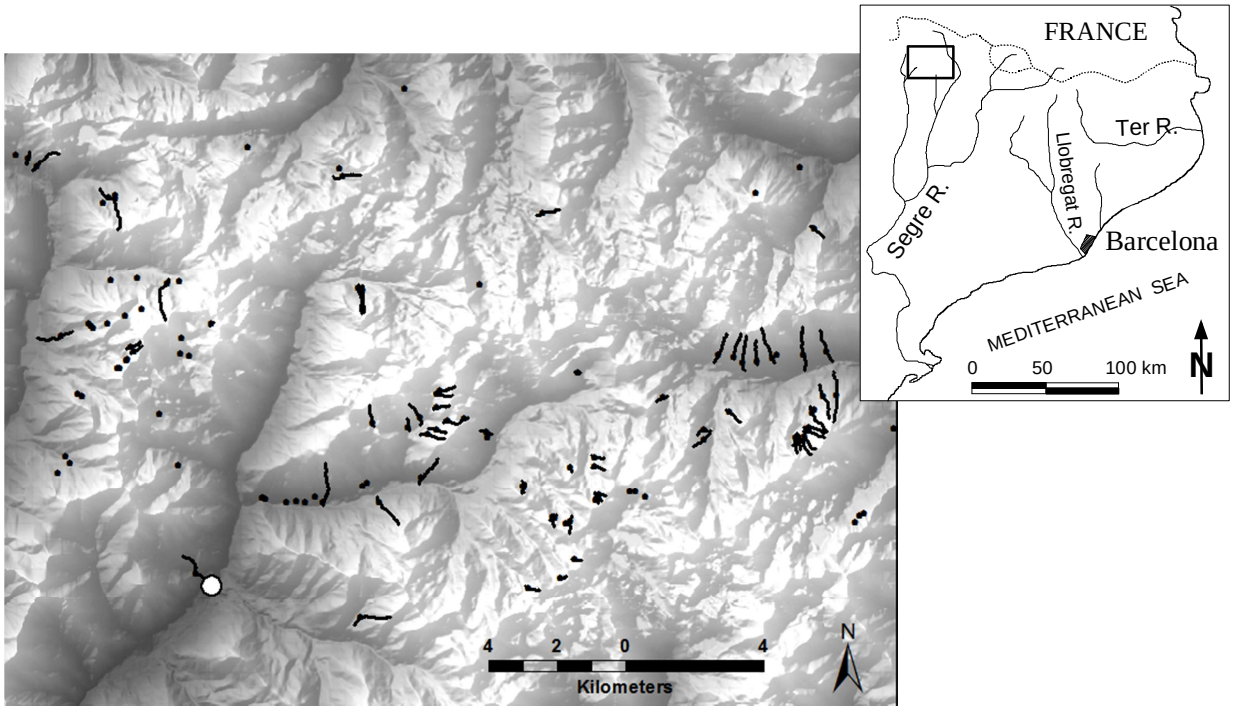

Figure 51: Debris-flows inventory and situation of the study area in the Central Pyrenees. The locations of the 116 affected torrents are indicated by dots, while some selected debris-flow tracks are given by lines. Erill test site is shown by the white circle.

The Erill site was chosen as Test Site for the fact it is one of the most active debris-flows known in the Pyrenees. While events have volumetric overlap in time with other major events in this region, its constant activity, has resulted in significant economic investment in mitigation measures in order to reduce this risk. This is a very small catchment (<0.5km^2) with average slope inclination (~16°), with almost no dressing plant due to the continued erosion and sedimentation of silty loam and gravely glacial resting on slates and quartzite of Devonian. The minimum elevation of the catchment is 1310 m asl and the maximum altitude is more than 2500 m asl. These conditions are representative extrapolated to many other basins in this area, and so are used for extrapolation pruposes.

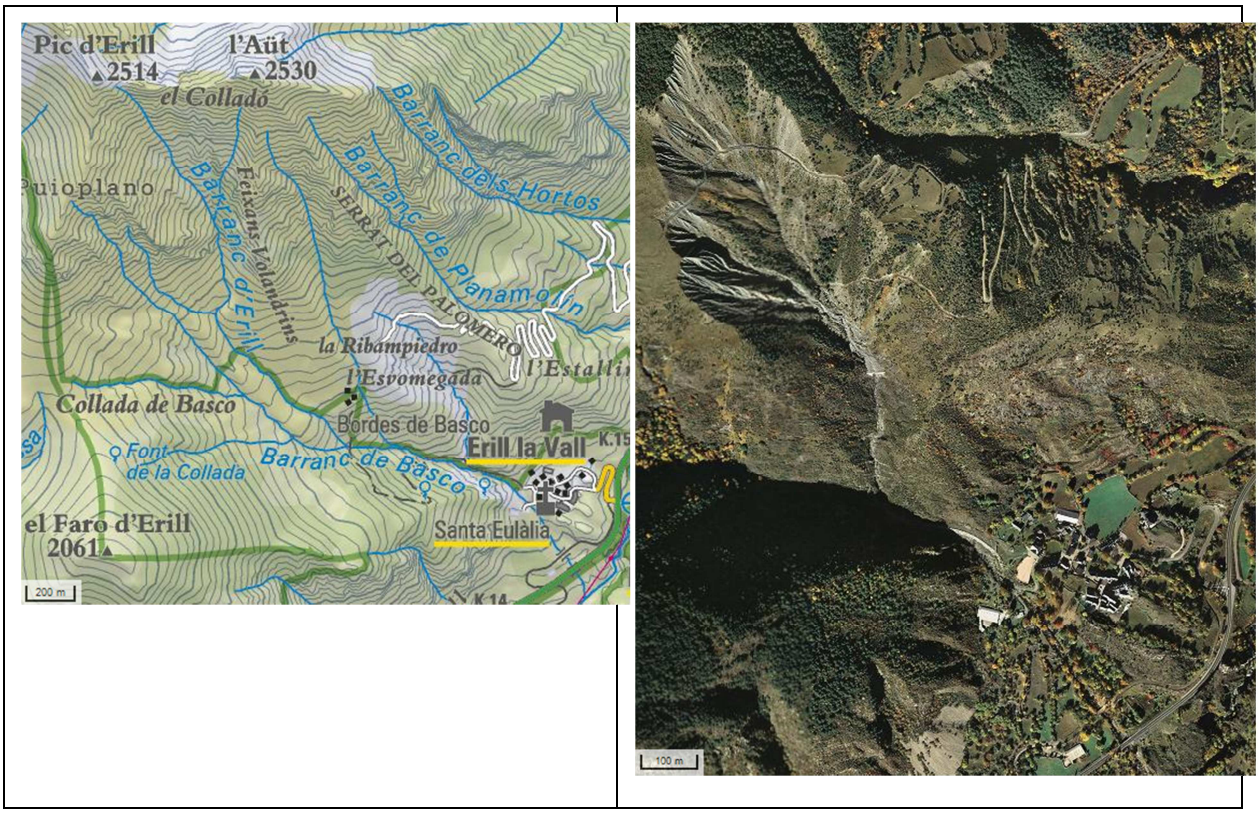

Figure 52: Erill test site. Topographic map of the entire catchment (left) and ortophoto of the lower part of the catchment and the fan (right).

b. Methods applied (UPC):

The occurrence of historic debris flows was analysed at two different scales: 1) at regional scale in a study area of about 384 km^2, which is located in and around the "Aigüestortes i Estany de Sant Maurici" National Park, and 2) at local scale in the Boí valley with particular emphasis on the Erill catchment.

1. Historic debris-flow occurrence at regional scale:

The documentation of historic debris-flows at regional scale included three main parts: 1) the interpretation of aerial photographs; 2) the digitalization in a Geographical Information System (GIS), and 3) the analysis of the inventory data.

The debris-flow inventory was built by the interpretation of several sets of aerial photographs covering a time span of 53 years. The details on the different datasets are listed in Table 13 and the explanation of their interpretation is given in the following.

Three types of photo-interpretation were applied due to different datasets: 1) standard interpretation of paper aerial photographs using a mirror stereoscope, 2) two-dimensional interpretation of digital ortho-photos, and 3) three-dimensional interpretation of digital ortho-photos.

Standard photo interpretation was applied to the printed pairs of aerial photos of 1975 and 1982. In contrast, the 1956/57 aerial photographs were analysed using the ortoXpres 1.0 application (http://www.ortoxpres.cat/) created by the Cartography Institute of Catalonia (ICC). In ortoXpres 1.0, the digitized and geo-referenced 1956/57 aerial photos can be visualised and directly compared with an extended cartography database consisting of topographic maps and recent ortho-photos. Thus, the interpretation of the 1956/57 aerial photo was two-dimensional. At last, the detailed aerial photos between 2004 and 2009 were analysed by the GoogleTM Earth software application (http://www.google.com/earth). GoogleTM Earth represents the colour ortho-photos in three dimensional views and facilitates a detailed interpretation.

It must be stated that the 1975 and 1982 datasets unfortunately did not cover the entire study area. While the 1975 photographs only covered 45%, the 1982 data represented 95%.

Table 13: Aerial photographs analysed

year	type*	scale or pixel size	source
1956/57	digitalised (bw)	1:33000	*ortoXpres 1.0*
1975	paper (bw)	1:18000	ICC
1982	paper (bw)	1:22000	ICC
2004	digital (col)	50 cm	Google™ Earth
2005	digital (col)	50 cm	Google™ Earth
2008	digital (col)	50 cm	Google™ Earth
2009	digital (col)	25 cm	Google™ Earth

* bw: black-white; col: colour

For each set of aerial photographs listed in Table 13, an inventory map was prepared and an overall inventory was created afterwards by merging all the data available. The inventories were created by the observation of different types of morphologic features and changes in the aerial photos. The debris-flow activity in a catchment or torrent channel was generally characterised by one of the following features: 1) observation of the deposit in the accumulation zone, 2) observation of deep erosion and/or lateral levees along the debris-flow track, 3) changes and damages in the vegetation, and 4) widening or migration of the debris-flow channel.

The area of each debris-flow event detected was digitized in ARCGIS over the base of the current coloured ortho-photos at a scale of 1:5000.

The magnitude of the events was generally determined by the area of the accumulation zone, A. Five different magnitude classes were defined (Table 14). It is evident that the magnitudes of the debris flows detected in the Central Pyrenees are smaller than events observed in other mountain ranges such as, for example the European Alps or the Canadian Coast Range (Jakob, 2005).

Table 14: Classes of debris-flow magnitude applied in this study.

Class	area of accumulation zone (m^2)
Very large	>4000
Large	2200-4000
Medium	1300-2200
Small	700-1300
Very small	<700

2. *Historic debris-flow occurrence at local scale (Erill):*

Three types of information were included to define the historic debris-flow occurrence at the Erill test site: 1) Interviews with the inhabitants of the local villages, 2) analysis of historic photographs; and 3) research in the historic archives.

Finally, a total of 19 interviews with people living in the valley were carried out and a time span from the 1930's to the end of the 20th century could be covered.

During the research on historic photographs, the oldest photo of the catchment and the fan was dated from August, 7 1920.

The research in historic archives mainly focused on the reports of the hydropower companies. Most of the information was found in the historic documents of the "Confederación Hidrográfica del Ebro" (http://www.chebro.es).

c. Historic debris-flow occurrence (UPC):

3. *Historic debris-flow occurrence at regional scale:*

A total of 194 debris flows were detected in 116 different torrents. Almost half of the debris flows were observed in the oldest aerial photographs of 1956/57 (Figure 53). Previous to 1956/57, an extreme flood occurred in October 1937. The 1937 flood is described in historic archives and other landslide studies as one of the most catastrophic that has affected the Central Pyrenees during the 20th century (Corominas and Alonso, 1984; Balasch, 2008). We assumed that most of debris flows identified in the 1956/57 photographs are related to the 1937 flood episode. The remaining cases may have been triggered by intense, but localised, rainstorms that occurred between 1937 and 1956/57.

The observed debris-flows areas range from ~200 m^2 up to 35000 m^2 and more than half of the magnitudes corresponds to the classes small and very small and only about 10% are debris flows of the class very large (Figure 53). Figure 53 shows no significant change on the rate of debris-flow production (expressed as events per years per square kilometre) for the last decades. This normalized production value indicates two peaks that can be related to the two largest historic flood events of the Central-Eastern Pyrenees in 1937 and 1982 (Novoa, 1984; Balasch, 2008).

Regarding the effects of climate change on the debris-flow occurrence in the 20th century, Figure 54 shows that no important reduction or increase of the magnitude can be observed over the time span analysed.

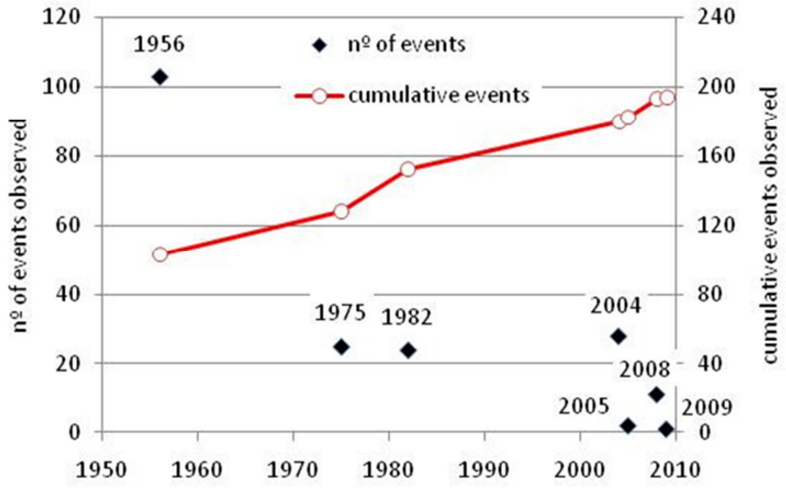

Figure 53: Number of debris flows observed in each dataset. Year of the datasets are given as labels

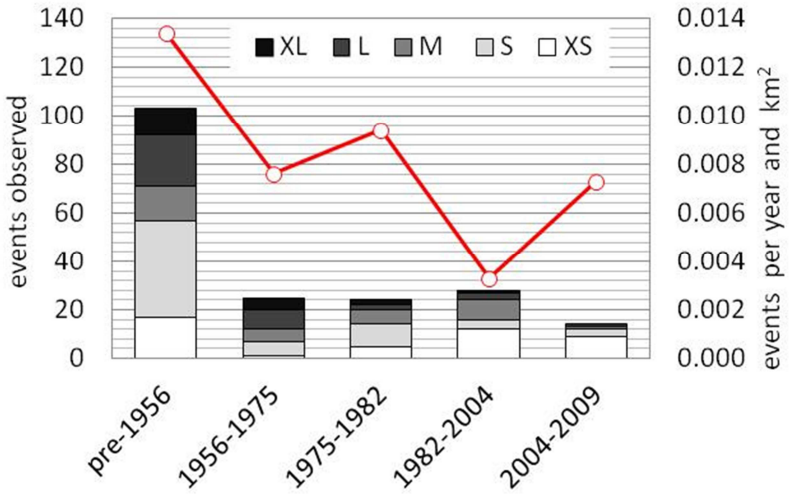

Figure 54: Debris flows observed within time intervals. Stacked columns indicate number of events separating different magnitudes. Line shows the number of events normalised per area and year.

4. Historic debris-flow occurrence at local scale (Erill):

The analysis of historic information on the debris-flow occurrence in the Erill catchment showed that several important events have taken place during the 20th century (Figure 55). Clear evidence of important debris flows with volume estimates between 10000 and 80000 m^3 were gathered for 1907, 1937, 1952 and 1963. In addition, other important events are assumed to have happened in the earlier 1920's, around 1930, between 1960 and 1964 and also in 1982. Smaller recent events occurred in 1997 and 2010. Since a sophisticated monitoring system was installed during 2005 in the catchment, several small debris flows and hyper-concentrated flows were registered.

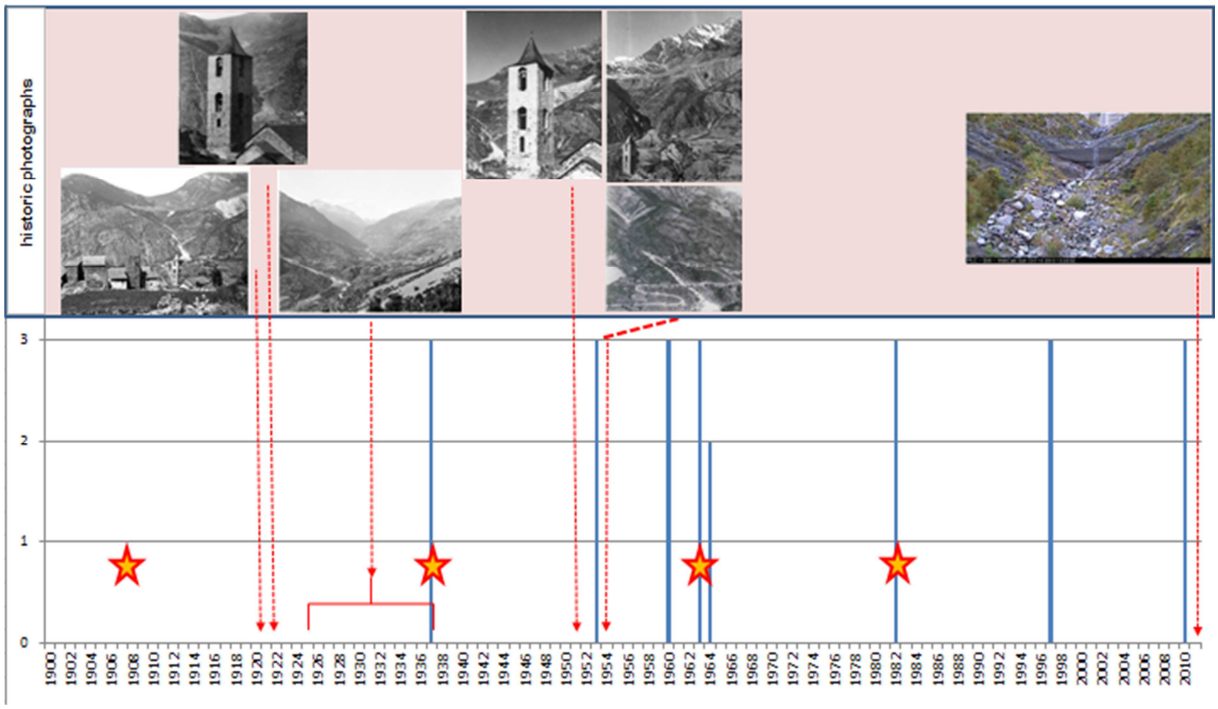

Figure 55: Debris-flow occurrence in the Erill catchment during the last 110 years. Blue bars indicate the results of the interviews; red discontinuous arrows show years of photographs and stars indicate results from the historic archives.

d. Comparison between debris-flow occurrence and rainfall data (UPC)

i. *Historic data*

Regarding the regional scale analysis, no trend of the increase or decrease in the debris-flow activity could be observed, as shown in Figure 54.

Regarding the local scale analysis carried out at Erill, Figure 56 presents a first comparison between rainfall data and historic debris-flow activity. The rainfall amounts were measured at Senet rain gauge located about 6.5 km to the West of the Erill catchment Only daily records are available and there is a large data gap in the 1930's and 1940's due to the Spanish Civil war. Only a slight correlation between the debris-flow occurrence and high annual or maximum daily precipitation can be observed.

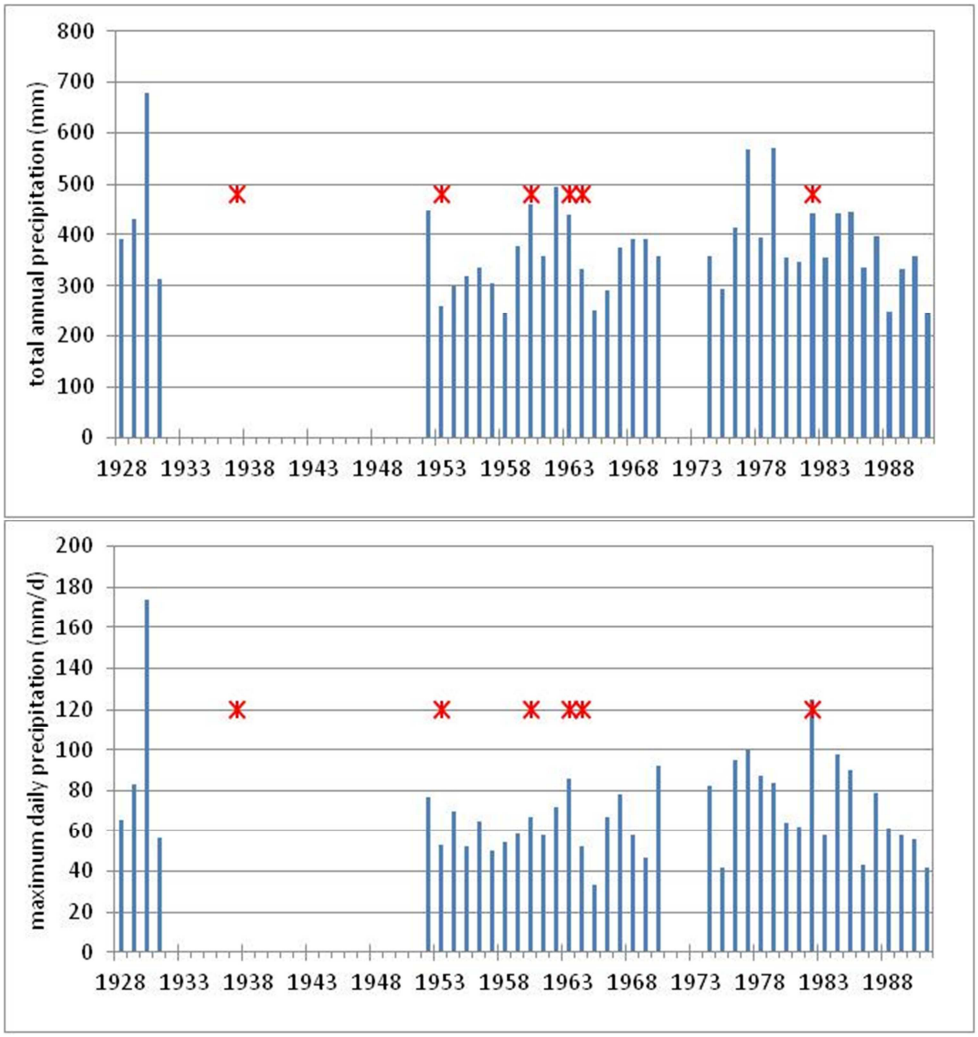

Figure 56: Comparison between rainfall data and important historic debris-flow events that occurred at Erill (year of event is indicated by red stars).

In a second step, the triggering rainfall amounts were analyzed for 12 debris flows that occurred during the 20th century (Figure 57a). In this case, the rainfall data were registered at the Boí meteorological station situated about 3 km to the south of the Erill catchment. In addition, the 12 triggering rainfall episodes were compared with other important rainfall events that were registered during the 20th century at the same meteorological station (Figure 57b).

The results show that even rather small daily rainfall amounts have triggered debris flows in historic times. This problem may partly be related to the daily record intervals, while convective rainstorms only last a few hours. In addition, we propose two other hypotheses to explain such low thresholds: 1) debris-flow initiation may be related to antecedent rainfall more than 7 days previous to the event; and 2) additional water input may be released by snowmelt (Hürlimann et al., 2010).

a)

b)

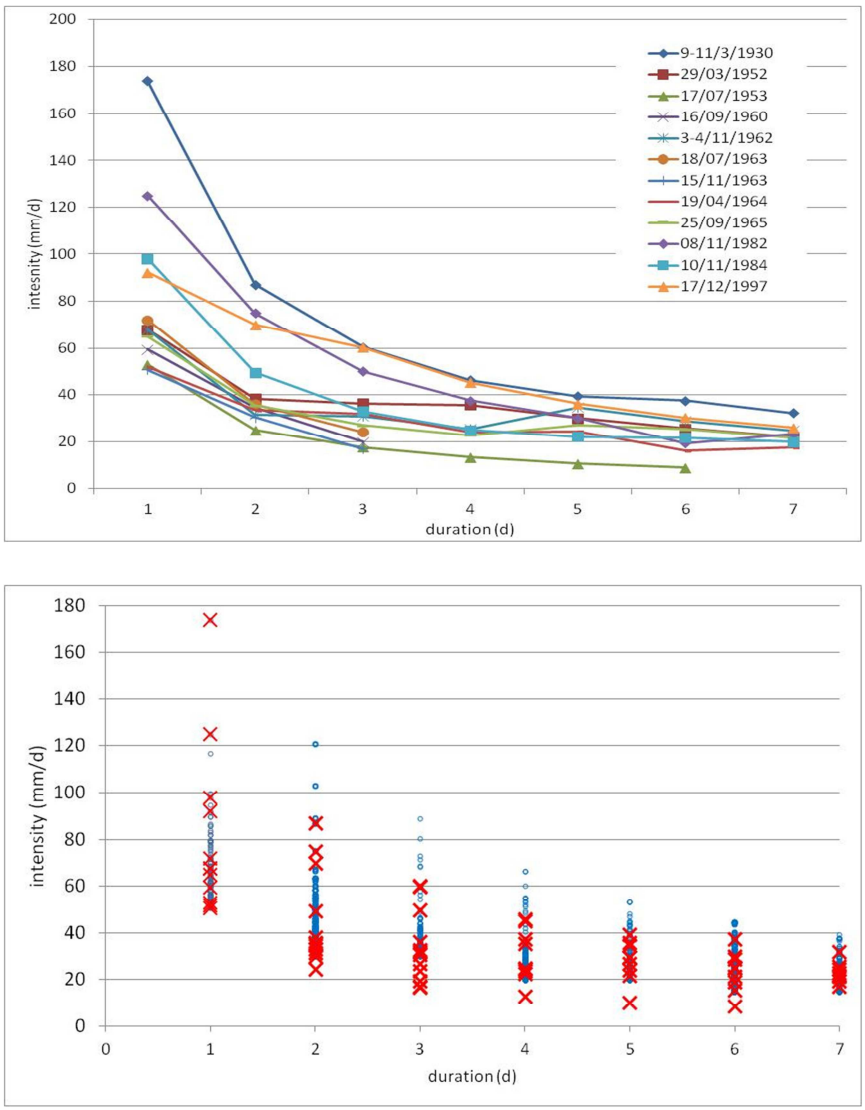

Figure 57: Characteristics of the debris-flow triggering rainfall events. a) Intensity – duration curves for the 12 analysed flow events. b) Comparison between debris-flow triggering rainfall events (red cross) and rainfall that did not trigger debris flows (blue circles).

ii. Future trend

Since for this site, climate change data downscaling is not provided by WP 3.1, regional modelling results published in the literature were used (Cabello et al., 2011). They focused on the analysis of extreme precipitation, which generally triggers debris flows, comparing return periods obtained from the Generalized Extreme Value (GEV) distributions fitted to the annual maxima series for both observation datasets and model results. The future trends between 2001 and 2100 for the Llobregat River Basin were taken into account from different IPCC mission scenarios. In this test case, B1 scenario, which assumes a rather moderate anthropogenic impact on climate, was regarded. Results obtained from the Llobregat River Basin can be extrapolated to our test area located less than 100 km to the west at the same south face of the Catalan Pyrenees.

In the results presented by Cabello et al. (2011), the annual maxima daily precipitation in the Llobregat River Basin was about 120 mm/d during the 100y return period during the control period (1971 – 2000), while the B1 scenario for the same return period estimates about 160 mm/d. This represents an increase of approximately 33% in the maximum daily precipitation for the future. Regarding a return period of 10 years, the maximum daily precipitation observed during the control period was ~80 mm/d, whereas the value for the B1 scenario was ~100 mm/d. This means an increase of about 25%. A similar trend was observed for annual maxima 6-hourly precipitation (personnel communication of A. Cabello, 2011). This 6-hourly time interval may better represent convective rainstorms that generally trigger debris flows in our test area. A comparison between the debris-flow triggering rainfalls shown in Figure 57 and the existing ID-curves is given in

Figure 58.

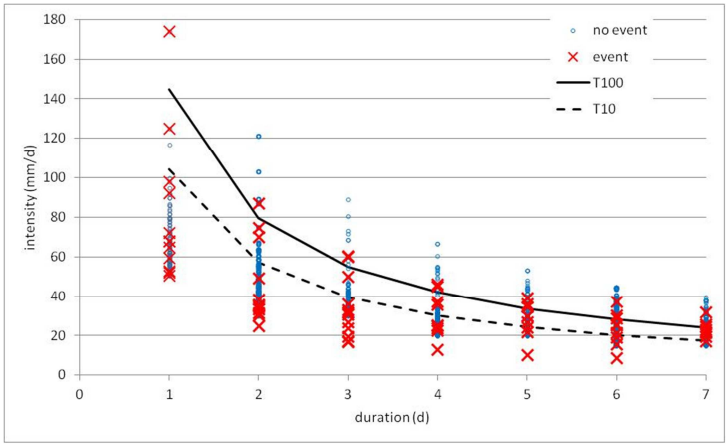

Figure 58: Comparison between debris flow triggering rainfalls and intensity – duration curve for 10 and 100 year return period (T) calculated for the rainfall data registered at the Boí meteorological station.

These future trends can be applied to the intensity – duration (ID) curves calculated for the historic rainfall data registered at the Boí meteorological station (Catalan Water Agency, 2003). This would mean that the rainfall amounts of the existing ID-curves would increase 25 and 33%, respectively.

DISCUSSION AND CONCLUSION

Influences of climate change on landslide activity have been analysed by different methods (statistical, empirical and physically-based methods) on different sites. Even if these sites present different contexts in view of landslides causes (climates, size of landslides), the analyses show that climate change is likely to induce similar trends in landslide activities. Based on the IPCC A1B scenario and on the resulting climate change scenario at local scale, the different models predict a very probable increase in landslide activities. This change would materialize either as an increase in the frequencies of landslides or as an increase in surface area of the potentially unstable areas (ks in their communes or valley, with for some of the models, spatial information. However, these models require precise data, not only for calibration but also for prediction, and so climate models should be adapted to such resolutions, like in this study.

Table 15).

The results differ from the predictions provided by larger scale models (Table 15). These differences might be explained by the finer calibration processes used for local scale analysis and also to the finer climate model used, which, for example, take into account the influence of topography on climate (mostly on precipitation). So, if large scale models are useful to determine where landslide activities will vary relatively to the other regions, the different kinds of local scale models are necessary for urban planners and all local authorities to estimate what would be the future risks in their communes or valley, with for some of the models, spatial information. However, these models require precise data, not only for calibration but also for prediction, and so climate models should be adapted to such resolutions, like in this study.

Table 15: Synthesis of the results for the different sites and comparisons with larger scale model (Safeland deliverable D3.7)

Local site	Results from D3.7	Methods used in D3.8	Results at local scale
Norway	No significant changes	Statistical modelling	Increase in superficies of areas exposed to higher hazard ranks
French Alps	Hazard ranking slightly decreases	Physically-based model	Increase in surface area of instable slopes and their probability of failure.
Italy	Hazard ranking decreases	Physically-based model	Increase in the number of mountain basins involved during rainfall events
Spain	no significant change (scenario IPCC A1B)	Empirical model	Increase in landslide frequency (scenario IPCC B1)

In order to improve the analyses performed in this study, several points would be interesting to consider in further studies:

- Use of different assessment methods at the different sites in order to improve the robustness of the analyses.
- Integration of other IPCC scenarios in order to have a wider variety of potential future climate.

- Consideration of the future evolution of the DEM and the lithology due to landslides or to human interventions.

REFERENCES

Aleotti, P. and , Chowdhury, R. (1999). Landslide hazard assessment: summary review and new perspectives. *Bulletin of Engineering Geology and the Environment*, 58 (1), 21-44

Apel, H., Thieken, A.H., Merz B. and Blöschl, G. (2004). Flood risk assessment and associated uncertainty. *Natural Hazards and Earth System Sciences*, 4, 295-308

Apostolakis, G. (1990). The Concept of Probability in Safety Assessment of Technical Systems. *Science*, New Series, 250(4986), 1359-1364.

Balasch, J. (2008). Les riuades del segle XX al Pallars Sobirà: 1907, 1937 i 1982. Generalitat de Catalunya, Barcelona, 240 pp. [In Spanish]

Bayraktarli, Y.Y., Ulfkjaer, J.P., Yazgan, U. and Faber, M.H. (2005). On the Application of Bayesian Probabilistic Networks for Earthquake Risk Management. In: Augusti et al., eds. Safety and Reliability of Engineering Systems and Structures. Proceedings of the ICOSSAR 2005, Rome. Rotterdam: Millpress, 3505-3512.

Bayraktarli, Y.Y., Yazgan, U., Dazio, A. and Faber, M.H. (2006). Capabilities of the Bayesian probabilistic networks approach for earthquake risk management. In: Proceedings of ECEEs First European Conference on Earthquake Engineering and Seismology, September 3-8, Geneva, Switzerland.

Benjamin, J.R. and Cornell, C.A. (1970). Probability, Statistics and Decision for Civil Engineers. McGraw-Hill, NY.

Bilotta, E., Cascini, L., Foresta, V., Sorbino, G. (2005). Geotechnical characterization of pyroclastic soils involved in huge flowslides. *Geotechnical and Geological Engineering*, 23, 365-402.

Cabello, A., Velasco, M., Barredo, J.I., Hurkmans, R.T.W.L., Barrera-Escoda, A., Sempere-Torres, D. and Velasco, D. (2011). Assessment of future scenarios of climate and land-use changes in the IMPRINTS test-bed areas. *Environmental Science & Policy*, 14 (7), 884-897.

Cascini, L. and Sorbino G. (2002). Soil suction measurement over large areas: a case study. Proc. 3rd Int. Conference on Unsaturated Soils, Recife (Brasil), Balkema 2, 829-834.

Cascini, L. and Ferlisi S. (2003). Occurrence and consequences of flowslides: a case study. Proc. Int. Conference on "Fast Slope Movements – Prediction and Prevention for Risk Mitigation", Napoli, Pàtron Editore, 1, 85-92.

Cascini, L., Guida, D. and Sorbino, G. (2006). Il Presidio Territoriale: una esperienza sul campo. G.N.D.C.I.-C.N.R. Edition, 139 pp.

Cascini, L., Cuomo, S. and Guida, D. (2008). Typical source areas of May 1998 flow-like mass movements in the Campania region, Southern Italy. *Engineering Geology*, 96, 107-125.

Cascini, L., Cuomo, S., Ferlisi, S. and Sorbino, G. (2009). Detection of mechanisms for destructive landslides in Campania region - southern Italy. First Italian Workshop on landslides (IWL 2009), 8-10 June 2009, Napoli, Italia. L. Picarelli, P. Tommasi, G. Urciuoli, P. Versace (eds.), ISBN 978-88-89972-12-0, 43 – 51.

Cascini, L., Cuomo, S., Pastor, M. and Sorbino, G. (2010). Modelling of rainfall-induced shallow landslides of the flow-type. *ASCE's Journal of Geotechnical and Geoenvironmental Engineering*, 1, 85-98.

Catalan Water Agency (2003). Recomanacions tècniques per als estudis d'inundabilitat d'àmit local. Departament de Medi Ambient, Generalitat de Catalunya, Barcelona, 89 pp.

Catani, F., Segoni, S. and Falorni, G. (2010). An empirical geomorphology-based approach to the spatial prediction of soil thickness at catchment scale. *Water resources research*, l46, W05508, 15pp.

Coles S. (2001). An Introduction to Statistical Modelling of Extreme Values. Springer, London.

Coles S., Pericchi L.R. and Sisson S. (2003). A fully probabilistic approach to extreme rainfall modelling. *Journal of Hydrology*, 273(1), 35-50.

Corominas, J. and Alonso, E. (1984). Inestabilidad de laderas en el Pirineo Catalan. Tipología y causas. In: ETSECCPB (Ed.), Inestabilidad de laderas en el Pirineo, Barcelona, C.1-C.53. [In Spanish]

Cuadrat, J. and Pita, M. (1997). Climatologia. Ediciones Catedra, Madrid, 596 pp.

Dussauge-Peisser, C., Helmstetter, A., Grasso, et al. (2002). Probabilistic approach to rock fall hazard assessment: potential of historical data analysis, *Natural Hazards and Earth System Sciences*, 2, pp. 15-26.

Faber, M.H. and Stewart, M.G. (2003). Risk Assessment for Civil Engineering Facilities: Critical Overview and Discussion. *Reliability Engineering and Systems Safety*, 80(2) 173-184.

Faber, M.H., Ranamukhaarachchi, S.L. and Rego, L. (2005). Sustainable Management of Natural Hazards in the Region of South-East Asia and South Asia. In: Proceedings of the International Symposium on Disaster Reduction on Coasts. November 14-16, 2005, Melbourne, Australia.

Faber, M.H., Bayraktarli, Y.Y. and Nishijima, K. (2007). Recent developments in the management of risks due to large scale natural hazards. In: Proceedings of SMIS XVI. Mexican National Conference on Earthquake Engineering. November 1-4, 2007, Ixtapa, Guerrero, Mexico.

Graf, M., Nishijima, K. and Faber, M.H. (2009). A probabilistic typhoon model for the Northwest Pacific Region. In: Proceedings of the 7th Asia Pacific conference on Wind Engineering. November 8-12, Taiwan.

Godt J.W., Baum R.L., Savage W.Z., Salciarini D., Schulz W.H. and Harp E.L. (2008). Transient deterministic shallow landslide modelling: requirements for susceptibility and hazard assessments in a GIS frame work. *Engineering Geology* 102, 214-226.

Hall, J.W. (2003). Handling uncertainty in the hydroinformatic process. *Journal of Hydroinformatics*, 5(4), 215-231.

Helton, J.C. and Burmaster, D.E. (1996). Guest editorial: treatment of aleatory and epistemic uncertainty in performance assessments for complex systems. *Reliability Engineering & System Safety*, 54(2-3), 91-94.

Hungr, O., Evans, S.G., Bovis, M.J., and Hutchinson, J.N. (2001). A review of the classification of landslides of the flow type. *Environmental & Engineering Geoscience*, VII (3), 221-238.

Hürlimann, M., Corominas, J., Moya, J. and Copons, R. (2003). Debris-flow events in the Eastern Pyrenees. Preliminary study on initiation and propagation. In: Rickenmann, D., Chen, C. (Eds.), 3rd Int. Conf. on Debris-Flow Hazards Mitigation. Millpress, Davos, 115-126.

Hürlimann, M., Abancó, C. and Moya, J. (2010). Debris-flow initiation affected by snowmelt. Case study of the Senet monitoring site, Eastern Pyrenees, Mountain Risks: Bringing Science to Society, Florence, Italy, 81-86.

Jacob, D., (2001). A note to the simulation of the Annual and Interannual Variability of the Water Budget over the Baltic Sea Drainage Basin. *Meteorology and Atmospheric Physics*, 58, No. 1-4, 61-74.

Jakob, M. (2005). A size classification for debris flows. *Engineering Geology*, 79, 151-161.

Jaedicke, C. and A. Kleven (2008) Long-term precipitation and slide activity in south-eastern Norway, autumn 2000. *Hydrological Processe*s 22 (4).

JCSS (2001). Probabilistic Model Code. The Joint Committee on Structural Safety. Internet Publication: http://www.jcss.ethz.ch/publications/publications_pmc.html

JCSS (2008). Risk Assessment in Engineering. The Joint Committee on Structural Safety. Internet Publication: http://www.jcss.ethz.ch/publications/JCSS_RiskAssessment.pdf

Jensen, F.V. (2001). Bayesian Networks and Decision Graphs. Springer, New York.

Lindley, D.V. (1976). Introduction to Probability and Statistics from a Bayesian Viewpoint. Cambridge, Cambridge University Press.

Malet, J.P. (2003). Les ‘glissements de type écoulement’ dans les marnes noires des Alpes du Sud. Morphologie, fonctionnement et modélisation hydro-mécanique. PhD thesis, Université Louis Pasteur, Strasbourg, France. [In French]

Malet, J.-P., Remaitre, A., Maquaire O., Durand, Y., Etchevers, P., Guyomarch, G., Deque and M., van Beek, L.P.H. (2007) Assessing the influence of climate change on the activity of landslides in the Ubaye Valley, In: McInnes, R. & Fairbank, H. (Eds): Proceedings International Conference on Landslides and Climate change - Challenges and Solutions, Wiley, London

Mann, C.J. (1993). Uncertainty in geology. In: Davis J.C., Herzfeld U.C. (eds.), Computers in geology – 25 years of progress, Oxford Univ. Press, 241–254.

McGuire, R.K., Cornell, C.A. and Toro, G.R. (2005). The case for using mean seismic hazard. *Earthquake Spectra* 21, 879-886

Montgomery, D.R. and Dietrich, W.E. (1994). A physically based model for the topographic control on shallow landsliding. *Water Resources Research*, 30, 1153-1171.

Morgenstern, N.R. and Price, V.E. (1967). A numerical method for solving the equations of stability of general slip surfaces. *Computer Journal*. 9, 388-393

Muñoz, A. (1992). Evolution of a continental collision belt: ECORS-Pyrenees crustal balanced cross-section. In: McClay, K.R. (Ed.), Thrust Tectonics. Chapman & Hall, 235-246.

Nadim, F., Kjekstad, O., Peduzzi, P., Herold, C. and Jaedicke C. (2006). Global landslide and avalanche hotspots. *Landslides* 3 (2).

Nishijima, K. and Faber, M.H. (2007). A Bayesian framework for typhoon risk management. In: Proceedings of the 12th International Conference on Wind Engineering. July 1-6 2007, Cairns, Australia. 1959-1966.

Novoa, M. (1984). Precipitaciones y avenidas extraordinarias en Cataluña. In: ETSECCPB (Ed.), Inestabilidad de laderas en el Pirineo, Barcelona, I.1.1-I.1.15.

O'Brien, J. S., Julien, P. Y., and Fullerton W. T. (1993). Two-dimensional water flood and mudflow simulation, *J. Hydrol. Eng.*, 119(2), 244–261.

Olivier, M., Sedan, O. and Monod B. (2011). Contribution of physical modelling to landslide hazard mapping: case of the French Basque coast. Proceedings of the 2nd World Landslide Forum, 3-October 2011. Rome, Italy.

Paté-Cornell, M. E. (1996). Uncertainties in risk analysis: Six levels of treatment. *Reliability Engineering and System Safety* (54), 95-111.

Pirulli, M. and Sorbino, G. (2008). Assessing potential debris flow runout: a comparison of two simulation models. *Natural Hazards and Earth System Sciences*, 8, 961-971.

Pirulli, M. and Sorbino, G. (2007). The runout of debris flows: application of two numerical models and comparison of results. In: Proceedings of the 1st North American Landslides Conference, 3-8 June 2007, 1, 1542-1551). ISBN/ISSN: 978-0-975-4295-3-2. : Editors: V.R. Schaefer, R.L. Schuster, A.K. Turner.

Pradel, D. and Raad, G. (1993). Effect of permeability on surficial stability of homogeneous slopes, *Journal of Geotechnical Engineering*, ASCE 119(2), 315–332.

Raiffa, H. (1968). Decision Analysis, Introductory Lectures on Choice under Uncertainty, Addison-Wesley, Reading, Mass.

Raiffa, H. and Schlaifer, R. (1961). Applied Statistical Decision Theory. Harvard University Press, Cambridge University Press, Cambridge, Mass.

Resseguier, S. (2006). The Geoextreme Project: River Bank Stability in a changing Climate. NGIReport 20051271-1

Rickenmann, D. (1999). Empirical relationships for debris flows, *Natural Hazards*, 19(1): 47-77.

Rochat, A., Grandjean, G., Cerdan, O. and Samyn, K. (under submission) Regional scale soil thickness prediction using digital terrain modelling and seismic data: application to erosion hazard mapping. *Earth and Planetary Science Letter*. Under submission

SafeLand D0.3 (2011). Dealing with uncertainties in modelling, prediction, and decision-making. Deliverable D0.3 report, SafeLand: Seventh Framework Programme for research and technological development (FP7) of the European Commission.

Safeland D1.2 (2010). Geomechanical modelling of slope deformation and failure processes driven by climatic factors: Shallow landslides, deep landslides and debris flows Deliverable D1.2 report, SafeLand: Seventh Framework Programme for research and technological development (FP7) of the European Commission.

Safeland D1.5 (2010). Statistical and empirical models for prediction of precipitation-induced landslides, Deliverable D1.5 report, SafeLand: Seventh Framework Programme for research and technological development (FP7) of the European Commission.

Safeland D2.10 (2010). Identification of landslide hazard and risk "hotspots" in Europe, Deliverable D2.10 report, SafeLand: Seventh Framework Programme for research and technological development (FP7) of the European Commission.

Safeland D3.1 (2012). Overview on and post-processing of available climate change simulations for Europe on a spatial scale of 25km with a special focus on meteorological extreme events. Deliverable D3.1 report, SafeLand: Seventh Framework Programme for research and technological development (FP7) of the European Commission

Safeland D3.2 (2012). REMO climate change simulations with 10km horizontal resolution for case study sites in Southern Italy, the Alps, Southern Norway, and Romania. Deliverable D3.2 report, SafeLand: Seventh Framework Programme for research and technological development (FP7) of the European Commission.

Safeland D3.3 (2012). Analysis of selected extreme precipitation events with the COSMO LM model on a special scale of 2.8 km. Deliverable D3.3 report, SafeLand: Seventh Framework Programme for research and technological development (FP7) of the European Commission.

Safeland D3.4 (2012). Report on projected changes in meteorological extreme events in Europe with a focus on Southern Italy, the Alps, Southern Norway, and Romania: synthesis of results. Deliverable D3.4 report, SafeLand: Seventh Framework Programme for research and technological development (FP7) of the European Commission.

Safeland D3.7 (2011). Deliverable D3.7 report, SafeLand: Seventh Framework Programme for research and technological development (FP7) of the European Commission.

Safeland D5.4 (2011). Quantification of uncertainties in the risk assessment and management process. Deliverable D5.4 report, SafeLand: Seventh Framework Programme for research and technological development (FP7) of the European Commission

Savage, L. J. (1954). The Foundations of Statistics, John Wiley & Sons, Inc., NY.

Savage, W.Z., Godt, J.W. and Baum, R.L. (2004). Modelling time-dependent areal slope stability. In: Lacerda, W.A., Erlich, M., Fontoura, S.A.B., Sayao, A.S.F., (eds.). Landslides – Evaluation and Stabilization. Proceedings of the 9th International Symposium on Landslides. Rotterdam: Balkema, 1, 23-36.

Schubert, M., Straub, D. and Faber, M.H. (2005). Reliability of rock fall protection galleries – A case study with a special focus on the uncertainty modelling. Safety and Reliability of Engineering Systems and Structures (Proc. ICOSSAR 05, Rome), Augusti et al. (eds), Millpress, 1333-1340.

Sedan, O. (2011). Logiciel ALICE version 7 – Guide Utilisateur. BRGM report. RP-60004-FR. 31p. [In French]

Sorbino, G. (2005). Numerical modelling of soil suction measurements in pyroclastic soils. Int. Symp. "Advanced experimental unsaturated soil mechanics", Tarantino, Romero & Cui (eds), Taylor & Francis Group, London, 541-547.

Sorbino, G., Sica, C. and Cascini, L. (2010). Susceptibility analysis of shallow landslides source areas using physically based models. *Natural Hazards*,53(2),313-332.

Stillwater Sciences (2007). Landslide Hazard in the Elk River Basin, Humboldt County, California. Final report. Prepared by Stillwater Sciences, Arcata, California for the North Coast Regional Water Quality Control Board.

Straub, D. (2005). Natural hazards risk assessment using Bayesian networks. In: Augusti et al., eds. Safety and Reliability of Engineering Systems and Structures. Proceedings of the ICOSSAR 2005, Rome. Rotterdam: Millpress, 2535-2542.

Straub, D. and Der Kiureghian, A. (2008). Improved Seismic Fragility Modelling from Empirical Data. *Structural Safety*, 30(4), 320-366.

Thiéry, D., (2003). Logiciel GARDÉNIA version 6.0 - Guide d'utilisation. BRGM report. RP-52832-FR. 104p. [In French]

Thiéry, Y., (2007). Susceptibilité du Bassin de Barcelonnette (Alpes du sud, France) aux 'mouvements de versant' : cartographie morphodynamique, analyse spatiale et modélisation probabiliste. PhD Thesis, Université de Caen, Caen, France. [In French]